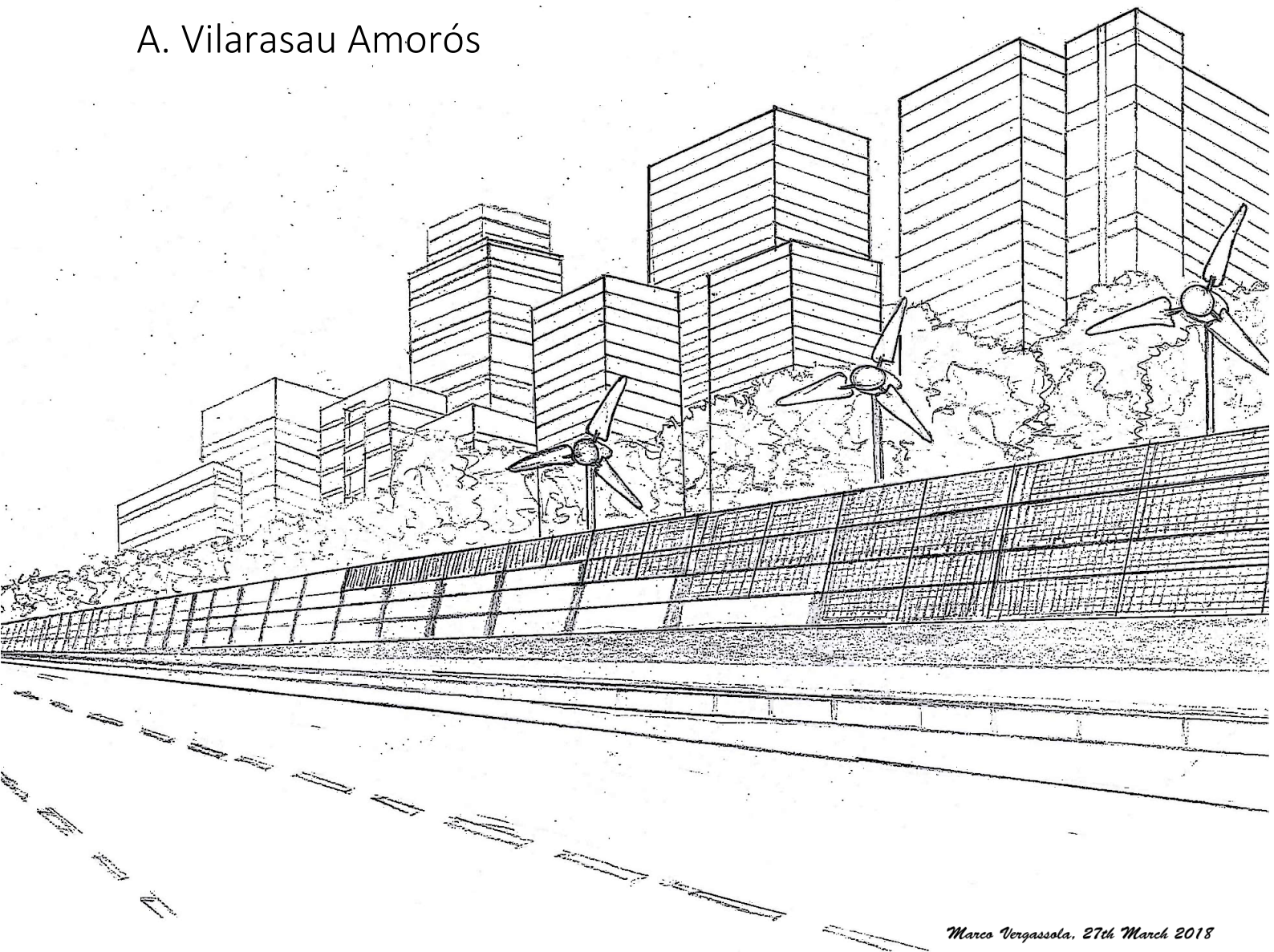


Turning noise-barriers into sustainable energy systems

A full approach from experimental data to energy and cost modeling with a focus on urban wind

A. Vilarasau Amorós



Marco Vergassola, 27th March 2018

Turning noise-barriers into sustainable energy systems

A full approach from experimental data to
energy and cost modeling with a focus on
urban wind

by

A. Vilarasau Amorós

to obtain the degree of Master of Science
at the Delft University of Technology,
to be defended publicly on Friday April 20th, 2018 at 12:30 AM.

Student number:	4633377	
Project duration:	September 1, 2017 – April 20, 2018	
Thesis committee:	Prof. dr. A.J.M. (Ad) van Wijk,	TU Delft, supervisor
	Dr. ir. W.A.A.M. (Wim) Bierbooms,	TU Delft
	Dr. ir. R. (Rene) Pecnik,	TU Delft

Cover illustration by Marco Vergassola. The author retains all copyrights associated with the work.

An electronic version of this thesis is available at <http://repository.tudelft.nl/>.

Abstract

Current urban systems have a linear metabolism; they rely on imported resources, which are used inefficiently, and they produce waste flows. Urban areas can become productive and not only consumptive if a well-planned distributed energy system is implemented. Switching to renewables, however, means rethinking today's urban landscape entirely. Decisions made for the future need to be built on a robust understanding of urban energy systems. There is a need to bring creative perspectives to include local potentials into urban planning and study the energetic gaps and opportunities that can foster a circular metabolism.

This thesis presents a modular energy generation system with an innovative noise-barrier integration feature. This novel concept, formally known as the *Energy Wall*, is designed to capture the local wind and solar energy resources of urban areas and transform them for urban use while exploiting the benefits of reusing existing urban stock. This paper embarks on a comprehensive assessment of the potential of this system taking a full approach from experimental data to energy and cost modeling. A study area located in Delft, the Netherlands, has provided a solid basis for this research. The base-case *Energy Wall* module in this area generates per year almost enough energy to supply the annual demand of a residential household. To account for the great diversity of urban environments, the energy supplied by the system is investigated in different scenarios with varying local characteristics. A number of cost reduction opportunities have been identified increasing the appeal of noise-barrier integration. Despite this, the small-wind system faces economic burdens hindering its profitability. Field measurements from sonic anemometers are employed to investigate the wind concentrator effect of a noise-barrier showing an acceleration effect up to 30% depending on flow perpendicularity. The robustness of current vertical wind profile scaling techniques is tested to gauge its reliability within the urban boundary layer. Results have underscored important gaps in the theory of near-surface wind speed prediction methods. The higher complexity and uncertainty of urban wind energy generation has given this research a special focus on understanding why this technology has lagged behind over the recent years and, most importantly, what steps should be taken to change this situation.

Preface

This thesis marks the completion of my Master in Sustainable Energy Technologies at the Delft University of Technology. I was engaged in researching and writing this project from September to April 2018. My interest in urban-integrated energy generation is due to my aspiration towards optimization of resources and my desire to work on a research project with tangible implications. The motivation of this work has its origin in finding solutions to practical problems of today's world.

I would like to thank my supervisors, Prof. Ad van Wijk and Nikolaos Chrysochoidis, for giving me the opportunity of exploring the field of urban-integrated energy systems with all its complexities and for their support throughout the process.

To my colleagues and friends, I am grateful towards you. It was always useful to share my doubts and discuss my ideas around with you. A special grazie to the cover artist.

My parents deserve a particular note of thanks, at moments of crisis, you kept me motivated. Your unconditional support and kind words have guided me throughout my journeys no matter how far they took me.

I hope you enjoy your reading.

Andrea Vilarasau Amorós
Delft, April 2018

Contents

List of Symbols	ix
List of Abbreviations	xi
List of Figures	xiii
List of Tables	xvii
1 Introduction	1
1.1 Motivation of this research	2
1.2 Scope and structure.	3
2 Energy Wall. Concept and context	5
2.1 Previous works and lessons learned.	6
2.2 Hybrid systems: A literature review	7
2.2.1 Modeling softwares	8
2.3 Characteristics of urban-integrated energy systems.	8
3 Study Area and Experimental Setup	11
3.1 Study area.	11
3.1.1 Description of resources	11
3.1.2 Terrain topology	13
3.2 The urban boundary layer	14
3.2.1 Flow around bodies: Theoretical background	14
3.2.2 Flow around bodies: Experimental analysis	15
3.2.3 Findings and verification of results.	20
3.3 Mapping surface roughness parameters	21
3.3.1 Aerodynamic characteristics.	21
3.3.2 Concluding remarks	25
4 Modeling methodology	27
4.1 Range of validity	27
4.2 Modeling distributed wind power.	28
4.2.1 Model elements	28
4.2.2 Vertical wind speed profile.	29
4.2.3 Correction factors	29
4.2.4 Starting behavior study	31
4.2.5 The power curve	33
4.3 Modeling distributed solar power.	33
4.3.1 Model elements	34
4.3.2 Effect of temperature and irradiance.	35
4.3.3 Sources of losses	37
5 Study of the Energy Supply	39
5.1 Solar, wind and hybrid generation profiles	39
5.2 Evaluating energy use strategies	41
5.2.1 Load-supplying against Grid-supplying	41
5.3 Concluding remarks	43

6	Sensitivity Analysis	45
6.1	Varying noise-barrier orientation	46
6.2	Varying wind resources	48
6.3	Varying hub height	50
6.4	Varying surface roughness	51
6.5	Varying power curve	53
6.6	Significance of sensitivities	55
7	Technoeconomical Assessment	57
7.1	The price of energy	57
7.1.1	Calculating the LCOE	58
7.1.2	Cost taxonomy.	59
7.1.3	A note on cost variability.	59
7.2	Noise-barrier-integrated wind system.	60
7.2.1	The question of system scale.	60
7.2.2	Cost breakdown	61
7.2.3	Cost reduction opportunities	63
7.2.4	LCOE range	63
7.3	Noise-barrier-integrated solar system.	64
7.3.1	The question of system scale.	65
7.3.2	Cost breakdown	65
7.3.3	Cost reduction opportunities	66
7.3.4	LCOE range	66
7.4	Noise-barrier hybrid system	66
7.4.1	Cost breakdown	67
7.4.2	LCOE range	67
7.5	Discussion	68
7.5.1	The effect of discount rate	70
8	Conclusions and Recommendations	71
A	Fluid Dynamics Model	73
A.1	Model framework	73
A.2	Model Parameters.	74
A.2.1	Coefficients for convective heat transfer	74
A.2.2	Sky temperature estimation	75
A.2.3	Absorptivity and emissivity	76
B	Detailed Economics	77
B.1	Description of wind system costs	77
B.2	Description of solar system costs	78
C	Technoeconomical Roadmap	81
D	Codes and Resources	83
	Bibliography	85

List of Symbols

α	Azimuth of the noise-barrier ($^{\circ}$)
A_m	Area of the solar module (m^2)
A	Swept area of the wind turbine rotor (m^2)
β	Relative angle between α and i ($^{\circ}$)
CF	Capacity factor (%)
C_p	Power coefficient (-)
C_r	Relative change in speed (%)
d_0	Zero-displacement length (m)
η	Efficiency of the solar module (%)
η_{STC}	Efficiency of the solar module at STC (%)
FF	Fill factor (%)
γ	Skew angle ($^{\circ}$)
G_m	Solar irradiation incident on the solar module surface (W/m^2)
G_{STC}	Solar irradiation at STC conditions (W/m^2)
H	Height of the noise-barrier (m)
HF	Hybridization factor (-)
i	Horizontal direction of the incoming wind flow ($^{\circ}$)
I_{MPP}	Current at maximum power point (A)
I_{SC}	Short circuit current (A)
k	Von Karman constant (-)
k_b	Boltzmann constant (JK^{-1})
λ_F	Front-area density of objects (-)
λ_P	Plan-area density of objects (-)
n	Ideality factor (-)
P_{in}	Kinetic power in the wind (kW)
P_{MPP}	Solar power output in DC at MPP (kW)
P_{out}	Power extracted by a wind turbine (kW)
ρ	Air density (kg/m^3)
$\sigma_{u,i}$	Standard deviation of u_i (m/s)
θ	Horizontal wind direction of anemometric measurements ($^{\circ}$)

TI	Turbulence intensity of a given i (-)
T_m	Temperature of the solar module (°C)
T_{amb}	Ambient temperature (°C)
T_{STC}	Temperature at STC conditions (°C)
u_0	Free stream wind speed (m/s)
U_j	Anemometric vector wind velocity in the direction j with $j = X, Y, Z$ (m/s)
u_j	Processed vector wind velocity in the direction j with $j = x, y, z$ (m/s)
u_i	Wind speed magnitude on the horizontal direction i (m/s)
u^*	Friction velocity (m/s)
V_{MPP}	Voltage at maximum power point (V)
V_{OC}	Open circuit voltage (V)
z	Height of an obstacle (m)
z_0	Surface roughness (m)
z_B	Blending height (m)
z_R	Height at which a measurement is taken (m)

List of Abbreviations

CanWEA	Canadian Wind Energy Association
CAPEX	Capital expenses
CFD	Computational Fluid Dynamics
DEMO	Dienst Elektronische en Mechanische Ontwikkeling
EV	Electrical Vehicle
GHI	Global Horizontal Irradiance
HOMER	Hybrid Optimization Model for Electric Renewables
KNMI	Koninklijk Nederlands Meteorologisch Instituut
LBL	Lawrence Berkeley National Laboratory
LCOE	Levelized Cost of Energy
LED	Light Emitting Diode
LPSP	Loss of Power Supply Probability
MPP	Maximum Power Point
NREL	National Renewable Energy Laboratory
O&M	Operation and maintenance
OPEX	Operation expenses
PNNL	Pacific Northwest National Laboratory
PV	Photovoltaic
STC	Standard Test Conditions

List of Figures

2.1	Artistic impression of the concept. Illustration by Marco Vergassola	5
3.1	Study area and noise-barrier section in yellow.	11
3.2	Hourly records of typical Meteonorm® year annual global irradiance (GHI) and ambient temperature.	12
3.3	Hourly records of typical Meteonorm® year wind speed.	12
3.4	Distribution of wind speeds as a function of the cumulative number of hours the wind speed exceeds a given wind speed.	12
3.5	Distribution of wind speed and direction over the period of one year, radial scale in % of time.	12
3.6	Terrain and near-surface characteristics of the study area. Map data ©2018 Google.	13
3.7	Streamlines of airflow around a built form; adapted from [37].	14
3.8	Streamline through the rotor; adapted from [37].	15
3.9	Change in maximum C_p as a function of skew angle γ [37]	15
3.10	Experimental setup definitions	16
3.11	Experimental setup on-site.	16
3.12	Definition of coordinates in anemometer equipment	17
3.13	Relative increase in wind speed with respect to wind direction.	18
3.14	Standard deviation of the relative increase in wind speed statistic.	18
3.15	Skew angle before noise-barrier (dashed) and above noise-barrier (solid).	19
3.16	Wind speed before noise-barrier.	19
3.17	Turbulence intensity before (dashed) and above noise-barrier (solid).	20
3.18	Relative change in wind speed and turbulence intensity.	20
3.19	Number of samples available for the calculation of statistics in each wind direction	20
3.20	Basic steps in method A to estimate surface aerodynamic characteristics.	23
3.21	Zero displacement scatter plot and statistical mean indicated with the symbol (+) calculated using method A and B based on multilevel anemometric data for seven incoming wind direction sectors.	24
3.22	Surface roughness length scatter plot and statistical mean indicated with the symbol (+) calculated using method A and B based on multilevel anemometric data for seven incoming wind direction sectors.	24
3.23	Aerial photo of the site in Sacramento (left) and the study area in Delft (right). Map data ©2018 Google.	25
4.1	Elements in the estimation of wind power production in the urban environment	28
4.2	Visualization of the boundary layer scaling technique.	29
4.3	Acceleration factor (indicated with + or -) and power factor (indicated between parenthesis) as a function of relative angle β for a 1.5H flow height. Bold line is aligned with the noise barrier long-axis.	30
4.4	Flow block diagram of wind turbine state transition	31
4.5	Distribution of time spent in each turbine state as a function of wind speed.	31
4.6	Comparison of distribution of time spent in each state as a function of speed using one dataset at two different resolutions.	32
4.7	State-of-turbine percentages using one dataset at two different resolutions.	32
4.8	Comparison of experimental and manufacturer power curves of the employed turbine.	33
4.9	Elements in the estimation of solar power production	34
4.10	Annual distribution of irradiation levels on a surface at three different altitudes. Estimated annual energy yield of one solar module is provided in brackets.	34

4.11	Incident annual irradiation as a function of module altitude and azimuth. Hourly irradiation data from Meeonorm® at the location of Delft, the Netherlands.	35
4.12	Normalized η_{MPP} efficiency as a function of irradiance on module G_m , and for different constant module temperatures T_m , of 25°C (red), 35°C (blue) and 15°C (yellow) and for variable realistic module temperature derived with the fluid-dynamics model (green).	36
5.1	Schematic and dimensions of a standard 6-meter <i>Energy Wall</i> segment.	39
5.2	Daily distribution of average power generated by 12 solar panels coupled onto the <i>Energy Wall</i>	40
5.3	Daily distribution of average power generated by one urban wind turbine coupled onto the <i>Energy Wall</i>	40
5.4	Daily aggregated load for common electricity use for a residential household with annual electricity demand of 3400 kWh	41
5.5	Daily production and consumption profiles for a system with 12 solar panels with 80° tilt and one urban wind turbine coupled onto a south-oriented noise barrier. Only 4 months displayed.	42
5.6	Aggregated production and consumption of each month. Annual generation is 3227 kWh with solar contributing 93.9% and wind 6.1% (i.e. 2992 kWh and 235 kWh respectively) and annual demand is 3400 kWh.	42
6.1	Energy rose showing in red the energy available in the local wind (E_{in}) and in blue the energy produced by the wind turbine (E_{out}). Radial axis in kilowatt-hour (kWh), time frame of one year.	46
6.2	Power produced by the turbine including the concentrator effect of the noise-barrier (solid line) and without the effect (dotted line) for eight orientations; annual energy yields are between brackets; radial axis in kWh.	47
6.3	Monthly distribution of solar and wind energy generation levels for eight noise-barrier orientations. Annual yields appear separately in the box.	47
6.4	Wind roses at reference height with radial axis given as time frequency (%) in a year.	49
6.5	Energy roses showing in red the energy available in the local wind (E_{in}) and in blue the energy produced by the wind turbine (E_{out}); annual energy yields provided in Table 6.1; radial axis in kilowatt-hour (kWh), time frame of one year.	49
6.6	Energy generation at each wind speed for the investigated wind resources (top) and corresponding state-of-turbine percentages (bottom); annual energy yields are indicated in brackets (kWh); results from southwest noise-barrier orientation only.	50
6.7	Sensitivity of annual energy output (blue) and corrected mean speed (orange) to varying hub height and surface characteristics for 4 different wind resources. Results are normalized to the base-case of Delft. Legend describes different sensitivity scenarios: varying hub height (HH), neglecting zero-displacement height (ZD), under- and over- estimating surface roughness parameters (MR^- and MR^+)	52
6.8	Base case power curve derived experimentally and improved power curve inspired in KETech®'s <i>Archimedes</i>	53
6.9	Energy generation at each wind speed (top), distribution of time spent in each turbine state as a function of wind speed (middle) and corresponding state-of-turbine percentages (bottom); annual energy yields are indicated in brackets (kWh); results from Delft wind resource and southwest noise-barrier orientation.	54
6.10	Sensitivity results for Delft wind resource at all noise-barrier orientations. Displayed parameters are normalized annual energy output (blue) and corrected mean speed (orange). Legend describes different sensitivity scenarios: varying hub height (HH), neglecting zero-displacement height (ZD), under- and over- estimating surface roughness parameters (MR^- and MR^+).	54
7.1	Noise-barrier coupling bracket prototype designed by Electronic and Mechanical Support Division (DEMO).	61
7.2	Cost breakdown of three single-turbine projects employing a commercial <i>micro</i> wind turbine on different mounting structures.	62
7.3	Cost breakdown comparison between a single-turbine project and a project employing ten turbines.	63
7.4	The calculated LCOE of small-wind for two system configurations; min/max ranges are given for those systems that have orientation-sensitive generation.	64
7.5	Cost breakdown the noise-barrier-integrated solar system adapted from [32].	65

7.6	The calculated LCOE of the noise-barrier-integrated solar system (NB-M) and the same system installed at an optimum tilt angle (OT-M); min/max correspond to North (N) and South (S) noise-barrier orientation.	66
7.7	Cost breakdown the noise-barrier hybrid system.	67
7.8	The calculated LCOE of the hybrid <i>Energy Wall</i> system for two sites of differing wind resources.	68
7.9	Positive cycle of small wind energy market development	69
C.1	Example of technoeconomical planning of a prospect <i>Energy Wall</i>	82

List of Tables

3.1	Linear regression statistics for the calculation of d_0 and z_0 using method A and B based on n number of cases out of the total number of observations within each sector. Dimensionless values; mean slope b and intercept a of the linear regression; $rmse$, root mean square error; r^2 coefficient of determination; n/a , not applicable or unreasonable value associated with small n available.	24
3.2	Surface roughness parameters of the study area as a function of direction sector. Experimental data unavailable for the direction sectors marked with asterisk.	26
4.1	Correction factors derived experimentally from the nose-barrier wind concentrator effect analysis. Values reported for a height equal to 1.5 the height of the noise-barrier.	30
4.2	SUNIVA Optimus® monocrystalline solar module specifications at STC.	35
4.3	Breakdown of solar system losses	37
6.1	Characteristics of the selected wind resources	48
6.2	Sensitivity analysis results of varying noise-barrier orientation (α) and varying wind resource.	50
6.3	Energy yield and mean wind speed for a higher hub height of 10 m normalized to the energy yield and mean wind speed of the base case hub height of 8 m reported in Table 6.3.	51
7.1	Comparison between average installed costs of small wind projects based on different sub-grouping systems from three reports published by renewable energy research institutes or associations; Canadian Wind Energy Association (CanWEA), Lawrence Berkeley National Laboratory (LBNL) and Pacific Northwest National Laboratory (PNNL).	61
7.2	Summary of main results for the different potential systems for the local solar and wind resources of Delft.	69
7.3	LCOE in Eur/kWh of each system at different discount rates	70
A.1	Air properties at 30°C.	74



Introduction

Since its introduction in the World Commission on Environment and Development of 1987, the term sustainable development has been widely used to describe the economic, environmental and social improvement that fulfills current demands without compromising the ability of future generations to fulfill their own demands [13]. And yet two decades after, the current profit-focused economic model fostered by globalization is incompatible with the concept of sustainable development. Urban areas occupy less than three percent of land surface and consume more than two thirds of primary energy [7]. Urbanization rates have been on the rise since the industrial revolution and this trend is expected to continue. Although cities are the result of energy development, urban demands are met almost entirely through imports, often across continents. This consumption pattern has resulted in a series of ecological and environmental problems. Researchers have introduced the idea of urban metabolism as a metaphorical framework to study the input and output flows of energy and matter of urban areas [33]. Within this framework, future sustainable urban systems will ideally have a circular metabolism. Current urban systems have, however, a linear metabolism: relying on imported resources, which are used inefficiently, and producing waste outflows. Most troubling, today's urban systems are characterized by a less efficient use of resources than natural systems; incapacitating natural systems to sustain urban systems. Urban metabolism should evolve from linear to circular and renewable energy technologies have a major role in this transition.

Much research has been done related to large renewable energy generation plants compared to the use and development of renewable technologies at the urban level. Clearly, it is much easier to plan and design a new development to be compatible with renewable energy technologies rather than retrofitting built-up areas. On one side, large utility-scale solar or wind farms facilitate renewable energy delivery and benefit from higher energy yields and better margins. On the other, small scale urban generation faces more obstacles in reaching a significant share in the urban energy mix and is more uncertain. A well-planned distributed generation system can, however, result in productive and not only consumptive urban areas, embodying the concept of circular metabolism and alleviating the enormous pressure that cities put on the environment. Thus, the energy transition must happen at both macro and micro scales, and the latter is lagging behind. Micro-scale energy transition requires changes in the way cities are conceived [7]. Essentially, there is a need to include local potentials into urban planning and study the energetic gaps and opportunities that can foster a circular urban metabolism. Diversifying energy sources through distributed energy generation can be seen as an opportunity to strengthen the energy security and economic resilience of a city while reducing the ecological footprint of urban activity [21]. Supplying local demand with locally available resources also shortens the distance between production and consumption, which can further contribute to energy savings, demand reduction and de-carbonization of the energy system due to less emissions during extraction, transformation and transportation of resources [33].

With all these in mind, the concept of *The Energy Wall* was born as a strategy to harvest near-road renewable energy by retrofitting noise cancelling barriers into hybrid solar-wind generation systems. The coupling of solar panels and small wind turbines onto already built noise barriers gives rise to a number of opportunities. The two most evident, making a better use of the already existing stock of urban and peri-urban constructions and contributing to a circular metabolism. There is also a reduction in cost and materials asso-

ciated with the re-use of existing infrastructure and the possibility of exploiting the wind concentrator effect of certain built forms for wind energy extraction. Generally speaking, closing urban cycles implies three central aspects: identifying the local resources of cities, efficiently capturing and transforming them for urban use, and minimizing residual outflows by reducing emissions and stimulating re-use and re-cycle practices. Reflecting on the first aspect, there is a need to explore ways to seamlessly merge renewable energy technologies with our built environment that maximize energy production. In this context, the question about retrofitting is a very important one because so much of the urban environment is already built and very slow to change. Researchers in this field must cope and respond to the dynamic technological situation incorporating both current and future trends. Moreover, retrofitting urban areas has an added complexity: local characteristics dictate the constraints and opportunities of the implementation of renewable energy technologies. Consequently, the ability to model and estimate the energetic potential of a specific technology in a specific location is crucial to reach a circular urban metabolism. In this sense, although the *Energy Wall* concept holds great promise, much work still remains to be done before determining the possibilities and impossibilities of this innovative approach towards closing urban cycles.

1.1. Motivation of this research

Switching to renewables means rethinking the entire urban landscape from buildings to transport to industry and power [26]. As the share of electricity generated from uncontrollable renewable energy sources such as solar and wind increases, specific challenges will arise. Smarter and more flexible electricity grids will be necessary to allow bidirectional power flows. Thus, decisions made for the future need to build on a robust understanding of urban energy systems. Urban-integrated energy systems are challenging in their implementation and require coordination across city planners, policymakers, technology developers and researchers. This project will contribute in this research field by studying the potential of the *Energy Wall* as a renewable urban-integrated energy system.

There is considerable experience in successful micro-generation projects in open rural areas, but understanding how integrated solar and wind will perform in urban areas is technically challenging. While distributed solar generation has grown in maturity and gained popularity among residential customers, which has motivated research and experience; this is not the case for urban small-scale wind energy. Theoretical and empirical evidence of the performance of urban wind energy technologies is limited, largely due to the limited research in the field. While much can be drawn from existing theory, the best methods for assessing the performance of small turbines in urban areas are unclear [49]. To address this gap, this research has a special focus in understanding wind micro-generation.

Although interest in circular urban metabolisms and renewable micro-generation is coming from many sectors (educational, environmental and commercial) it is being counterbalanced with the lack of experience in many aspects associated with its deployment. Firstly, because precise estimation of energy yields remains problematic and undermines user confidence, and secondly, because it is still unclear how much energy potential realistically exists in urban sites [31]. The aim of this research is to put some of these questions into context and provide answers so that barriers can be recognized and solutions developed. This Master Thesis will report on the following research questions:

1. What is the energetic potential of the *Energy Wall* as an urban-integrated renewable energy generation system? Which energy management strategies can ensure a sustainable and efficient use of the energy supplied by a system of these characteristics?
2. To which extent does the structure of the noise-barrier affect the local wind and solar resources?
3. How sensitive is the output of the *Energy Wall* to changes in local characteristics such as noise-barrier orientation, wind resource and surface aerodynamics? How can these sensitivities be translated into practical guidance for installing and planning new urban forms?
4. How well do current modeling techniques used in small-wind urban energy generation work in the face of uncertain input parameters? To what extent are the estimated energy yields reliable? And if they are, how much wind energy potential realistically exists in urban sites?
5. What are the barriers blocking the economics of the *Energy Wall* as a profitable urban-integrated system? What are the steps required to overcome these barriers?

1.2. Scope and structure

The aim of this report is to guide the reader through the various steps followed to study the possibilities and impossibilities of the *Energy Wall* concept in current and future urban areas. Two phases can be distinguished; in the first phase, work is directed towards developing a model with the capability to predict the energy generated by this hybrid system within the complex urban environment; in the second phase, the model is used to study the economic viability of the *Energy Wall* concept itself. Wind and solar energy are not treated equally in this study, the former is given special consideration due to the limited research in comparison with the latter. The report is organized as follows.

- Chapter 2: Provides a review of previous works, urban hybrid systems literature and state-of-the-art modeling techniques. Elaborates on the characteristics that set distributed energy systems apart from utility-scale systems to familiarize the reader with the particularities of energy generation in urban environments. The disadvantaged position of small wind with respect to the current technical and market development of distributed solar energy is also addressed to argue the special treatment that urban wind energy receives throughout the report.
- Chapter 3: Describes the study area, the local energy resources and, more in depth, the characteristics of wind flows within the urban boundary layer. This includes a theoretical background of flow around bodies and their potential wind concentrator effect; the methodologies followed to log, process and analyze the experimental data used to understand the wind behavior around the noise-barrier; and a discussion of the obtained results against similar studies. The outcome of this analysis is used in the modeling phase to investigate the wind concentrator effect of noise-barriers and derive correction factors for the flow as well as for the refinement of the vertical wind profile estimates. The last section describes the approach chosen to map the surface aerodynamics of the study area.
- Chapter 4: Develops two urban energy generation models. The first one models the energy generated by a small-wind turbine mounted on top of a noise-barrier. The second one models the energy generated by an array of solar modules installed on the wall surface of a noise-barrier. The central purpose of this chapter is to take an in-depth view of the unpredictability inherent in non-dispatchable energy sources and the variability associated with urban energy generation. All this with the aim to develop a model as precise as the intrinsic uncertainty of its elements permits.
- Chapter 5: Investigates the energy supply of the *Energy Wall* through the coupling of the generation models introduced in the previous chapter. First conclusions regarding the possibilities and impossibilities of the system in current urban areas are drawn, setting the ground for the sensitivity analysis that comes next.
- Chapter 6: Presents the sensitivity analysis conducted to investigate the *Energy Wall* supply in different circumstances and to evaluate the robustness of the developed models. The main purpose of this chapter is to recognize the most influential parameters affecting energy generation output and translate the obtained results into useful information for technology developers, urban planners and researchers.
- Chapter 7: Examines the economics of the three potential systems in which a noise-barrier can be converted into. This includes a discussion of cost evaluation issues arising from the noise-barrier-integration attribute of the studied system.
- Chapter 8: Presents conclusions and recommendations.

2

Energy Wall. Concept and context

The *Energy Wall* concept describes a urban-integrated hybrid system combining solar and wind energy generation on noise-cancelling barriers along roadways. If well-developed, this concept can harvest urban clean energy with an economic return by means of retrofitting already existing structures into renewable energy generation plants.

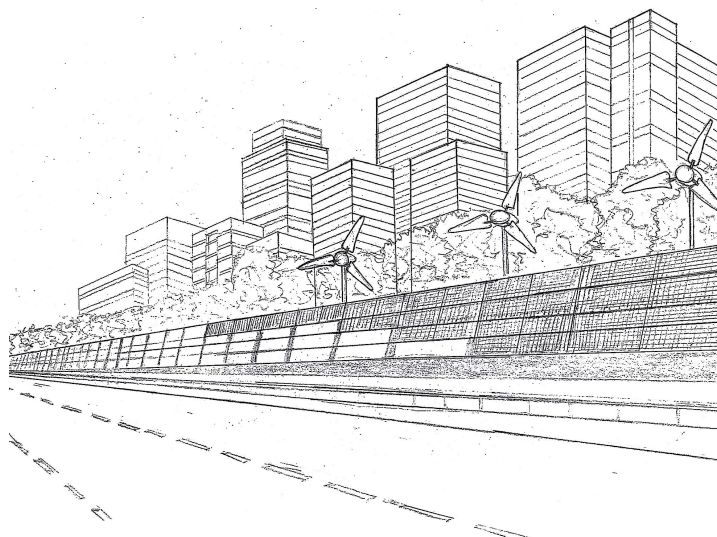


Figure 2.1: Artistic impression of the concept. Illustration by Marco Vergassola

The first building block of this novel concept is a noise-cancelling barrier. Noise barriers are exterior structures designed to shield inhabitants from noise pollution. The urban and suburban sites where noise barriers are commonly installed are located in close proximity to residential areas and/or a coupling point with the national electricity grid. This allows a flexible approach towards ensuring that the generated energy is efficiently used and energy waste is minimized. Which approach will lead to the best economic return is still unclear. While urban photovoltaic systems are becoming increasingly popular, urban wind energy is not yet competitive. In fact, partly due to the relatively low potential of urban wind turbines, many questions remain regarding the economics of the *Energy Wall*. Work oriented towards characterizing the potential of this novel concept in terms of energy generation and economic attractiveness has been conducted. However, there is still a long way to go in realizing the true potential of the *Energy Wall* and finding the answers to all the questions that remain. Presently in Delft, an outdoor setup has been installed to gather real site data usable for continuing research in this direction. This site is used as the study area of this research.

In view of the above, there are two important lines of research. First, the study of the *Energy Wall* generation capabilities and second, the study of energy use strategies that can bring added economical value to a system of these characteristics. A review of similar works reported in literature provides a rich source of information and is presented in the following sections.

2.1. Previous works and lessons learned

The *Energy Wall* has been the main focus of two prior works from Master students of the Delft University of Technology. On one side, Natalia Aleksandrova conducted a preliminary assessment of the generation potential of the Energy Wall based on meteorological data from a nearby weather station. Models for wind and solar power generation were coupled with a storage system model in order to run real-time simulations. For the wind generation model, the classic logarithmic wind profile was used to translate the wind speed at the reference height to the desired height, and assumed roughness lengths were used. However, it cannot be concluded that the model is a fair representation of the wind resources at the site. In the first place, no further consideration was given to the differences between utility-scale wind generation and urban wind generation. Secondly, the wind data was not corrected to account for the effect that the wall structure has on the wind flow and tilt angle. The former may have led to an overestimate of the wind speeds while the latter could have introduced both over- and under- estimates depending on the distribution of the incident wind direction on the wall. The solar generation model includes a simple estimation for cell temperature but corrections for the possible influence of nearby traffic and pollution are not considered. The choice of panel tilt is made based on maximum yearly production without much consideration of the physical limitations that arise from coupling solar panels on a tilted wall.

A rough approximation of a LED lighting load profile is generated and a load sizing algorithm based on literature is adopted to find the optimum size of the system. The algorithm considers different system configuration and determines which combination satisfies a desired loss of power supply probability. Economic aspects are not taken into account. With the optimum configuration, a modular design is then selected to resize the system for the available physical space on-site. Each module powers up one LED light and consists of 36 PV panels, 2 urban wind turbines and one 258Ah battery. Annual production per module is found to be around 11 MWh. The study provides valuable insights on the limitations that a high degree of energy supply intermittency poses when designing a cost-effective hybrid system. This highlights the importance of developing a strategy to tackle the mismatch between generation and consumption. Natalia concludes that increasing wind energy's contribution does not necessarily lead to a decrease in solar installed capacity or battery size. In regards to the proposed modular configuration and system power output, more realistic wind and solar generation models should be developed in order to draw final conclusions on system feasibility. Because no consideration is given to the economics of the system, the sizing algorithm loses relevance when the real implementation of the Energy Wall concept is in question.

On the other side, Changzhi Liu explored the application of the Energy Wall concept for electrical vehicle charging. The methodology followed to assess the energy generation potential of the system is similar to that of Natalia's, except that Changzhi performs a statistical analysis of the energy production profiles using meteorological data of the past 10 years to evaluate the uncertainty inherent in wind and solar resources. Calculations are based on a grid-connected hybrid system with 36 PV modules, 2 urban wind turbines and no energy storage. The statistical analysis quantifies the meteorological variability of the site. The results are useful to conclude that forecasts can be addressed based on monthly and annual analysis while the unpredictability of daily and hourly fluctuations cannot produce realistic forecasts. Demand profiles are constructed for two scenarios, workplace charging and public charging, based on a survey of EV types and energy consumption in the Netherlands. Each demand profile reveals different excess energy patterns throughout the year. The study concludes that increasing the fraction of renewable energy used for charging comes with increasing grid dependency and suggests that improvements should be made to increase the effectiveness of the system. This should be done by implementing strategies that can increase the fraction of used renewable energy and/or minimize the energy exchange with the grid.

A common challenge of both projects is how to deal with the large amount of excess energy that the system produces. This is a direct consequence of the day-night pattern of solar availability magnified by the relatively small contribution of wind generated power, which is not enough to mitigate this effect. The 36

PV panels generate 80% of the system output in both system configurations. As a matter of fact, all generation systems with high penetration of renewable energy sources are faced with this challenge. The balancing energy problem is one of the main drawbacks of integrating renewable energy sources in the electricity market. This problem arises because daily and yearly supply of renewable sources does not match the daily and yearly cycles of energy demand. A large amount of research has been directed towards developing strategies to tackle the intermittent availability of power supply generated from weather-dependent energy sources. The next section presents a literature review in this regard.

2.2. Hybrid systems: A literature review

Studies have shown that proper system sizing is directly connected to the need for balancing energy and reducing cost. Broadly speaking, three sizing approaches can be differentiated based on the fraction of renewable energy in the system (a) no renewable energy surplus, (b) optimal cost and (c) no renewable energy shortage [8].

- (a) In the first approach, renewable energy sources are sized such that no energy is produced in excess. The investment cost is low since no storage is required and the green factor¹ is also low as the renewable energy penetration is limited. To guarantee security of supply, these systems must be supported by the grid or diesel generators.
- (b) The second approach aims at designing a system with the lowest operational cost. The point at which an extra kWh from renewable energy becomes higher than the cost of the dispatchable energy determines the system size. This point can vary widely depending on the system characteristics such as the type of renewable source and whether or not the system is grid-connected. In general, this strategy will lead to low investment cost and possibly low green factor.
- (c) The third approach runs fully on renewables which implies that an important fraction of energy is stored during periods with high availability of weather-dependent sources. This configuration has the highest investment costs and the lowest operational costs, thus possibly is the most attractive option if the system life turns to be longer than expected [42][8]. When not designed properly, this approach can lead to large amounts of lost energy. Although this approach has the highest green factor, it is not necessarily the most energy efficient.

This classification provides some insights on the consequences that the mismatch between production and consumption cycles entails. The daily cycles of supply and demand determine the amount of renewable energy that has to be stored while the amount of energy that is lost depends on the yearly cycles. For this reason, optimal system sizing is extremely site-specific.

Other sizing methodologies found in literature employ the concepts of Levelized Cost of Energy (LCOE) and Loss of Power Supply Probability (LPSP), a measure of the probability that insufficient power supply results when the hybrid system is unable to satisfy the load demand [55][56]. When applied to mathematical models describing the power production of a hybrid system, these criterion are used to quantify system reliability and economic feasibility. The rationale behind the LPSP technique is to obtain the set of system configurations that can meet the desired system reliability requirement. The optimum configuration is the one with the lowest LCOE from the obtained set. Different optimization techniques are reported in literature such as linear programming, iterative approach, dynamic programming and genetic algorithm. The used technique depends on the choice of optimization decision variables, namely the sizing parameters (degrees of freedom of the system configuration). Most simulations reported in literature consider the number and type of generation units and the storage capacity as sizing parameters [9][14][55][56]. A number of factors affect the results reported in literature: (a) the characteristics of the site, (b) the load profile, (c) the solar panel and wind turbine technology, (d) the selected storage and modeling technique, and (e) the input capital costs for the economical assessment. Differences among factors (a)-(e) are the reason why published results must be evaluated carefully. Nonetheless, these studies provide a relevant indication of the common characteristics of in hybrid system combining wind and solar resources. From the reviewed literature [9][14][47][55] and [56], the following commonalities have been found:

¹The green factor relates to the fraction of energy generated from renewable sources in the overall energy output of a system.

- For systems configurations where the energy excess fraction is low, the load is not always satisfied. A LPSP of 0 cannot be guaranteed and, because loss of supply may occur, a dispatchable energy source is needed.
- For system configurations where total renewable contribution is achieved, more than 30% of the generated energy is dumped. In essence, a LPSP of 0 can only be guaranteed with very large storage capacity. This finding cannot be generalized for all system sizes and weather conditions because is limited by the coverage of this literature review. The very fact that agreement was found among the reviewed studies is relevant.
- In general, a decrease in renewable energy contribution, decreases the amount of energy lost. Renewable contribution increases linearly with the generating capacity of the system and is independent of the battery capacity.
- Lowest system LCOE values correspond to storage with double the capacity of daily average consumption if a LPSP of 0 is considered. Relaxing system reliability to a LPSP of 1% could reduce the storage capacity to half and a LPSP of 5% could reduce it to one fourth.
- Lowest system LCOE corresponds to excess energy around 45% if total renewable contribution is considered, namely LPSP is zero. A reduction of excess energy comes with an increase in LCOE.
- All studies show that hybrid systems combining wind and solar are preferred over only wind or only solar. The combination of both resources provide a more balanced supply which helps bridge the gap at times when one of the resources is affected by intermittency. In general, systems with a high installed capacity of solar energy will require a higher supplemental supply over the parts of the day where solar energy is not available. Hence, hybrid systems dominated by wind energy production will possibly show better complementarity of power supply.
- Optimization of module tilt angle can reduce the substantial contribution of solar energy in the excess energy fraction. If the yearly supply and demand cycles are considered, the module tilt angle can be tuned to maximize generation during the period of lowest solar availability or the period of highest demand
- Oversizing renewable energy production makes the system more cost-effective by minimizing the need for expensive diesel generation and storage but results in large amounts of excess energy. When off-grid, this large amount of clean electricity is lost. When connecting the system to the grid, this excess energy can be injected in the grid making the electricity market more green in general terms.

2.2.1. Modeling softwares

In addition to the optimization methodologies discussed above, there are commercially available optimization softwares that model the configuration of microgrids based on user-defined input parameters. The HOMER (Hybrid Optimization Model for Electric Renewables) energy model is one of the most popular and has proved to be useful in exploring the techno-economic potential of microgrids with high penetration of renewables [47]. Other modeling tools include EnergyPlan, which does not take cost into consideration, and H2RES which is limited to off-grid systems. There are many other available tools that investigate the optimal integration of renewables. Nonetheless, these models behave as black boxes and they are not suitable for this research. A fundamental part of this study is to describe the connection between the meteorological information of the particular site and the actual wind and irradiation resources available for power production, and use the results to tune the model. Including the necessary corrections to the model is paramount in order to increase the accuracy of the model and determine whether the *Energy Wall* concept is a feasible project both energetically and economically. Commercial softwares are thus not used in this research due to their limitations when it comes to capturing the diverse particularities of real urban environments.

2.3. Characteristics of urban-integrated energy systems

The studies reported in literature and the available software tools are useful to generate a basis of comparison for modeling techniques and optimization strategies in terms of system sizing. However, most of the presented systems have a scale different to that of the *Energy Wall* and are targeted for areas with greater wind speeds and/or higher solar irradiation. As a matter of fact, the significance of system scale is of great

importance and should not be overlooked. Energy technologies used in distributed applications have performance and reliability challenges different from utility-scale. These are the attributes that set urban-scale apart from utility-scale:

- Different generation capabilities; urban distributed energy systems differ in physical size from utility-scale plants, which has a direct impact on its energy generation potential.
- Less predictability; small scale distributed energy generation is subject to higher fluctuations and uncertainty due to the strong influence of local characteristics and the generally less ideal conditions of the site.
- Proximity to end-use; distributed energy systems are installed at or near the point of end-use for the purpose of either meeting onsite energy demand or supporting operation of the existing distribution grid [6].
- Compatibility with current infrastructure; distributed energy systems don't require new communication and transmission networks as they can take advantage of the available capacity of local distribution grids.
- Strengthened energy independence; distributed energy generation decreases the dependence of a city on energy imports.
- Improved social well-being; the economical and social benefits of distributed energy projects stay local and shape the cultural identity of a city.
- Increased wind energy in the public eye; familiarity can dispel concerns and misinformation promoted extensively by opponents of wind power leading to greater acceptance and deployment [6].

The central idea of urban-integrated energy systems lies in recognizing the inherent complexity of urban renewable energy resources, their challenges and their distinctiveness among different urban areas. Compared to utility scale, a knowledge gap exists when it comes to accurately estimating the energetic potential of hybrid systems integrated in the urban environment. There is still limited experience, and empirical evidence is needed to verify the theory and understand practical considerations that theoretical principles fail to capture. In the race to bridge this knowledge gap, solar energy is clearly in the lead.

Distributed residential and non-residential photovoltaic systems have grown steadily in size since 1998 partly due to the increase in module efficiencies [18]. According to National Renewable Energy Laboratory (NREL)'s models, solar photovoltaic system costs have seen a reduction between 60% and 80% across sectors since 2009 [45]. Not only prices have been reducing but also becoming less variable across projects. In the ninth edition of Lawrence Berkeley National Laboratory (LBNL)'s *Tracking the Sun* report series it was shown that installed prices have been slowly but steadily converging. The results were based on project-level data from 450,000 residential and non-residential PV systems. The reasons were; a maturing market stimulated by increased competition among installers and vendors and better-informed customers.

The various forms of research initiatives and policy support that have been fruitful in growing the solar market have had the unintended consequence of retarding the growth of distributed wind market [6]. In addition, wind energy research, development and deployment programs have been heavily focused on funding and reducing the costs of large wind turbines [6]. As a result, small wind and medium wind technology is lagging behind in both technical and market development. In fact, since its high point in 2012, distributed wind has experienced a decline in capacity additions and investment [48]. This trend is a consequence of a decrease in incentives and supportive schemes magnified by the low retail electricity costs and the increased competition of photovoltaic technologies. The volatility in installed prices also reflects this trend, which can be observed in the wide cost ranges found in small wind cost benchmarks like the one prepared by the Pacific Northwest National Laboratory (PNNL) [2]. Contributing to an even larger price variability, their results were based on a relatively small sample size of 70 new small wind projects and uneven geographic representation.

Clearly, the scenario for distributed wind is different and requires a different treatment than its solar counterpart. Consistent with this claim, the presented study has heavily concentrated in understanding urban

wind energy and producing a model with the finest detail and accuracy to then utilize it to recognize barriers and make recommendations for future development. Having discussed the distinctiveness of urban-integrated energy systems in general, the next chapter zooms in to describe the urban area taken as base case for the hybrid energy system studied in this paper.

3

Study Area and Experimental Setup

The study area taken as the base case for this thesis is introduced in this chapter. A complete description of the available solar and wind resources at the site is provided in the first section. Terrain and roadway topologies and their effect on the local wind resources are described. The next two sections examine the implications of wind flow estimation within the urban boundary layer. A review of flow around bodies theory is provided to explain the potential wind-concentrator effect of a noise-barrier. This is important as it serves as the basis for the correct interpretation of experimental setup and data presented thereafter. Wind gradient data is elaborated to characterize the effect of the noise barrier on the flow. The last section delves into the parameterization of the area's surface roughness aerodynamics.

3.1. Study area

The crossing between the road N-470 and the highway A-13 (E-19) is located southeast of Delft, in the Netherlands. The maximum vehicle speed allowed in this junction is 50 km/h. A noise-cancelling barrier, predominantly facing South, was built along the junction to protect the Emerald district from noise and traffic pollution. Near the roundabout, the noise-barrier is easily accessible making it a strategic point where to install the experimental setup. The space between the roadway and the noise-barrier is 10 meters. The settings and orientation of this noise-barrier sector is favorable for both the study of wind flow development and solar panel performance as it will be explained in the following sections.



Figure 3.1: Study area and noise-barrier section in yellow.

3.1.1. Description of resources

To characterize the potential of the site, a study of the available wind and solar resources has been performed. Hourly meteorological data has been retrieved from Meteonorm®, a climate database that generates accurate typical years combining weather station and geostationary satellite data. The platform takes standard time periods 1991-2010 for irradiation data and 2000-2009 for wind data in its models to calculate the typical years. Global horizontal irradiance (GHI) and ambient temperature records are displayed in Figure 3.2. The seasonal pattern is visible and correlation is observed between both parameters. The total annual GHI is 1040 kW/m, the maximum and minimum temperatures are 31.4°C and -7.8°C.

Figure 3.3 displays hourly wind speeds throughout a year at a reference height of 10m. The mean wind speed is 3.84 m/s which can be considered a medium to low wind speed for wind energy applications. Maximum gusts records reach 16.4 m/s and no seasonal pattern is observed. Elaborating the data, the speed duration curve in Figure 3.4 is obtained. This curve serves as an indication of the amount of hours a turbine sitting in this particular site will operate at speeds between 0 and 4 m/s. Sure enough, performance at low

speeds is the most important parameter of urban wind turbines. Figure 3.5 shows wind direction frequency over the typical year at different wind speeds. The prevailing wind direction is southwest, therefore, a significant fraction of the wind will approach the experimental setup perpendicularly. This fact is important because in order to characterize the effect of the noise barrier on the incident wind, a great amount of clean upwind flow data is necessary.

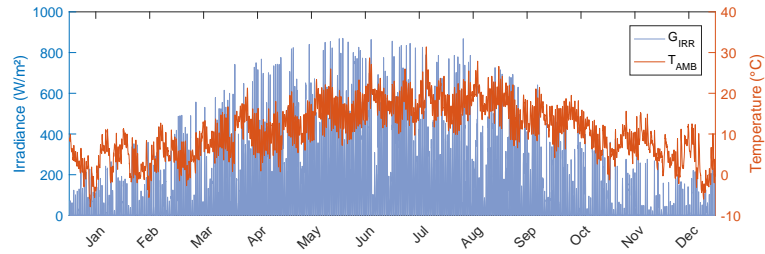


Figure 3.2: Hourly records of typical Meteonorm® year annual global irradiance (GHI) and ambient temperature.

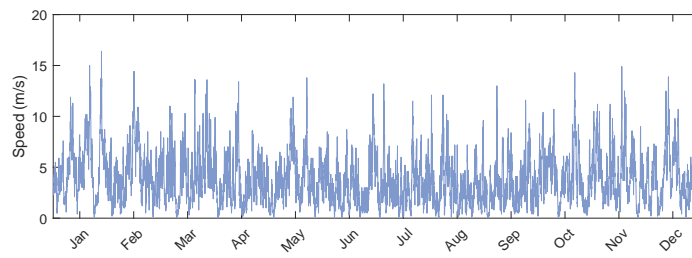


Figure 3.3: Hourly records of typical Meteonorm® year wind speed.

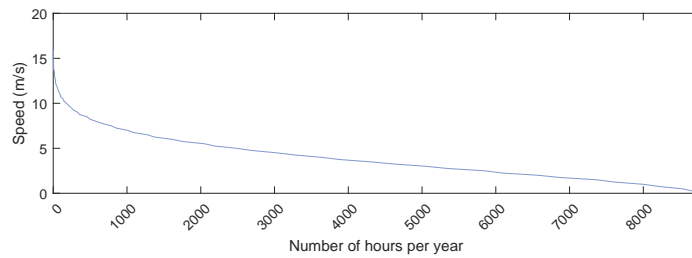


Figure 3.4: Distribution of wind speeds as a function of the cumulative number of hours the wind speed exceeds a given wind speed.

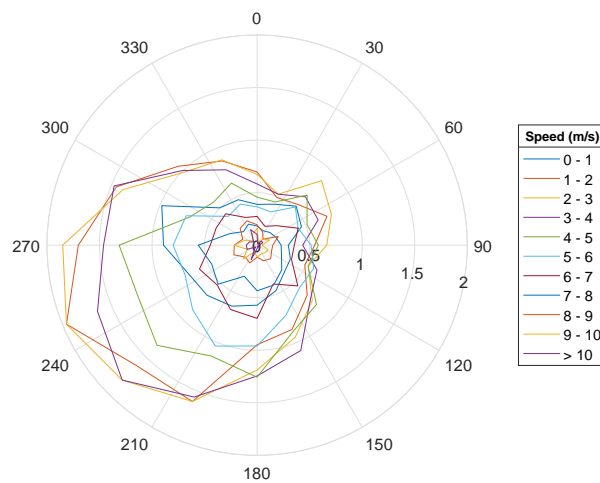


Figure 3.5: Distribution of wind speed and direction over the period of one year, radial scale in % of time.

3.1.2. Terrain topology

The land in close proximity to the study area is fairly open. The noise barrier sits at a distance of 10 meters from the road, on a slightly elevated part of the intersection; the terrain is otherwise flat. A small group of trees in the South direction represent the closest obstacle. The group of low buildings Southeast of the roundabout is an industrial parcel. At the opposite site of the A-13 there is the start of the Delft University of Technology campus. A selection of shoots in Figure 3.6 provide a more realistic impression of the near-road area. The characteristics of the roadway itself may influence and modify airflows and turbulence. Wind velocity field in the vicinity of roads differs from that over natural surfaces [39]. According to the study reported in [46], velocity fluctuations near a roadway are due to three distinct causes,

- Wake turbulence
- Ambient turbulence
- Wake-passing effect

The wake-passing effect is the time variation in wind speed as a vehicle's wake passes a fixed point. This effect cannot be easily separated from the other two fluctuations in real world conditions where vehicles drive at randomly distributed times. To observe the changes in speed caused by moving vehicles, the study conducted in [46] performed a series of controlled anemometric measurements on groups of cars driving at 80 km/h in intervals of 29 seconds at different distances from the road. The results showed that variations in the vertical wind component were only detectable immediately next to the road. Variations in the horizontal components were a function of distance to the roadway. At 3.8 m from the roadway, the effect was more significant for the along-wind component showing a decrease from the reference ambient velocity in the range of 0.17 m/s at a 5-meter height. Further away, at 15 m from the roadway, the effect on both along- and cross- wind horizontal components at the same height above the ground was even smaller [46]. Given the complexity of carrying out turbulence measurements adjacent to motorways and the relatively small effect that the intensity and range of vehicle-induced turbulence seems to have, this effect is considered negligible in this study. This assumption, however, may not be valid for noise-barriers installed within 3.8 m from a high speed (< 80 km/h) roadway with high traffic density (< 1365 cars per lane per hour) as the wake-passing effect may play a role.

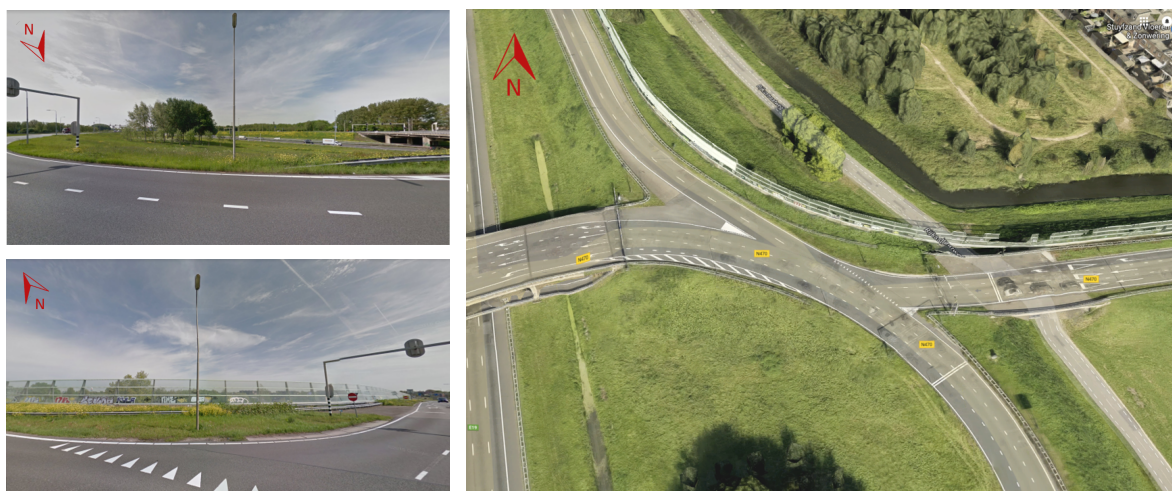


Figure 3.6: Terrain and near-surface characteristics of the study area. Map data ©2018 Google.

The area of study lays within the urban boundary layer. Airflow within this layer is continuously encountering changes in surface roughness. The parameter used in vertical wind profile equations to capture the effect of surface roughness is the roughness length (z_0) and zero displacement (d_0). Values of z_0 and d_0 are not readily available for this site. Hence, an analytical method is used to estimate this parameter based on the acquired on-site data. The importance of properly characterizing the site were a wind turbine will be installed cannot be overemphasized. Terrain features at low height have an influence on the wind characteristics so great that compromise the applicability of the common prediction models for vertical wind speed profiles. The remaining two sections of this chapter examine the implications of estimating wind within the urban boundary layer.

3.2. The urban boundary layer

The urban boundary layer is characterized by wind-obstacle interactions and the resultant highly disturbed airflow. Research into urban wind characteristics has been mainly driven by interest in urban micrometeorology and pollution patterns [27]. Only recently have researchers started to focus on urban wind and its implications in small-scale urban wind power applications. The central challenge lies in the non-uniform characteristics of urban wind flows and the difficulties in estimating expected energy yield in a particular site. This section delves into the aerodynamics of airflow around obstacles explaining it first from a theoretical standpoint and then empirically from field measurements.

Airflow around built forms creates complex air whirls patterns and high turbulence levels which influence the wind speed and direction having a direct impact on its extractable power. Moreover, the many categories of conditions within the surface roughness layer and the various external weather variables make characterization of the urban environment a challenging endeavor. A great amount of airflow data before and just above obstacles, at high sampling frequencies, is necessary when the suitability of wind turbines for urban applications is being considered. In view of this, the next section is intended to provide a theoretical background on flow around bodies which will serve as the basis for the correct interpretation of the experimental data presented afterwards.

3.2.1. Flow around bodies: Theoretical background

In general aerodynamic terms, all bodies cause an acceleration of the free stream wind speed at certain locations close to the body. As distance from the body increases, the velocity approaches free stream wind speed. A rotor close to a body will consequently operate in a spatial non-uniform flow. According to this principle, built forms have the potential to serve as wind concentrators within the urban environment [27]. Realising this potential requires aerodynamical knowledge and strong analytical tools in order to explore the complex concentrator effect of a body on the actual airflow. Mathematical models, measurements and numerical simulations are complementary analysis tools widely used to study aerodynamic phenomenon. In this study, mathematical models and numerical computational fluid dynamics (CFD) calculations reported in literature will be used for the verification of physical observations and model assumptions.

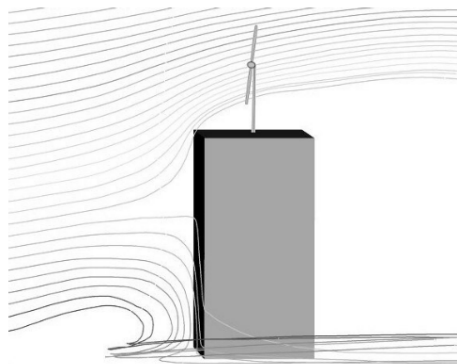


Figure 3.7: Streamlines of airflow around a built form; adapted from [37].

Wind turbines in the proximity of built forms operate in the flow region influenced by such forms. This influence can be observed in Figure 3.7 where the separation of the boundary layer at the sharp upwind edge creates curved streamlines. The curved path is a consequence of the pressure gradient, as the pressure close to the edge is low and increases with increasing distance. Accordingly, the velocities close to the body are high and reduce with increasing distance. This separation creates a distinguished zone of low velocity, highly turbulent and recirculated flow between the curved streamlines and the body's surface. This recirculation region is not wanted for sitting of a wind turbine. The angle resulting from the separation of the boundary layer is referred to as skew angle (γ) and is dependent on the distance from the surface, the roughness of the upwind area, the size and edge rounding of the body and the yaw angle of the free flow approaching the body. The maximum acceleration effect occurs when the free flow is perpendicular to the upwind area. The ratio between free flow velocity and accelerated flow velocity depends on; local surface roughness, building shape, wind direction and height above the roof. The accelerated flow at the body's surface with known local roughness at a given height and wind direction i , can thus be defined in terms of the free stream u_0 and the

relative change in speed C_r as per Equation 3.1,

$$u_i = (1 + C_{r,i}) u_{0,i} \quad (3.1)$$

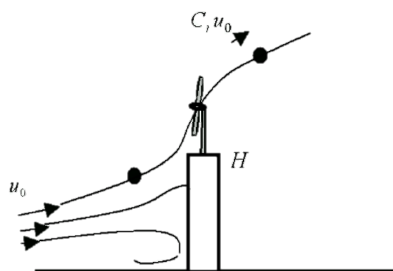


Figure 3.8: Streamline through the rotor; adapted from [37].

In terms of energy generation, a turbine sitting in a region with accelerated wind, will generate power proportional to the cube of the accelerated wind. For instance, if the speed is doubled, the power is increased eightfold. At this point, however, the effect of skewed flow has not been taken into account. A tilt mechanism at the mast to create a normal flow through the rotor increases failure probability and investment costs. Hence, these wind turbines inevitably have to operate in skewed flow. Glauert Momentum Theory shows that maximum power coefficient decreases (C_p) with increasing skew angle (γ) as shown in Figure 3.9

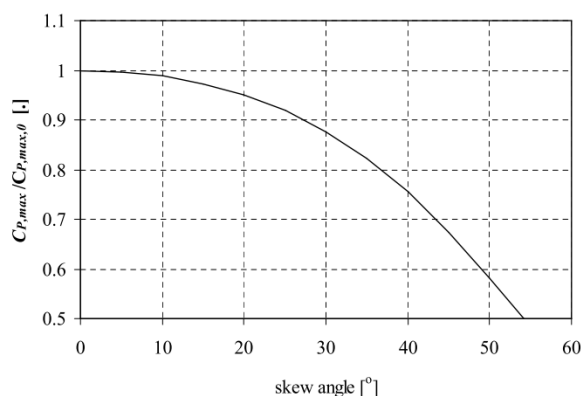


Figure 3.9: Change in maximum C_p as a function of skew angle γ [37]

3.2.2. Flow around bodies: Experimental analysis

The ultimate goal of this experimental analysis is to understand the behavior of low to moderate winds (2-5 m/s) around a noise barrier and explore its wind concentrator effect. Average wind speed information provided by wind speed databases does not include the effect of thermally driven flows and local surface roughness. Hence, access to on-site airflow data is key in modeling urban wind close to built forms such as a noise barrier. Field measurements must be logged and processed meticulously in order to avoid biasing the disturbed nature of the wind speed and direction. This is particularly challenging due to the high turbulence levels of the flow, which translates into the need for high sampling frequencies able to measure the authentic behavior. Specific grouping and categorizing is needed to convert this great amount of airflow data into useful information without jeopardizing the accuracy of the results. Comparing the acquired data with direct observation and judgment is one way to monitor the transparency of the procedure. The methodology followed to log, process and interpret the experimental data is presented in this section.

Data Logging

In order to characterize the flow approaching the turbine rotor, sonic anemometers are mounted on two masts, one before the barrier and the other on top of the barrier. Each setup consists of three anemometers

that have been installed and calibrated for three different heights. Three-dimensional wind velocities measurements have been acquired, post-processed and analyzed in order to understand the interaction between the wind flow and the obstacle. This is important for the turbine sitting on the top of the barrier because the wind captured by the turbine rotor carries the effect of the windbreak. Sonics before the barrier were mounted at a distance of $2H$ from the obstacle, where H is the height of the barrier. This location is referred to as the *clean flow region* as it is intended to log the flow unaffected by the noise barrier. For the purpose of this study, data from the highest sonic level in the clean flow region is termed as *ambient flow*. The mast located on top of the barrier is intended to log the disturbed flow, thus, this location is categorized as *turbulent flow region*. These definitions are sketched in Figure 3.10. Flow characterization is achieved through comparison between the data gathered in these two regions. From the geometrical details of the experimental setup, two flow regimes can be distinguished based on the orientation of the incoming wind direction. As displayed in Figure 3.10, southwesterly winds approach the experimental setup from the clean region onto the turbulent region, where they interfere with the active surface of the noise barrier. This regime of flow is classed as *exposed* and is the flow of interest for this study. Conversely, northwesterly winds are classed as *interference* flow because they encounter the noise barrier first, biasing the measurements logged by the mast in the clean region.

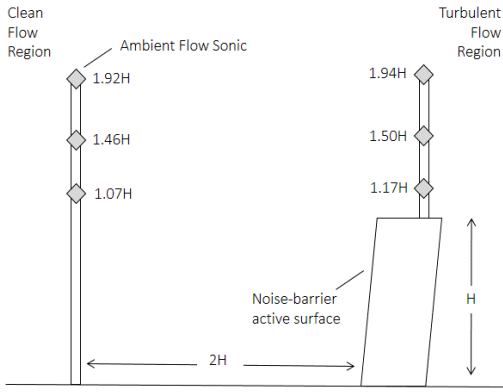


Figure 3.10: Experimental setup definitions

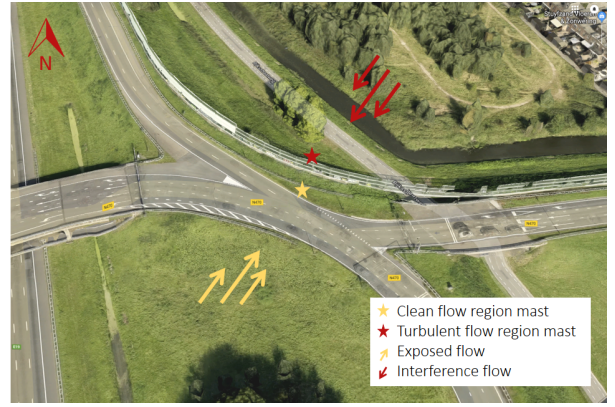


Figure 3.11: Experimental setup on-site.

Calibration of the sonic anemometers is done according to the technical manual [24]. Vector $+U_x$ is defined as towards the direction in line with north, vector $+U_y$ is defined as towards the direction of 90° anti-clockwise from north and vector $+U_z$ is defined as vertically up the mounting shaft. A coordinate rotation is necessary in order to transform the $+U_{xy}$ vectorial wind direction into the classical wind compass domain. This is done by calculating the arc tangent between the vectors $+U_x$ and $-U_y$ where the negative U_y is taken to match the standard Cartesian coordinate system. The resulting angle points towards the direction of the flow with respect to north (grey vector in Figure 3.12). Because winds are commonly characterized by the direction *from* which they are blowing, a 180° shift is applied to obtain the final wind direction used in the analysis and illustrated in Figure 3.12 with the black vector.

Vector wind velocities U_x , U_y and U_z are sampled at 4Hz and written to separate files for each sonic every 2h due to memory limitations. The raw anemometric data have to be elaborated to obtain wind speed magnitude and direction at the desired frequencies. From the three wind velocities components, the resultant wind scalar magnitude (u_{xyz}), the horizontal wind direction (θ) and the skew angle (γ) are calculated with Equations 3.2, 3.3 and 3.4 respectively.

$$u_{xyz} = \sqrt{U_x^2 + U_y^2 + U_z^2} \quad u_{xy} = \sqrt{U_x^2 + U_y^2} \quad (3.2)$$

$$\theta = \arctan\left(\frac{U_z}{U_{xy}}\right) \quad (3.3)$$

$$\gamma = \arctan\left(\frac{-U_y}{U_x}\right) \quad (3.4)$$

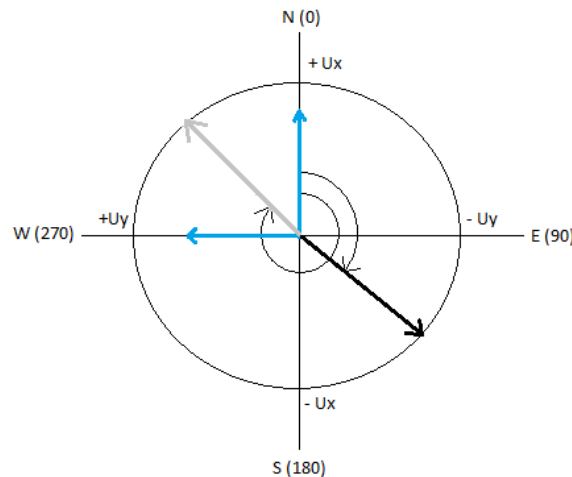


Figure 3.12: Definition of coordinates in anemometer equipment

The importance of correct anemometer installation, orientation and calibration cannot be overemphasized because it provides the basis of the analysis. Any error during this phase will be carried forward and undermine the final results.

Data Processing

The anemometric data is then processed to generate a more suitable dataset for analysis purposes. A number of considerations must be taken in order to develop a data processing methodology that will lead to an accurate representation of the site. These considerations are given below:

- To avoid potential outliers and reduce human-induced calibration errors, a median wind direction is taken as a reference. This value is obtained by computing the median of the wind directions recorded by the 3 anemometers located at the *clean* flow region for each data sample.
- For the purpose of analyzing the concentrator effect of the noise barrier, only upwind *exposed* flow measurements are suitable. Thus, flows outside the 100°-280° arc (*interference* flow) are screened out.
- To establish comparability, measurements from before the barrier are interpolated to match exactly the height of those above the barrier. Assumption is made that data follows a polynomial function.
- To standardize the data, after height interpolation, the 4Hz samples are elaborated into statistics at ten-minute intervals. This has been considered a suitably short time period to enable appropriate analysis of the effect of turbulence on the flow.

A filtering methodology has been developed to clean the anemometric data and remove invalid measurements and outliers. Invalid measurements refer to repeatedly appearing values associated with equipment malfunction whilst outliers refer to values outside a 5 m/s deviation from a windowed mean. The outliers detection algorithm is designed carefully such that the turbulent nature of the flow is not degraded. To convert 4Hz data into ten-minute data, statistics must be conducted in intervals of 2400 (in 10 minutes, the anemometers log 2400 measurements). The filter is based on the percentage of valid 4Hz measurements contained in each of the above mentioned intervals. For example, the number of invalid measurements and/or outliers in one interval is registered and linked to the resulting ten-minute datapoint. A datapoint that derives from an interval with a percentage of outliers and/or invalid measurements greater than 5% is considered 'corrupted' and is directly removed from the sample population. A self-made Matlab® algorithm has been developed to process the data according to the above stated considerations. The various steps taken to clean and standardize the raw data led to the different datasets presented below.

The full data sample includes all 4Hz measurements logged by the anemometers. In total, it consists of roughly 9.5 million data points of the three velocity components over a one-month period between December 11th, 2016 and January 11th, 2017.

The processed data sample, following the detection algorithms for invalid data and outliers, consists of all the calculated statistics for mean wind speed, median horizontal wind direction, median skew angle, standard deviation and turbulence intensity at ten-minute intervals. Additionally, the number of invalid measurements and outliers in each statistical interval is registered. The large 4Hz dataset is reduced to 3947 samples.

The clean data sample is obtained after the exclusion of corrupted data. A corrupted datapoint is defined as a point linked to a percentage of invalid measurements or outliers greater than 5%. A total of 119 corrupted data points were registered by the filtering methodology leaving a sample size of 3828 available for further analysis.

The final analysis data, after screening out the interference flow cases, the sample size is reduced from 3828 to 2745 cases. This data is also referred to as the exposed flow data, as is the flow of interest for this study.

After cleaning and standardization, the final analysis data is categorized per wind direction in 10° intervals resulting in 18 sectors. The centerline for sector 1 is 10° , for sector 2 is 20° , and so on. A second set of statistics is performed for each sector to assess: sector mean wind speed, sector mean change in speed, sector median wind flow tilt, sector standard deviation, and sector turbulence intensity. First, the data is analyzed with no discrimination per wind speed. In a second analysis, the data is discretized in wind speed groups 0-2 m/s, 2-4 m/s and 4-6 m/s. Results from the discretized analysis were not significantly different if compared to the first analysis. This suggested that the acceleration effect of the free stream close to the wall is independent of its speed. Additionally, discretization per wind speeds reduces the number of cases available to conduct the statistical analysis, which in the 4-6 m/s interval are sometimes too small. Based on these two facts, the outcome of the first analysis is used. Hence, generalization of these results to all wind speeds is deemed a suitable estimation for modeling purposes. The investigated parameters are: relative change in wind speed, skew angle, and turbulence intensity.

(A) Relative change in wind speed (m/s)

The relative change in wind speed at a given wind direction i is expressed by $C_{r,i}$ and calculated as per Equation 3.5,

$$C_{r,i} = \frac{u_i}{u_{0,i}} - 1 \quad (3.5)$$

where $u_{0,i}$ represents clean flow region measurements and u_i represents turbulent flow region measurements (which is to say before and above noise barrier measurements, respectively). The obtained results are displayed below in Figure 3.13 for the three different anemometer heights.

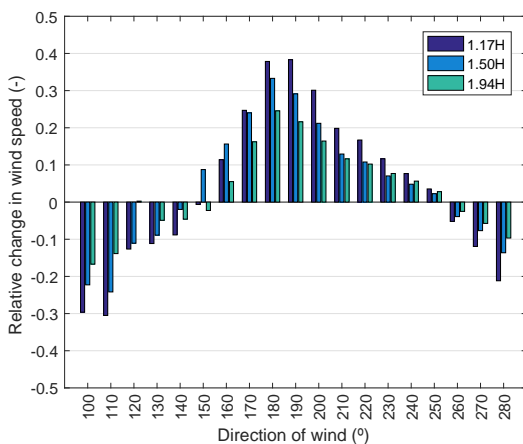


Figure 3.13: Relative increase in wind speed with respect to wind direction.

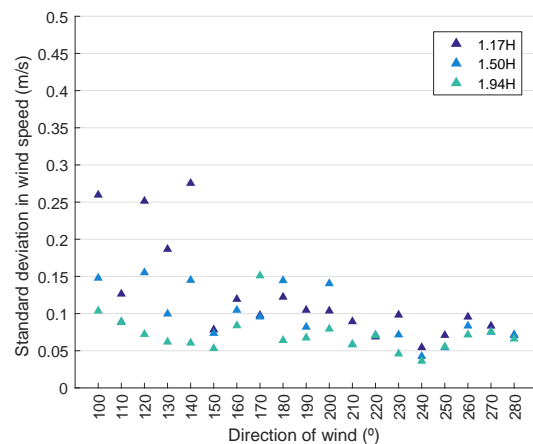


Figure 3.14: Standard deviation of the relative increase in wind speed statistic.

When $C_{r,i}$ is positive, the flow coming from direction i experiences an acceleration effect. Conversely, when $C_{r,i}$ falls below zero, the effect is reversed and the wind speed decreases as a result of the noise barrier interaction. Flows with an incident angle $\pm 20^\circ$ from perpendicular flow (taken as 190°) experience an increase

of roughly 35% at $1.17H$ and 30% at $1.50H$. In contrast, when the incident angle is more than 50° from the perpendicular, the increase becomes zero and also negative in some cases. Parallel flow shows a decrease in wind speed between 10% and 20% and this decrease is higher for eastern winds. The standard deviation of the relative change measurements is reported in Figure 3.14. This parameter reflects how the data concentrates around the mean relative change providing a sense of the uncertainty inherent in the acceleration effect. Standard deviation is overall low suggesting good concentration of the data around the ten-minute mean. This value increases with decreasing height and increasingly eastern wind.

(B) Skew angle ($^\circ$)

The vertical angle of the flow, defined as skew angle (γ) in the previous section, behaves asymmetrically along the arc domain. Figure 3.15 shows significant drop between wind directions 110° and 150° in the measurements before and above the noise-barrier. A similar pattern is observed in Figure 3.16, which displays the wind speed before the noise barrier. In the physical setup, this orientation is aligned with the crossroad between the East lane and the South lane. Therefore, an explanation for this asymmetry could be found in the local layout influencing the free stream as it enters the highway crossing. For the remaining wind directions, the skew angle is broadly similar with roughly 25° , 15° and 10° degrees at heights $1.17H$, $1.50H$ and $1.94H$ respectively. This behavior suggests that the local characteristics of the location influence the southeasterly flow differently from the southwesterly flow resulting in a distinctive wind-obstacle interaction. This result is in agreement with the standard deviation values reported in Figure 3.14 where the wind directions with higher standard deviation match those with lower wind speed.

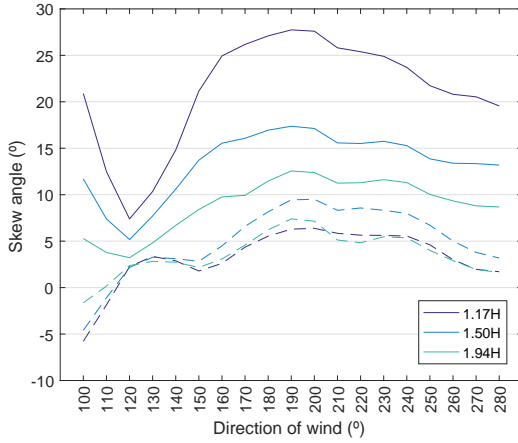


Figure 3.15: Skew angle before noise-barrier (dashed) and above noise-barrier (solid).

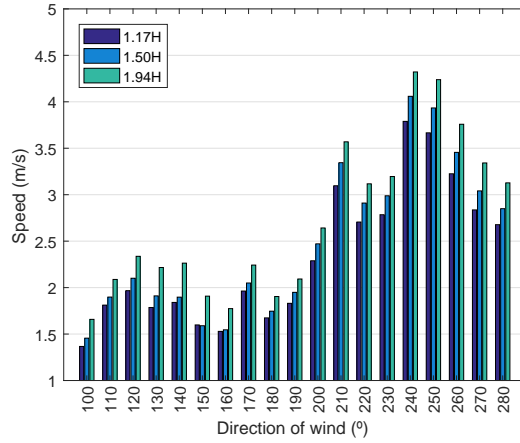


Figure 3.16: Wind speed before noise-barrier.

(C) Turbulence Intensity (%)

The turbulence intensity is the most basic measure of turbulence and is the ratio between the standard deviation of the wind speed and the mean wind speed. Thus, for a given wind direction i , the turbulence intensity is expressed by TI_i and calculated with Equation 3.6,

$$TI_i = \frac{\sigma_{u,i}}{\bar{u}_i} \quad (3.6)$$

where $\sigma_{u,i}$ is the standard deviation of the wind speed and \bar{u}_i is the mean wind speed. All turbulence intensity values given in this analysis correspond to the three-dimensional wind speed vector. The before and above obstacle results can be found in Figure 3.17 for the three different anemometer heights. Turbulence intensity is a location-dependent parameter with values often in the 0.1-0.4 range [29]. The obtained values are within this range except for the southwest end, which reaches values around 0.55 for the lowest anemometer height. This is indeed normal as higher turbulence intensities occur at lower wind speeds. The noise observed in wind directions from 100° to 170° matches the scattered standard deviation values from Figure 3.14. Figure 3.18 shows the relative change in turbulence intensity between the flow before and the flow above the obstacle. To allow and insightful interpretation, the relative change in wind speed is also included. Perpendicular flow experiences a decrease in turbulence intensity, and the opposite behavior is observed as the wind direction approaches parallel flow. This pattern is quite the opposite from that observed in wind speed. This result

is consistent among the three anemometer heights and symmetrical about the centerline defined by the wind direction perpendicular to the noise barrier long-axis. This suggests that there is a relationship between the perpendicularity of the wind-obstacle interaction and the effect of this interaction on turbulence intensity. Results indicate that as wind direction approaches the perpendicular centerline, the speed-up effect of the noise barrier gets stronger and the flow becomes less turbulent. Contrarily, as the wind direction moves away from perpendicular, turbulence intensity increases and the effect on wind speed is reversed. This behavior can be attributed to the formation of recirculation areas, which may slow down the streamline velocity and form complex air swirls. Note that these results relate directly to the particular experimental setup, the local surface and the geometrical characteristics of the studied noise-barrier, therefore, higher order computational fluid dynamics (CFD) calculations would be needed to confirm this inference.

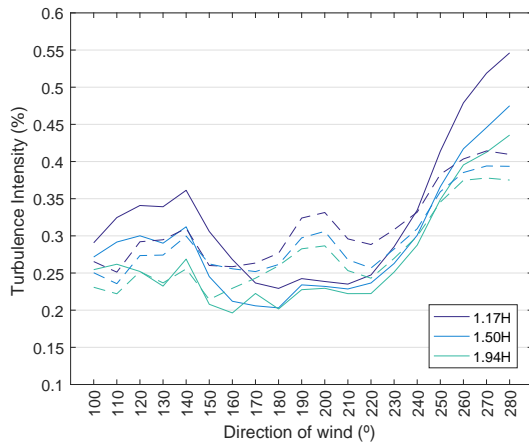


Figure 3.17: Turbulence intensity before (dashed) and above noise-barrier (solid).

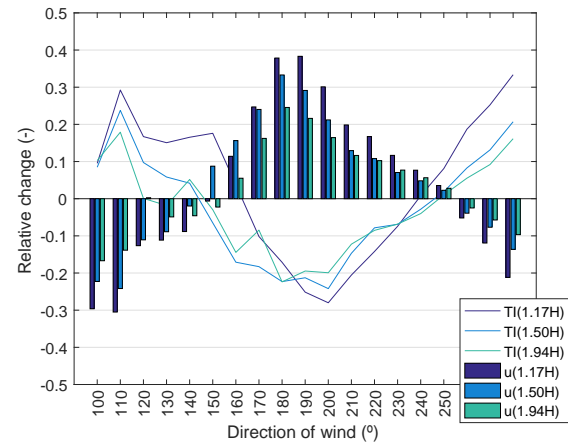


Figure 3.18: Relative change in wind speed and turbulence intensity.

Records of sample sizes are given in Figure 3.19 as a function of wind direction. The aggregated area of the bars is the total sample size containing all post-filter 2745 cases of *exposed flow* statistics. The dominance of the prevailing southwesterly wind is reflected on the number of samples available for the calculation of statistics in each wind direction. The smaller the sample size, the higher the uncertainty of the results obtained for that particular wind direction.

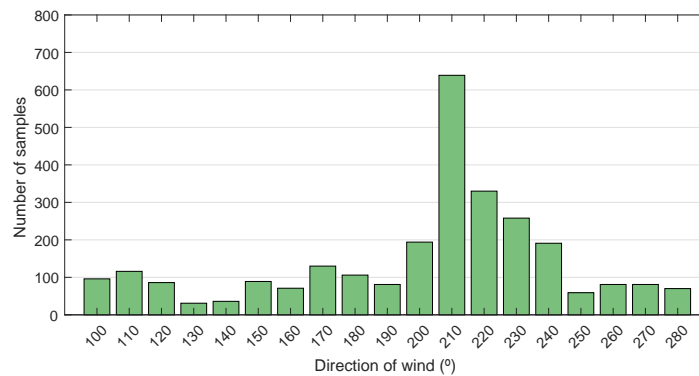


Figure 3.19: Number of samples available for the calculation of statistics in each wind direction

3.2.3. Findings and verification of results

The analysis of wind data for the experimental setup site has provided valuable insight on the complex behavior of airflow around a noise barrier. Two main conclusions can be drawn from these results depending on the angle of incidence of the flow on the obstacle:

- Findings on the perpendicular flow region (within 150°-250°) suggest that the analysis led to sound

results. Acceleration effect and skew angle values are consistent and can be considered for modeling applications. A wind concentrator effect exists in this region. This effect is independent of streamline velocity and strongly correlated with incident wind direction. The results are based on a sufficiently high number of sample occurrences and the standard deviation is between acceptable limits.

- Findings on the parallel flow region (outside 150°-250°) present some inconsistencies at specific wind directions suggesting the influence of local phenomenon in the proximity of the noise barrier. The wind concentrator effect is reversed in this region producing a deceleration of the flow above the noise barrier. The number of occurrences is lower than in the perpendicular case, but high enough to consider this behavior as a true representation of the eastern and western flows.

Although the results of the analysis are seen positively, validation is necessary in order to support the conclusions. Malcolm A. Heath et al [22] identified speed-up levels for different prevailing wind directions at different turbine locations on a modelled pitched-roof house. Their results at a relative height $1.3H$ broadly agree with the pattern observed at $1.50H$ at the site analysed in this study. Disagreement is found at a relative height of $1H$. This discrepancy can be explained with two theories. First, strongly sheared flow characteristic of above-ridge flow making the acceleration effect very dependent on the obstacle shape and the porosity of the material. Second, the fact that the model was based on a suburban neighborhood which differs from the layout and obstacle arrangement at the studied site. Additionally, it can be argued that a maximum exists between the sets of measurements at $1.17H$ and $1.50H$, which would validate the obtained results with the work of Islam Abohela et al. [28] who showed that the accelerating effect was consistent above the height of $1.2H$ with maximum streamwise velocity at $1.3H$ for all investigated cases. Islam Abohela et al [28] conducted a numerical analysis of wind flow above buildings for different heights. Turbulence intensity and streamwise velocity values were normalized against the respective values in an empty domain. Interestingly, the simulation suggested that ground roughness length has an effect on the speed-up level near $1H$ for H equal to 6 m but this effect decreased notably at higher H values. Surface roughness parameters are discussed in the next section. But before, there are two points to be emphasized regarding the correct interpretation of the results from this study:

1. First, the complexity of parameterizing velocity within the urban boundary layer poses limitations on the prediction of speed at a given point, instead, the values refer to a temporal and spatial mean.
2. Second, results are strongly dependent on the site layout and the anemometric data. In this sense, differences on sampling frequency, data processing methodologies and computation techniques of higher order statistics are all possible sources of discrepancy. Therefore, it is impossible to assure that the validity of the results can be extended to a general case.

With this in mind, the results are considered applicable for estimating flow development through an obstacle; but are limited to obstacles with aerodynamic characteristics similar to those of the studied noise barrier. Results from this analysis are used in the next chapter to derive correction factors key for the accurate estimation of wind reaching the rotor swept area.

3.3. Mapping surface roughness parameters

Accurate knowledge of the surface roughness characteristics of a site is vital to describe and model the behavior of urban winds. Unfortunately, maps of surface aerodynamic parameters are not readily available over the studied area and hence a methodology is needed to derive the apparent aerodynamic characteristics of the site. Because terrain is not uniform, the methodology must consider the incoming wind direction. Comparison between different approaches is the only recourse to assess the reasonableness of results due to the difficulty involved in mapping surface roughness, and the absence of a credible standard against which to validate the estimates. Thus, the methodology developed to parameterize the surface aerodynamics of the study area is in reality a combination of quantitative and qualitative approaches. The four approaches presented in this section are: a rule-of-thumb approach, which is often quoted as a first-order guide [10]; a wind-based approach, which takes wind gradient data as input; a comparative approach based on a survey to identify similar cases; and simple visual inspection of the study area.

3.3.1. Aerodynamic characteristics

Surface roughness length (z_0) and zero-displacement (d_0) are the main parameters describing the urban surface geometry. Two additional aspect ratios are widely used in the study of urban surfaces. These are the

front-area density of obstacles (λ_F), which is defined as the ratio between the frontal area of the obstacles to the total surface area, and the plan-area density of obstacles (λ_P), which is defined as the ratio between the plan area of the obstacles to the total surface area [44]. The interdependency between z_0 and d_0 can be understood with the following analogy. Starting from a smooth surface, as the density of obstacles increases, so does the roughness. At some intermediate density, z_0 peaks before the point comes where inter-element spaces are so small that a virtual new surface is created and z_0 starts to decrease. Following this idea, the behavior of d_0 is related to the plan-area density of obstacles (λ_P). A lower bound of the displacement height can be understood as the height of the surface obtained by flattening out all the roughnesses into a smooth surface. Therefore, taking z as the obstacle's height, it follows $d_0/z > \lambda_P$. In this sense, $d_0/z = 0$ if $\lambda_P = 0$ and conversely, $d_0/z = 1$ if $\lambda_P = 1$. This means that for a surface completely covered by obstacles such that $\lambda_P = 1$ then $d_0 = z$ and, because a new smooth surface has been formed, then $z_0 \rightarrow 0$ is expected [44].

In principle, the concepts of z_0 and d_0 are straight forward; in practice, there is a lack in literature of a well-received expression for the calculation of neither parameter. It is for this reason that a methodology combining more than one approach has been implemented in this thesis to estimate the aerodynamic characteristics of the studied area.

Rule-of-thumb

The rule-of-thumb approach relates z_0 and d_0 to the height of the mean height of the roughness elements $\overline{z_H}$ as follows,

$$z_0 = f_0 \cdot \overline{z_H} \quad \text{and} \quad d_0 = f_d \cdot \overline{z_H} \quad (3.7)$$

where f_0 and f_d in urban areas take values around 0.1 and 0.5 respectively [10]. This approach fails to include the effect of density changes and cannot be computed for any direction as it is spatially continuous. However, it serves as a point of reference.

Wind-based approach

Given the availability of multilevel anemometric measurements, an empirical approach to estimate z_0 and d_0 can be derived from wind gradient data. The vertical variation of the mean wind speed at some distance above the surface obstacles is usually well approximated by a semi-logarithmic curve with the added parameter of the displacement height,

$$u(z) = \frac{u^*}{k} \ln \frac{(z - d_0)}{z_0} \quad (3.8)$$

This extension of the classic logarithmic profile applies to cases where roughness elements interfere significantly with each other [44]. The von Karman constant k , is commonly taken as 0.4, and u^* is the friction velocity. Equation 3.8 becomes a straight line on a semi-log graph enabling u^* , z_0 and d_0 to be calculated so long as wind gradient data at three different heights is available. The anemometric measurements on *exposed* flow elaborated in section 3.2.2 are applicable for this study and serve as the $u(z)$ input.

$$\ln(z - d_0) = \frac{k}{u^*} u(z) + \ln z_0 \quad (3.9)$$

From the relationship in Equation 3.9, two different solving techniques, method *A* and *B*, have been implemented. These methods are described in detail below.

(A) Iterative method with linear regression

This method is built on the evidence that d_0 cannot exceed the mean height of roughness elements ($\overline{z_H}$). Therefore, d_0 can be expressed as $d_0 = c \cdot \overline{z_H}$ where the constant c is a number between 0 and 1. Hence, Equation 3.9 can be rewritten as,

$$\ln(z - c \cdot \overline{z_H}) = \frac{k}{u^*} u(z) + \ln z_0 \quad (3.10)$$

The missing value is then the unknown constant c , for which an iterative linear regression technique has been developed and is conceptualized in Figure 3.20. For coherence of the results, all wind gradients that are not monotonically increasing are taken out from the sample. First, a loop is created to iterate through the possible values of c . In every iteration, a linear regression analysis is performed between $\ln(z - c \cdot \overline{z_H})$ and $u(z)$ and the standard error is computed to evaluate goodness of fit. The value of c with smaller standard error is taken as optimal. Knowing c , d_0 can be calculated directly, and z_0 is obtained from the intercept of the fitted line. This process is repeated for each wind gradient data set. Results are then classed in wind direction intervals of 30° and statistics are computed for each wind direction sector.

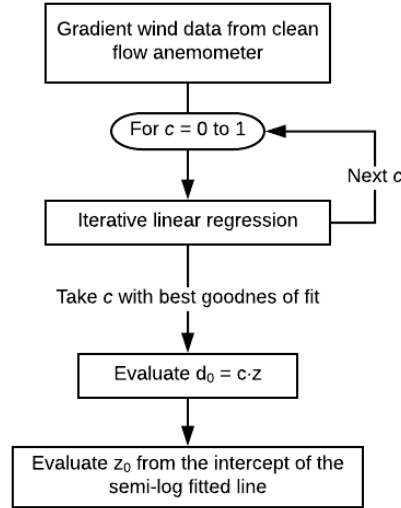


Figure 3.20: Basic steps in method A to estimate surface aerodynamic characteristics.

(B) Implicit method with linear regression

This methodology calculates d_0 implicitly. Given two wind speeds measured at different heights z_1 and z_2 , the following expression can be obtained manipulating Equation 3.9,

$$z_0 = \exp\left(\frac{u(z_2) \ln(z_1 - d_0) - u(z_1) \ln(z_2 - d_0)}{u(z_2) - u(z_1)}\right) \quad (3.11)$$

The same can be done with speeds z_2 and z_3 leading to the implicit equation:

$$\exp\left(\frac{u(z_2) \ln(z_1 - d_0) - u(z_1) \ln(z_2 - d_0)}{u(z_2) - u(z_1)}\right) - \exp\left(\frac{u(z_3) \ln(z_2 - d_0) - u(z_2) \ln(z_3 - d_0)}{u(z_3) - u(z_2)}\right) = 0 \quad (3.12)$$

The function $D(d_0)$ is now defined as,

$$D(d_0) = \left(\frac{u(z_2) \ln(z_1 - d_0) - u(z_1) \ln(z_2 - d_0)}{u(z_2) - u(z_1)}\right) - \left(\frac{u(z_3) \ln(z_2 - d_0) - u(z_2) \ln(z_3 - d_0)}{u(z_3) - u(z_2)}\right) \quad (3.13)$$

Solving $D(d_0) = 0$, gives the value of d_0 . From this point onwards, the remaining steps are the same as in method A. Note that failure to solve $D(d_0) = 0$ occurs when wind speed pairs are too close or when the wind speed gradient is not monotonically increasing. This problem causes a reduction of the number of cases available to perform sectorial statistics, which must be taken into consideration when evaluating the results.

Both solving techniques have been coded using Matlab® leading to the results presented in Table 3.1 and Figures 3.21 and 3.22. There are two important points to be borne in mind when evaluating the outcome of these methods. First, results based on on-site measurements tend to favor the variable but authentically complex nature of wind profiles. Estimates are sensible to surface form, wind direction, and turbulence intensity, which can lead to the absence of strong correlation or expected trends. Second, even when considering all the collected measurements, data remains sparse. Note that the number of cases (n in Table 3.1) that are available to conduct statistical analysis vary between methods and across sectors. This is because on one side, the number of observations are unevenly distributed among incoming wind direction and, on the other side, the input wind gradient data will not always converge to a solution for that particular method. This point is particularly problematic in method B and has led to the omission of some values that were out of a reasonable range. It appears that the implicit function $D(d_0) = 0$ has no solution when $u(z_1) \sim u(z_2)$ or $u(z_2) \sim u(z_3)$.

Based on the linear regression statistics, differences between the two methods are notable. Estimates from method A are based on a larger number of cases which generally leads to a decreased uncertainty in

Sector (°)	Observations	Method A					Method B				
		n	a	b	rmse	r^2	n	a	b	rmse	r^2
90-120	298	270	2.45	-2.35	0.039	0.98	23	3.78	-5.70	0.000	1.00
120-150	156	63	1.45	-0.52	0.035	0.99	3	n/a	n/a	0.000	1.00
150-180	307	260	2.37	-2.18	0.041	0.98	6	n/a	n/a	0.001	1.00
180-210	914	901	2.12	-4.16	0.076	0.96	578	2.34	-5.57	0.000	1.00
210-240	779	771	2.14	-4.16	0.151	0.87	521	2.42	-5.42	0.001	1.00
240-270	221	220	1.21	-1.77	0.129	0.90	32	1.85	-3.88	0.000	1.00
270-300	442	432	1.15	-2.33	0.017	0.99	6	2.99	-3.82	0.001	1.00

Table 3.1: Linear regression statistics for the calculation of d_0 and z_0 using method A and B based on n number of cases out of the total number of observations within each sector. Dimensionless values; mean slope b and intercept a of the linear regression; $rmse$, root mean square error; r^2 coefficient of determination; n/a , not applicable or unreasonable value associated with small n available.

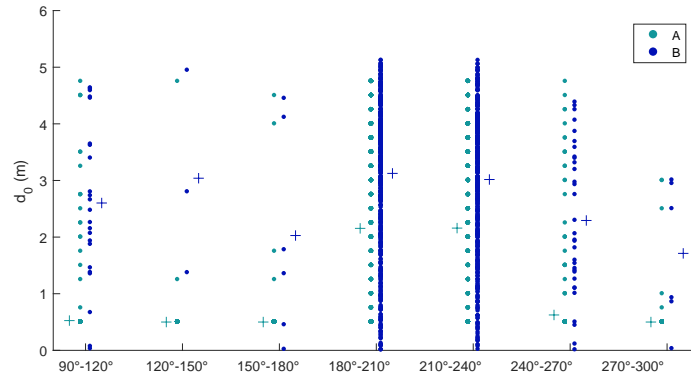


Figure 3.21: Zero displacement scatter plot and statistical mean indicated with the symbol (+) calculated using method A and B based on multilevel anemometric data for seven incoming wind direction sectors.

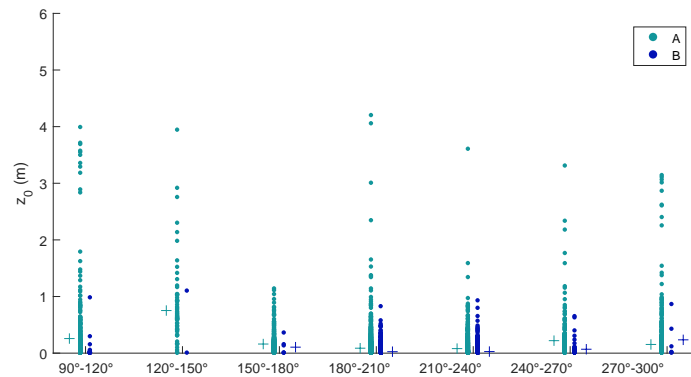


Figure 3.22: Surface roughness length scatter plot and statistical mean indicated with the symbol (+) calculated using method A and B based on multilevel anemometric data for seven incoming wind direction sectors.

the calculation of unknown parameters. At the core of method B is the implicit function $D(d_0) = 0$, which has high selectivity and drastically reduces the number of cases available for the calculation of statistics. As a result, method B is more stringent than method A. This is in reasonable agreement with the r^2 and $rmse$ statistics reported in Table 3.1, where method B stands out for achieving nearly perfect goodness of fit. Comparing the mean values of the linear regression slope (a), estimates from method B are consistently higher but correlation exists between both methods. There is less degree of agreement between intercept estimates (b), although smallest b values correspond to relatively large a values in both methods.

The scatter-plots show some correlation between the two methods, but the data scatter is large. Mean

values are in the same order of magnitude. Method *A* produces mean d_0 estimates in the range 0.5-2.13 m and method *B* in the range 1.71-3.12 m. This suggest that the first method tends to produce slope underestimates leading to smaller zero-displacement values. Conversely, mean z_0 values are in the range 0.09-0.75 m and 0.03-0.24 m for methods *A* and *B* respectively. This indicates that the second method has a bias towards underestimation of linear fit intercepts leading to smaller roughness length estimates.

Comparative survey

A survey has been conducted to identify sites with known surface aerodynamic parameters comparable to the study area in Delft. Among the surveyed locations, a good match was found in a neighborhood in Sacramento, California (3839'N, 21230'W). This location was investigated in [10] as part of a study applied to eleven North American cities to test morphometric methods for the estimation of surface roughness parameters. An aerial photograph is shown in Figure 3.23, next to that of Delft. Both sites display similar density of houses and trees and comparable percent cover. The neighborhood is quoted as a suburban residential area characterized by detached one- to two- story houses surrounded by trees, suburbs and grass. The aspect ratios are $\lambda_P=0.58$ and $\lambda_F = 0.23$ with mean building height of 4.8 ± 0.2 m and mean tree height 6.7 ± 0.5 m. The aerodynamic characteristics of this neighborhood in Sacramento were calculated using various morphometric methods leading to values of z_0 in the range 0.1-1.1 m and d_0 in the range 1.8-4.5 m. These ranges indicate both the variability among direction sectors and the variability artifact of the different methods employed. Such ranges are then taken as the expected upper and lower limit of the results obtained using the wind-based methodologies.

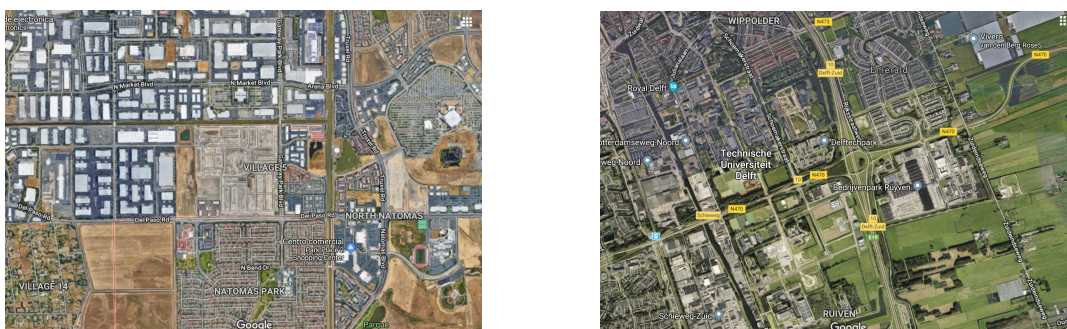


Figure 3.23: Aerial photo of the site in Sacramento (left) and the study area in Delft (right). Map data ©2018 Google.

Visual inspection

Lastly, estimates of the aerodynamic parameters of the area can be obtained from tables of typical values. Visual inspection is one way to validate the wind-based results against the typical values and extend the parameters to the complete arc domain. Table 6 from reference [10] associates different urban surface types with typical ranges of roughness-related parameters and is taken as the basis for comparison. The study area in Delft corresponds to their definition of urban forms of low height and density. In this category, with mean obstacle height between 5-8 m, the typical d_0 and z_0 ranges are 2-4 m and 0.3-0.8 m respectively. Note that according to the reported ranges, the neighborhood of Sacramento falls in the same category.

3.3.2. Concluding remarks

The findings of all four approaches are now put in common to finally map the surface roughness parameters. Because the area studied is mainly characterized by two-story suburban properties and the presence of some medium height bushes and trees, the mean obstacle height $\overline{z_H}$ of is taken as 5 m. This approximation is based on on-site visual assessment supported by the comparative case of the neighborhood of Sacramento. As a result, the rule-of-thumb estimates become $d_0 = 2.5$ m and $z_0 = 0.5$ m, serving as spatial averages and future point of reference. This is in agreement with the midpoints of the ranges reported in the table for typical values, which are 3 m and 0.55 m respectively [10]. In virtue of this observation, the following inferences can be made on the results obtained with the wind-based approach. Method *B*, with an absolute mean $\overline{d_0}$ equal to 2.53 m seems to produce better estimates of d_0 than method *A*. And, while both methods seem to underestimate z_0 , method *A* yields a higher absolute mean $\overline{z_0} = 0.24$ m than method *B*. Thus a decision is made to rely mainly on method *A* for determining z_0 and on method *B* for d_0 . Because *exposed* wind gradient data was

not available in sectors 0° - 30° , 30° - 60° , 60° - 90° , 300° - 330° and 330° - 0° due to the geometrical characteristics of the experimental setup, roughness-related parameters have to be approximated in those five sectors. In the effort to convert these approximations into valid estimates, visual comparison and intuition are the only alternatives. The final surface aerodynamics map is presented in Table 3.2.

Sector ($^\circ$)	d_0 (m)	z_0 (m)
0-30*	2.20	0.18
30-60*	2.30	0.20
60-90*	2.00	0.19
90-120	2.60	0.26
120-150	3.00	0.75
150-180	2.00	0.16
180-210	3.10	0.09
210-240	3.00	0.08
240-270	2.30	0.22
270-300	1.70	0.15
300-330*	1.90	0.18
330-0*	2.00	0.20
Mean	2.34	0.22

Table 3.2: Surface roughness parameters of the study area as a function of direction sector. Experimental data unavailable for the direction sectors marked with asterisk.

From the validation of roughness-related parameters against apparent surface characteristics, two observations can be made. To establish comparability, it is worthwhile recalling the analogy (Section 3.3.1) used to describe the interdependency between roughness length and zero-displacement.

- The smallest z_0 values are found within 180° - 240° and correspond to the largest d_0 values. This area is located southwest of the roundabout and is characterized by a plan-area density lower than the apparent average, which can explain the low surface roughness length values, and few buildings taller than the predefined mean obstacle height, which can justify the rather high zero-displacement values.
- The largest z_0 values occur in sector 120° - 150° corresponding to the industrial parcel located southeast of the roundabout. This sector has virtually the highest plan-area density of the studied area, still within the low-height, low-density urban form type range. It may even be argued that the z_0 peak found in this sector is comparable to the z_0 peak described in the analogy, which occurs at some intermediate density before packing becomes so dense it begins to create a new smooth surface.

Describing the physical form of an inhomogeneous system such as this one is never straight forward. There is irreducible uncertainty in the observation and analysis of wind measurements and the necessary process of simplification of their geometrical behavior. This analysis, however, provides enough evidence to conclude that the derived surface parameters are a fair representation of the surface characteristics of the study area.

4

Modeling methodology

Renewable energy generated by non-dispatchable energy sources like solar and wind is uncontrollable in nature. There is also inherent variability associated with urban environment meteorology. Predictive models of urban-integrated renewable generation combine these two scenarios. How to capture model uncertainty is, therefore, the central challenge. The aim of this chapter is to present the methodology followed in order to develop a model as precise as the intrinsic uncertainty of its elements permit. First, a list of general assumptions is provided to define the context in which the model are developed. The next two sections describe in detail the wind energy generation model and the solar energy generation model in this order. Throughout this chapter, the year-round hourly meteorological data presented in Section 3.1.1 are used as inputs.

4.1. Range of validity

A number of preliminary considerations are required to build a robust basis for the model and define its range of validity. These points are summarized below:

- Variability and unpredictability are intrinsic elements of the model, sources of uncertainty are to be understood and captured rather than smoothed out and simplified.
- The geometrical characteristics of the noise-cancelling barrier located in the study area in Delft is taken as a general case noise barrier.
- The results derived from the wind concentrator effect analysis in section 3.2.2 are considered applicable for predicting flow development around obstacles with aerodynamic characteristics similar to that of the general case noise barrier.
- The noise barrier is considered symmetrical. This assumption affects mainly the correction factors implemented in the urban wind generation model. This simplification arises from the geometric characteristics of the experimental setup, which limits the data applicable for the characterization of wind concentrator effect to only *exposed* flow.
- Above enough height from the ridge of the obstacle the wind concentrator effect is inhibited and the applied correction factors are no longer valid. The highest point at which this effect was investigated is two times the height of the noise-barrier.
- A general case noise barrier at an average inclination of 80° is selected. Statistics have shown that the vast majority of noise barriers are built with an inclination higher than 75° [40].
- The effect of vehicle-induced turbulence is considered negligible for the reasons discussed in section 3.1.2. For noise-barriers installed within 3.8 m from a high speed (< 80 km/h) roadway with high traffic density (< 1365 cars per lane per hour) this assumption, however, may not be valid because the wake-passing effect may play a role.
- Model requirements arise from the fact that the system is to be coupled onto noise-cancelling barriers. The morphology of such structures alongside curvy highways require a highly adaptable and detailed model, offering precise energy generation output as a function of time and also orientation.

4.2. Modeling distributed wind power

The model developed to estimate the energy generated by the wind turbine is introduced in this section. The focus here is quantifying the effect of the urban setting on the wind flow speed and direction, and hence, its potential extractable energy. The challenges involved in the estimation of energy yield in the urban environment can be divided in two. On one hand, determining the mean wind speed of the clean flow around obstacles, and on the other correcting for the local effect of obstacles on the airflow reaching the rotor swept area. Related to the turbine operation, the starting behavior of the turbine and the power curve are two additional aspects that also play an important role on the accuracy of power production estimates. These challenges are explored in depth throughout this section. The main elements of the small-wind model are conceptualized in Figure 4.1 along with the subsection number in which they are treated.

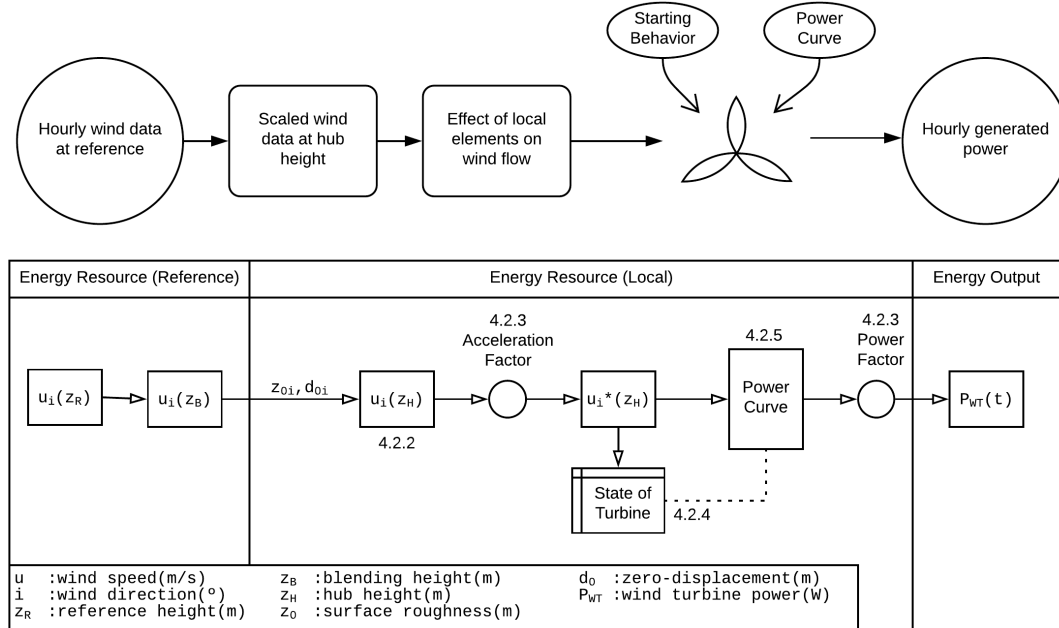


Figure 4.1: Elements in the estimation of wind power production in the urban environment

4.2.1. Model elements

On the basis of a wind energy generation model there is the estimation of windflow speed and direction approaching the rotor area. When wind information from meteorology data centers is used as input for the generation model, scaling is necessary to convert the information from the reference height used by the data center (z_R) to the local height where the turbine is sitting (z_H). Within the urban environment, the flow must also be corrected to capture the influence of nearby obstacles when necessary. To this aim, the outcome of the wind concentrator effect analysis and the knowledge gained through the field measurements is used in this chapter to derive two correction factors: the acceleration factor and the power factor. The first one captures the acceleration effect on the free stream approaching the rotor area resulting in a corrected wind speed. The second corrects for the operation of the turbine in skewed flow. Equally important to the correct estimation of wind is a reliable power curve. Power curves define power output levels over a range of wind speeds, thus, their accuracy is detrimental for the accuracy of the generation model. Manufacturer power curves often lack a reference and lead to overestimates, hence experimental wind tunnel data is necessary for a reliable prediction of turbine power output. The performance of a small turbine in urban environments is also affected by its starting behavior against the short-term fluctuations in wind speed [51]. Cut-in and cut-out levels may blurry at low wind speeds with high turbulence intensity because short-term gust can overcome inertia and enable generation, allowing the turbine to continue to produce even if speed decreases [43]. The methodologies employed to model each of the above described elements follows.

4.2.2. Vertical wind speed profile

The near-surface wind speed is different from the wind higher in the atmosphere due to the influence of the urban morphology. Based on empirical evidence, wind speed experiences a marked speed-up over some short distance above the surface and a more gradual acceleration afterwards. This logarithmic increase in speed is known as shear effect. Because meteorological database speed records are given at a reference height, a boundary layer scaling technique is generally adopted to estimate the wind speed at the height of interest. This technique uses the concept of surface roughness length (z_0) and zero-plane displacement (d_0) to parameterize the frictional effects of surface irregularities on the flow. Correct scaling of wind speeds between two heights is strongly dependent on the accuracy of the available surface aerodynamics parameters describing the area of study. The vertical distribution of mean wind speed is thus described by the semi-empirical logarithmic profile in Equation 4.1, which can be used to extrapolate wind speed levels between two heights z_1 and z_2 ,

$$U(z_2) = U(z_1) \cdot \ln\left(\frac{z_2}{z_0}\right) / \ln\left(\frac{z_1}{z_0}\right) \quad (4.1)$$

The process to scale the wind speed from reference height down to turbine hub height has two steps. First, the reference wind speed is scaled-up vertically to a blending height (z_B) where frictional effects are assumed absent. Next, the wind speed from the blending height is scaled-down to the height of interest [30]. In this sense, the first step reads,

$$U(z_B) = U(z_R) \cdot \ln\left(\frac{z_B}{z_0}\right) / \ln\left(\frac{z_R}{z_0}\right) \quad (4.2)$$

Here z_R and z_0 represent the height and the surface roughness length at which the reference data is measured. Meteorom data is measured at 10 m height over a smooth surface $z_0 = 0.03$ m. The blending height, z_B , is commonly taken as 60 m. For a prospective turbine with hub height z_H , a surface roughness length z_i , a zero-plane displacement d_i and wind direction i , the second step becomes,

$$U(z_H) = U(z_B) \cdot \ln\left(\frac{z_H - d_i}{z_i}\right) / \ln\left(\frac{z_B - d_i}{z_i}\right) \quad (4.3)$$

Equations 4.2 and 4.3 are used in the model in order to scale the reference wind speed according to the surface roughness features of each wind direction interval. Figure 4.2 displays the scaling steps described above. For clarity, only a small interval of 400 hours is shown out of the 8760 hours that make up the complete one-year dataset.

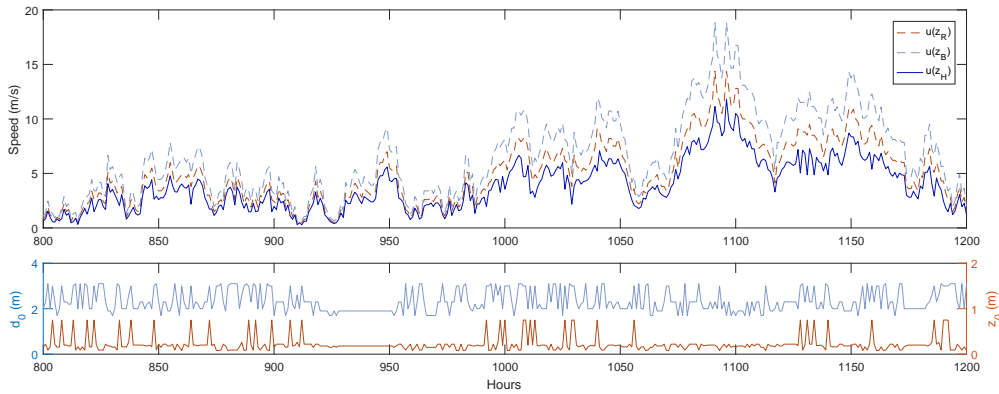


Figure 4.2: Visualization of the boundary layer scaling technique.

4.2.3. Correction factors

The values of the correction factors are based on the results presented in section 3.2.2. The corrections are thus derived from experimental data and have been contrasted with similar studies reported in literature. The speed-up effect is dependent on the angle of incidence of the incoming flow. Aiming to extend the applicability of the generation model to cover noise barriers with different orientation, the relative angle β is introduced to describe the angle of a free flow inciding on the upwind area of a noise barrier. Thus, β is the angle in the

horizontal plane between the direction of the free flow and the azimuth of the barrier¹. For instance, a perfectly perpendicular air stream will have relative angle $\beta = 0^\circ$. This angle has been chosen as the center of symmetry. This decision has been made so that the derived factors can be applied to all noise barriers. Values agree with two important points of the theory presented in section 3.2.1. First, the maximum acceleration factor is found at $\beta = 0^\circ$ where the free flow is perpendicular to the upwind area. Second, the acceleration effect decreases with increasing distance from the edge of the obstacle. The power factor is a function of the skew angle, which is again dependent on the relative angle. Based on [37] and Figure 3.9, the resulting power factors are also reported in Table 4.1.

Relative Angle (β)	-90°	-60°	-30°	0°	+30°	+60°	+90°
Acceleration Factor	-0.02	+0.08	+0.12	+0.30	+0.12	+0.08	-0.02
Skew Angle (γ)	12°	14°	15°	17°	15°	14°	12°
Power Factor	(0.98)	(0.975)	(0.97)	(0.96)	(0.97)	(0.975)	(0.98)

Table 4.1: Correction factors derived experimentally from the nose-barrier wind concentrator effect analysis. Values reported for a height equal to 1.5 the height of the noise-barrier.

It is worth emphasizing that it is impossible to assure that the validity of the results can be extended to a general case. There is a degree of uncertainty inherent in this model and is a direct consequence of the complexity of urban wind patterns. Nonetheless, to reiterate, the aim of this study is to develop a model as precise and realistic as this constraint permits. The correction factors displayed in Table 4.1 cover only half arc domain, a restriction that arises from the coverage of the experimental setup. The extension of the correction factors to the complete arc domain is based on a principle of symmetry. Clearly, this generalization does not apply to all noise barriers, however, all levels of detail in noise barrier designs cannot be captured in the model and some concessions must be made. The impact of this concession on the model accuracy will be minimal for noise barriers with a mirrored configuration and increase with asymmetric noise barriers. The final correction factors are sketched in Figure 4.3 at each the relative angle (β) for the complete arc domain.

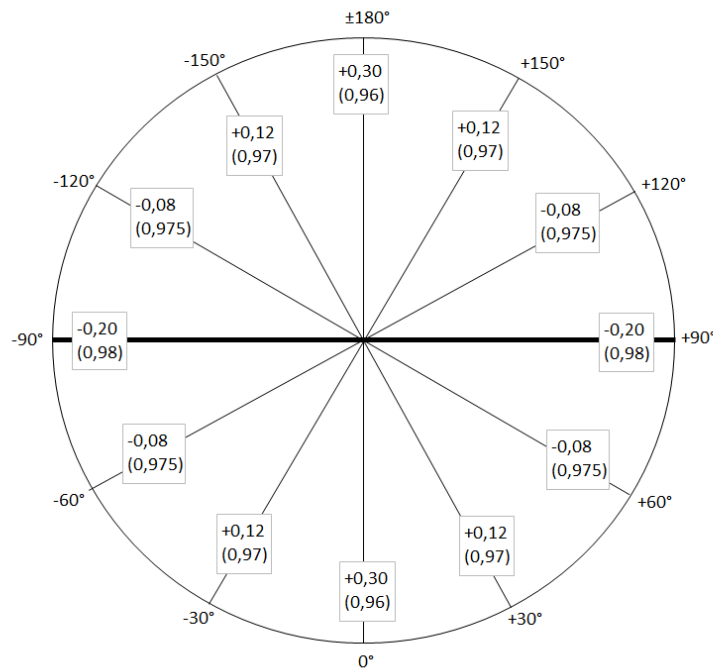


Figure 4.3: Acceleration factor (indicated with + or -) and power factor (indicated between parenthesis) as a function of relative angle β for a 1.5H flow height. Bold line is aligned with the noise barrier long-axis.

¹Azimuth is measured from the north and increasing towards the east.

4.2.4. Starting behavior study

A number of design features define the starting behavior of a wind turbine. Different applications call for different starting patterns. The lowest speed at which the turbine is able to generate power is commonly known as cut-in wind speed. In urban applications, small wind turbines tend to have mean hub height wind speeds close to cut-in speed. As a result, energy generation periods are highly sensitive to this speed level. When manufacturer data is not available, cut-in speeds can be derived through wind tunnel testing. In real operation, however, cut-in levels become blurry. This is the result of short-term wind speed fluctuations, aiding the rotor to overcome inertia. Results from field measurements in [43] concluded that short duration gusts could assist starting. The significance of cut-in speeds should not be underestimated when modeling urban wind generation. To accurately emulate the starting behavior of a particular small turbines, wind tunnel observations testing the many categories of starting conditions would be required. Because access to such experimental data is not guaranteed, a simple algorithm has been developed to emulate this behavior based on three states of the turbine. 'State zero' is always the initial state and corresponds to a non-rotating turbine. 'State one' occurs when the turbine is in survival mode, namely the wind speed is enough to make the rotor rotate but insufficient to overcome internal consumption and start generating energy. The turbine is said to be in 'state two' when energy is being generated. State transitions are illustrated in Figure 4.4 where,

- $start_{sp}$, is the speed at which the turbine starts rotating (3 m/s)
- $stop_{sp}$, is the speed at which the turbine stops rotating (1 m/s)
- cut_{insp} , is the threshold speed at which the generator connects and starts generating energy (4 m/s)
- $idle_{sp}$, is the speed below which the turbine generator disconnects even if the rotor continues to move, the turbine is in survival mode (2.5 m/s)

Wind tunnel measurements for 4 configurations of small wind turbine generators and rotors served as a basis for the estimation of $start_{sp}$, $stop_{sp}$, cut_{insp} and $idle_{sp}$ wind speeds. To mimic the highly disturbed urban wind patterns, power output was monitored at low wind speeds in quick ramp-up and ramp-down sequences. The measurements revealed a good degree of convergence among the tested turbine configurations. These experimentally derived wind speeds are indicated between parenthesis. These values have been considered appropriate for the prediction of the starting behavior of a small wind turbine designed for low speed winds with high turbulence intensity.

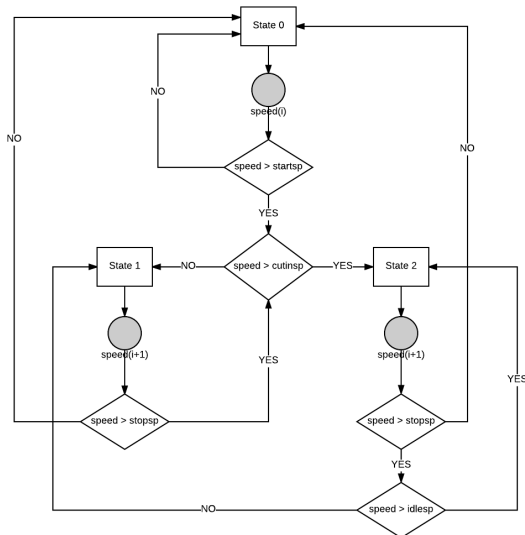


Figure 4.4: Flow block diagram of wind turbine state transition

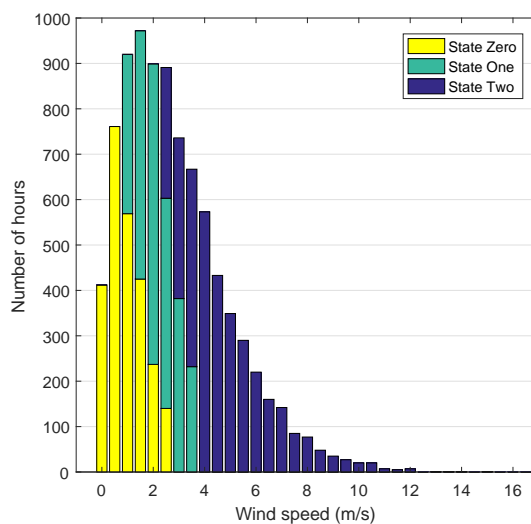


Figure 4.5: Distribution of time spent in each turbine state as a function of wind speed.

This algorithm tries to mimic the true behavior of a rotor affected by sustained short-term wind speed fluctuations [51]. For instance, this feature allows the turbine to remain in 'state two' even after the wind

speed decreases below cut-in, emulating the effect of the inertia stored in the rotor blades. Figure 4.5 illustrates this effect by showing the times the turbine spends in each state as a function of wind speed. The total area of the bars represent the number of hours in a year. Thus, the green area is equal to the number of hours the turbine is visibly spinning but does not generate energy. This demonstrates the sensibility of small wind turbines to cut-in speeds. The performance of a wind turbine at low wind speeds is of utmost importance in urban applications mainly because this speed level covers a substantial amount of their operational time. Proof of this is the wind speed duration curve previously introduced in Figure 3.4.

Merits and limitations of the starting behavior emulator

Meteorological data centers commonly provide year around time-series data at hourly resolution. Hourly wind speed data is unrepresentative of short-time wind speed fluctuations. Clearly, this poses a limitation on the validity of the starting behavior algorithm, as its main objective is to capture the short-term response of the turbine in the face of minute-wise speed fluctuations. With the objective of understanding to what extent this limitation undermines the significance of the emulator, the following steps were taken:

- First, minute-wise wind speed data was obtained from The Royal Netherlands Meteorological Institute (KNMI) upon request. The time series included (not validated and supplemented) mean wind speed values at a ten-minute resolution for the year 2015. The ultimate aim was to establish a comparison, thus the interest was on the resolution of the data and not so much on its quality.
- Next, a second dataset was generated by converting ten-minute data into hourly averages.
- The emulator is then ran: one time using the hourly time series as an input and a second time using the original ten-minute dataset. Comparison between both reveals the impact of running the emulator with time series data at finer resolution.
- The outcome is presented in two manners. First to compare the changes in the distribution of time spent in each state as a function of wind speed (Figure 4.6) and secondly to compare the total amount of time spent in each state (Figure 4.7).
- Results show that, some small differences are observed particularly at speeds 1 m/s, 2.5 m/s and 3.5 m/s and the use of a finer resolution leads to a smoother decrease in number of hours as wind speed increases. By looking at the total amount of time spent in each state is almost the same, only a 1% difference is observed between 'state zero' and 'state one'. In absolute values, both time series lead to the same results for 'state two', which is the state in which energy generation occurs.

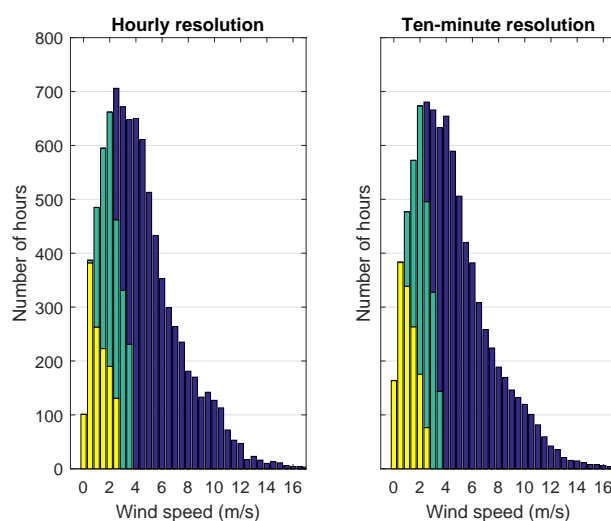


Figure 4.6: Comparison of distribution of time spent in each state as a function of speed using one dataset at two different resolutions.

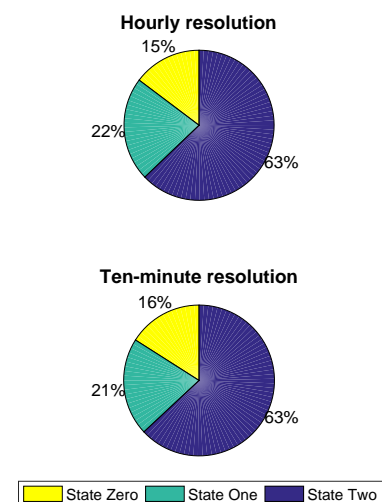


Figure 4.7: State-of-turbine percentages using one dataset at two different resolutions.

By all means, higher-resolution wind speed data leads to a more realistic emulation of the turbine states. Based on this premise, and considering the limited availability of minute data, the following conclusion is reached: results based on hourly datasets are a good overall indication of the behavior of the turbine and provide valuable information for understanding the starting patterns close to cut-in levels. Nonetheless, results should always be interpreted with this limitation in mind and a recommendation is made to use finer minute-wise or second-wise time series data when possible.

4.2.5. The power curve

There is evidence in literature that discrepancies between manufacturer power curves and the actual power conversion capabilities of a urban wind turbine are frequent. Wind tunnel measurements are needed to tune power curves so that they match better with the reality observed. The model employs the WindChallenge® wind turbine model 1.7, a 3-blade horizontal axis urban wind turbine with nameplate power 0.7 kW. The decision criteria were; first, the structural compatibility with the noise barrier; and second, the possibility of testing the turbine and familiarity with the technology.

Interpolation of data from 4 different tunnel tests lead to the final power curve displayed in Figure 4.8. Comparing experimental and manufacturer power curves, three regions can be identified. At low wind speeds below 4.5 m/s, the manufacturer indications exceed the experimental power output. Urban wind turbines operate at those wind speeds a substantial amount of time, thus, accuracy here is of utmost importance. In the middle region, speeds between 4.5 and 8.5 m/s, both curves follow the same pattern with the experimental values slightly above manufacturer specifications. Above 12.5 m/s the manufacturer supplied power curve keeps an upward trend while the experimentally derived values stagnate. This observation agrees with the findings reported in [15], a performance study of 26 urban wind turbines of 4 different manufacturers installed at 5 different sites. The study concluded that more work was required to determine the sources of this discrepancy at high wind speeds [15]. Regardless of this discrepancy, the empirical power curve describes the true operation of the turbine and, therefore, is the one used in the model. Because this curve is representative of after-converter power output, system losses are already taken into account.

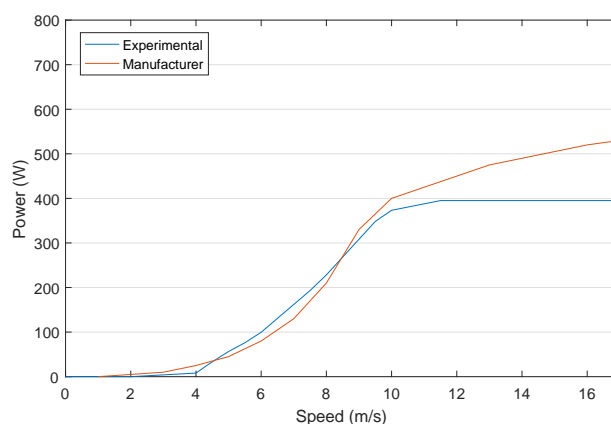


Figure 4.8: Comparison of experimental and manufacturer power curves of the employed turbine.

4.3. Modeling distributed solar power

The model developed to estimate the energy generated by the noise-barrier-integrated solar panels is introduced in this section. The fraction of sunlight beam incident on the surface of the module and the irradiance intensity are two key factors in predicting the output of a solar photovoltaic system. The horizontal global irradiance has to be corrected according to the azimuth and altitude at which PV modules are installed. Related to the module performance, there are some additional factors that can have a significant impact on efficiency namely the combined effect of irradiance and temperature of the module or the presence of dirt or objects blocking the sunbeam. These elements are conceptualized in Figure 4.9 and explored in detail in the following sections.

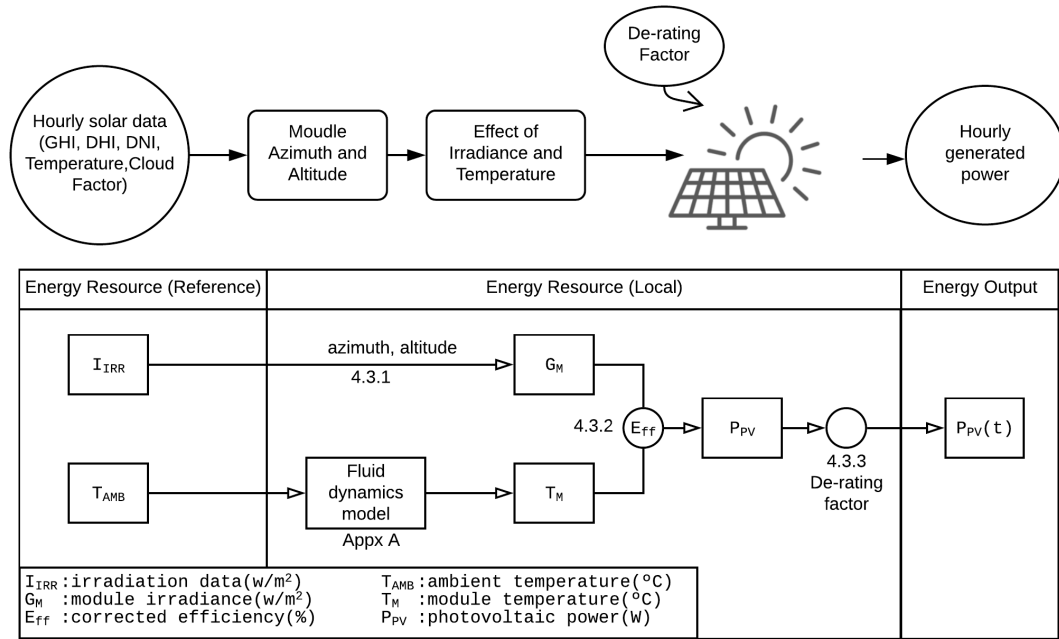


Figure 4.9: Elements in the estimation of solar power production

4.3.1. Model elements

Among the number of factors influencing the output of a solar PV system, the orientation of the panel and the potential benefits of selecting the right altitude are considered first. The orientation should be determined taking into consideration the sunpath and the onsite characteristics such as shadow patterns, however, for systems integrated in the built environment, installation constraints also play a role. Generally, altitude or tilt angle is chosen so that generation is maximized over the year unless mounting limitations are present. Even so, the angle can be tuned to help balance the energy mismatch between generation and consumption. The choice of tilt angle is a degree of freedom that can have a positive impact on the energy output of a hybrid systems. Tuning the angle such that generation is more evenly distributed throughout the year or such that production is maximized for the periods in which the other microsources produce less can prevent shortage and reduce system storage. Figure 4.10 shows yearly generation patterns and annual energy yield for Delft with four different module altitudes. Maximum yearly production is achieved with a module altitude of 55° or what is the same, a 35° tilt angle. A flat module (90° altitude) gives the highest peak during May and June and very low energy yield during December and January. Solar panels coupled onto a general case noise-barrier of a 80° inclination will follow the generation profile of a module altitude of 10° corresponding to the lowest energy yield of the set.

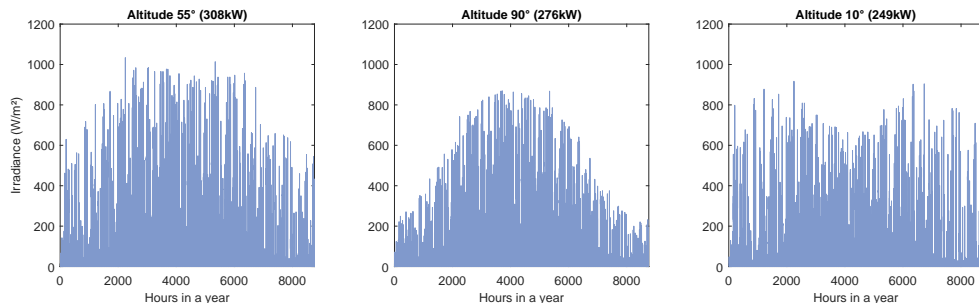


Figure 4.10: Annual distribution of irradiation levels on a surface at three different altitudes. Estimated annual energy yield of one solar module is provided in brackets.

Module azimuth is commonly oriented towards the equator to the possible extent. This is done to maximize the amount of irradiation hitting the PV module over a year. An algorithm has been developed to assess how the incident irradiation levels vary for different module altitude and azimuth. The output of this algorithm for the location in Delft is shown in Figure 4.11. The highest annual incident irradiance corresponds with a South-oriented, 55° altitude module. This contour plot provides insight on how far from the theoretical potential a pv module is operating. For instance, for a general case noise-barrier oriented towards North (dark blue region of the contour plot) the PV system would be operating at half of its full potential.

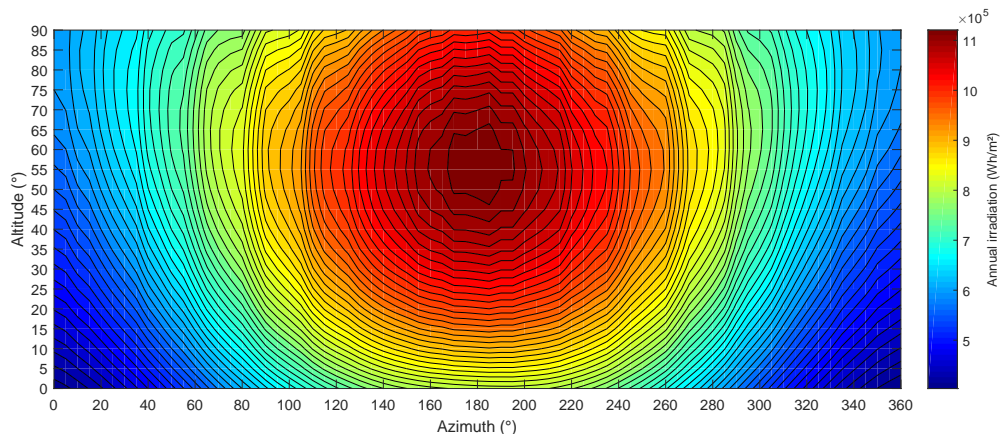


Figure 4.11: Incident annual irradiation as a function of module altitude and azimuth. Hourly irradiation data from Meteornorm® at the location of Delft, the Netherlands.

4.3.2. Effect of temperature and irradiance

Standard Test Conditions (STC) are used by most manufacturers to rate the power output of their solar panels. Efficiency at STC is defined for an incident sunlight of $G_{STC} = 1000 \text{ W/m}^2$, a cell temperature of $T_{STC} = 25^\circ\text{C}$ and a $AM1.5$ air mass spectrum. Because these conditions are generally not representative of the real working conditions of solar modules, accurately estimating the effect of module temperature and incident irradiance on module performance is necessary [5]. Table 4.2 provides a summary of the manufacturer specifications of the employed technology, a commercial Suniva Optimus® series PV module.

Parameter	Symbol	Value
Module efficiency	η_{STC}	17.43 %
Module surface area	A_m	1.95 m^2
Max. Power Point Power	P_{MPP}	340 W
Max. Power Point Voltage	V_{MPP}	37.8 V
Max. Power Point Current	I_{MPP}	8.99 A
Open circuit voltage	V_{OC}	46 V
Short circuit current	I_{SC}	9.78 A
Power temperature coeff.	$\partial P_{MPP} / \partial T$	-0.42 %/°C

Table 4.2: SUNIVA Optimus® monocrystalline solar module specifications at STC.

Knowledge of how the module temperature (T_m) varies with different irradiation levels is important to determine the real efficiency of a solar photovoltaics system. While incident irradiation (G_m) shifts the IV curve upwards and to the right, module temperature has a contrary effect shifting it towards the left. This is because the small increase in short circuit current at higher temperatures is counterbalanced by the decrease in open circuit voltage [5]. Therefore, when studying the performance of a solar panel, both the effect of irradiance and the effect of temperature must be considered. The accurate estimation of module temperature is the first step in adjusting the STC efficiency to match real working conditions. With this purpose, a fluid dynamics model has been employed to estimate the temperature of the module throughout the year. The model is adapted from the work done by [5] and [17] with minor additions, and a detailed explanation is presented in Appendix A. The consequences of accurately estimating module temperature and its effect on PV perfor-

mance are illustrated in Figure 4.12. The curves are normalized to the standard test conditions efficiency η_{STC} and the combined effect of irradiance and temperature can be observed at various light intensities.

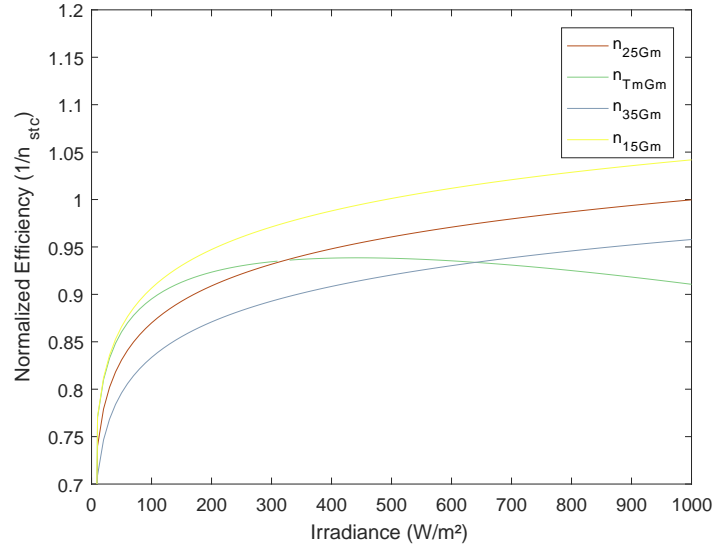


Figure 4.12: Normalized η_{MPP} efficiency as a function of irradiance on module G_m , and for different constant module temperatures T_m , of 25°C (red), 35°C (blue) and 15°C (yellow) and for variable realistic module temperature derived with the fluid-dynamics model (green).

Figure 4.12 highlights the advantages of low-temperature high-irradiance sites for the installation of photovoltaic modules. For a module temperature below 25°C the module will operate at an efficiency higher than η_{STC} (yellow curve) while for a module above this temperature, the efficiency will decline (blue curve). The effect of varying module temperature is only captured by the green curve, where at irradiance levels above 320 W/m^2 , the positive effect of higher irradiance is outweighed by the increase in temperature. In a climate such as the one in the Netherlands, the normal operating conditions correspond to low levels of irradiance and low temperatures. Thus, because of the favorable conditions, solar panels are likely to exceed their rated power output.

Once the temperature of the model is known, the efficiency of the model at real working conditions can be calculated through the three steps provided below.

1. The first step is to quantify the effect of temperature on module performance. Mathematically, this effect is expressed by Equation 4.4,

$$\eta(T_m, G_{STC}) = \eta_{STC} + \frac{\partial \eta}{\partial T} (T_m - T_{STC}) \quad (4.4)$$

where $\partial \eta / \partial T$ is the efficiency temperature coefficient. This parameter is unknown, but it can be calculated from the power temperature coefficient $\partial P_{MPP} / \partial T$. This coefficient is commonly provided by manufacturers as a percentage of P_{MPP} and in this case is equal to -0.42 %/°C.

$$\eta(T_m, G_{STC}) = \frac{P_{MPP}(T_m, G_{STC})}{G_{STC} A_m} \quad (4.5)$$

$$P_{MPP}(T_m, G_{STC}) = P_{MPP} \cdot \left(1 + \frac{\partial P_{MPP}}{\partial T} (T_m - T_{STC})\right) \quad (4.6)$$

2. The effect of irradiance is expressed by Equation 4.7, where $P_{MPP}(T_{STC}, G_m)$ is still unknown.

$$\eta(T_{STC}, G_m) = \frac{P_{MPP}(T_{STC}, G_m)}{G_m A_m} \quad (4.7)$$

To obtain $P_{MPP}(T_{STC}, G_m)$ from the manufacturer specifications, a couple extra steps are needed. Those are described in Equations 4.8 to 4.10 where k_b is the Boltzmann constant, q is the elementary charge and n is the ideality factor taken equal to 1 as suggested in [5]. The fill factor (FF) is the ratio between the maximum power generated by a solar cell and the product of V_{OC} and I_{SC} . The remaining parameters can be found in Table 4.2 above.

$$I_{SC}(T_{STC}, G_m) = I_{SC}(STC) \cdot \frac{G_m}{G_{STC}} \quad (4.8)$$

$$V_{OC}(T_{STC}, G_m) = V_{OC}(STC) + \frac{nk_b T_{STC}}{q} \cdot \ln \frac{G_m}{G_{STC}} \quad (4.9)$$

$$\text{with } k_b = 1.38 \cdot 10^{-23} \text{ JK}^{-1}, q = 1.602 \cdot 10^{-19} \text{ C}$$

$$P_{MPP}(T_{STC}, G_m) = FF \cdot V_{OC}(T_{STC}, G_m) \cdot I_{SC}(T_{STC}, G_m) \quad (4.10)$$

3. Combining the two effects, the efficiency of the module at a specific level of irradiance G_m and module temperature T_m can be calculated with Equation 4.11 below. The key inputs are $\eta(T_{STC}, G_m)$ from Equation 4.7 and the parameter κ which relates to the efficiency temperature coefficient calculated with Equation 4.4.

$$\eta(T_m, G_m) = \eta(T_{STC}, G_m)(1 + \kappa(T_m - T_{STC})) \quad (4.11)$$

$$\kappa = 1/\eta_{STC} \cdot \partial\eta/\partial T \quad (4.12)$$

Typical values of κ can also be found in [5] along with a more detailed explanation on how to derive the expressions introduced above.

4.3.3. Sources of losses

Besides module temperature and irradiance, other effects like accumulated traffic dust can also impact the overall performance of a solar panel. These, and other losses are summarized in Table 4.3 and further discussed below.

Category	Value
Soiling	8%
Shading	1%
Mismatch	2%
Connection	2%
Light-induced degradation	1.5%
Availability	3%
Overall Loss	16.4%

Table 4.3: Breakdown of solar system losses

Given the proximity of the solar panels to traffic, losses due to dirt preventing solar irradiation from reaching the photovoltaic cells are likely. A demonstration project [38] carried out along a noise-barrier monitored the in-plane irradiance of 4 reference cells over a period of two years. The study concluded that soiling was responsible for a 8% reduction of the annual energy production. Observations suggested that the accumulation of dust and its natural cleaning reached equilibrium relatively fast. Based on these results, a 8% de-rating factor is included in the generation model to account for this phenomena. Annual cleaning of the solar panels has been considered as a possible alternative to mitigate the effect of soiling. The benefits of scheduled cleaning are, however, hard to calculate. On one side, besides labor and equipment costs, water consumption for cleaning is around 1 liter/m² of system area. On the other, heavy rains result in a complete cleaning effect for free. In rainy climates, therefore, a cleaning regime is almost never cost-effective [41]. For the reasons above, cleaning is not included as a maintenance cost and the assumption is made that the impact of soiling is well represented in the model by the aforementioned de-rating factor.

In addition to soiling, static and/or dynamic shading can also block irradiation to the cells. An additional 1% loss is included in this regard. Other losses inhibiting the performance of a solar system are; electrical mismatch, which are the losses due to manufacturing imperfections; wiring and connection; light-induced degradation, which is the effect of the reduction in power during the first months of operation caused by degradation of the photovoltaic cells; and availability, which accounts for the scheduled and unscheduled system downtime [32]. Default values from the National Renewable Energy Laboratory (NREL) have been adopted to capture the above set of losses in the model. The breakdown of all system losses is reported in Table 4.3.

On top of the discussed system losses, the efficiency of the DC-to-AC inverter also reduces the output of the solar system. Considering the favorable ambient temperatures of the study area and the rapid advances in the field of power electronics, a 98% conversion efficiency is assumed.

5

Study of the Energy Supply

Efficiently generating energy from renewable sources is the first step in the process of managing energy sustainably. The second step is ensuring the generated energy is efficiently used and waste is minimized. When energy sources are uncontrollable in nature, this step becomes problematic. Solar and wind power generation characteristics are fundamentally different from conventional energy sources because they cannot be adapted to a given electricity demand. Hence, the overriding challenge is pairing energy production with energy consumption profiles. Whether grid-tied, off-grid and/or backed up with storage, an assessment of the generation pattern of a system is important in order to foresee the possibilities and impossibilities of its applications.

In this chapter, the generation models introduced in the previous chapter are coupled together. The output of the hybrid system is assessed in the first section. The next section discusses possible energy uses to then reach a conclusion regarding the most efficient strategy, which is presented in the last section.

5.1. Solar, wind and hybrid generation profiles

To investigate the inherent variability in generation patterns, a statistical analysis has been performed on the hourly generation profiles obtained from the coupling of the two models described in chapter 4. For consistency, the number of solar panels and urban wind turbines is fixed. The choice is based on the structural characteristics of the noise barrier located in the study area. The barrier has a modular design and each segment is 6 meters long. Each segment has a surface area of more than 30 m^2 which is able to fit 12 Suniva Optimus® series OPT-340-Wp solar panels installed in 4 rows and 3 columns. The employed wind turbine is the WindChallenge® model 1.7, a Dutch manufactured urban wind turbine with nameplate power 0.7 kW. The choice of 1 turbine per segment is necessary to allow sufficient spacing between rotors. With 1 turbine per segment and a rotor diameter of 1.7 m, the distance between rotors becomes 4.3 m. From this point onwards, unless stated otherwise, a standard *Energy Wall* segment is south-oriented and has the generation capability of one turbine and 12 solar panels at 80° of inclination according to the specifications mentioned above. The total installed capacity of a single segment is 4.78 kW, from which 4.08 kW are solar power and 0.7 kW are wind power.

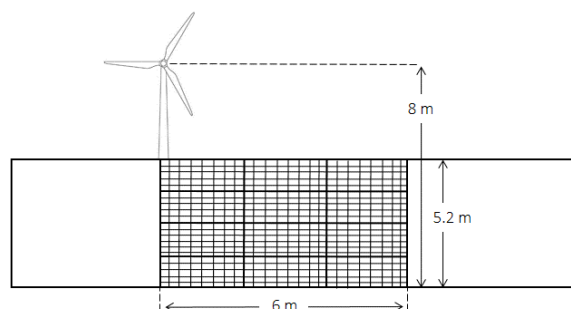


Figure 5.1: Schematic and dimensions of a standard 6-meter *Energy Wall* segment.

The fluctuations of solar and wind energy availability are more visible if annual generation is elaborated into monthly statistics. Instead of analyzing the distribution of generated power over 8760 hours, hourly generation of each month is averaged to obtain 12 generation curves, each one describing the average day of each month of the year. To obtain average daily profiles, generation levels of the same hour in a day are grouped together for each month. Then, the mean and standard deviation of each hour group is calculated leading to 12 average daily generation profiles. In this manner, elements describing the availability of solar and wind energy throughout the year are visible. Note that results are by all means linked to the chosen location in the Netherlands and the meteorological data¹ used as input for the models.

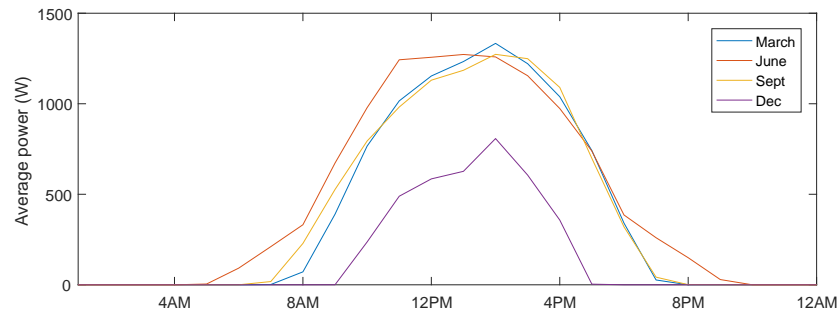


Figure 5.2: Daily distribution of average power generated by 12 solar panels coupled onto the *Energy Wall*.

The distribution of solar power generation over a day has been studied for each month, but only the months of March, June, September and December are shown in Figure 5.2 for clarity. Intuitively, average power becomes zero during night, shaping the typical daily pattern of solar energy. Comparing the power profiles of different months, seasonal variations can be observed. The lowest daily energy generation occurs in December with a peak at 2pm of just above 800-watts, whilst the highest generation takes place in April with a peak above 1630-watts around the same time. The aggregated energy generated during April, May, June and July represent more than half of the total generation of one year. The months of medium generation are March, August, September and October. The remaining months contribute less than 15 % to the annual energy yield. Standard deviation values are a measure of the variability of the described daily patterns within a month. September and February are the months with highest internal variability (up to 1000-watts at times of high irradiance) while the daily generation patterns during May, June and July are statistically more repetitive. The variability of generation patterns between days introduces uncertainty in solar energy predictions. In view of this, the dependency of solar generation on daily and seasonal variations is emphasized and the challenge of balancing supply and demand underlined.

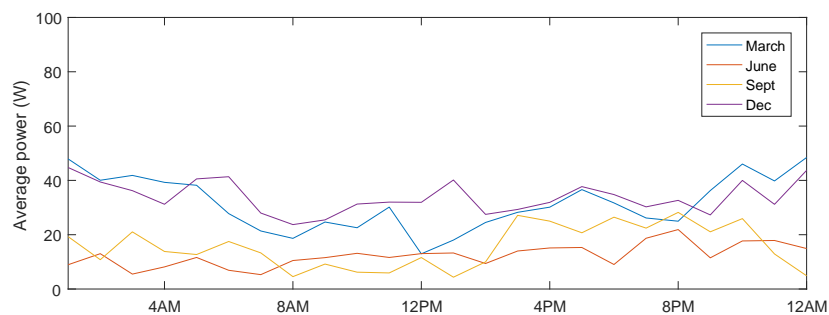


Figure 5.3: Daily distribution of average power generated by one urban wind turbine coupled onto the *Energy Wall*.

The seasonal pattern observed in solar generation is less evident in the distribution of power generated from wind. Results for the studied year are shown in Figure 5.3. Highest and lowest daily generation occur in January and August respectively. The trends of June, July, August and September suggest that, during summer, generation is favored after noon and during night. This observation cannot be made on the remaining months. No real pattern can be derived from the standard deviation values which are higher than the actual

¹Refer to section 3.1.1 for a description of the local meteorology and data resources.

mean in some cases. This is not new considering the characteristics of urban wind flow. From the results, it can be concluded that the energy generated from wind is completely dependent on the prevailing weather conditions, and therefore is more variable and circumstantial than the energy generated from the sun. Even so, the contribution of wind energy is important as it represents the sole source of energy during nighttime.

5.2. Evaluating energy use strategies

Knowledge of the seasonal fluctuations and daily variability of the solar and wind resources available in the study area sets the basis for the second step in the process of managing energy sustainably. This step consists in choosing a strategy that ensures an efficient use of the energy produced with the least losses, and is the main focus of this section.

The proximity of noise barriers to residential areas and/or coupling points with the main electricity grid opens two main possibilities for the utilization of the energy generated by the *Energy Wall*. The first one is seen as an opportunity to shorten the distance between energy production and consumption by supplying suburban electricity demand with near-road generated renewable energy. Suburban demand can take various forms depending on the characteristics of the site. In fairly isolated areas, transportation applications such as road lighting could benefit from near-road generated energy. With increased proximity to residential areas, the load profile diversifies to include applications ranging from vehicle charging to home appliances. The second opportunity is grid-connection. A grid-tied configuration is subject to less stringent requirements as it eliminates the need for balancing supply and demand. Both load supplying and grid-supplying alternatives are valid, but further investigation is necessary to determine which of the two will lead to a greater added value.

5.2.1. Load-supplying against Grid-supplying

To evaluate the matching between the *Energy Wall* generation profile with suburban electricity demand, a typical residential load has been selected for the scope of this analysis among the various near-road electrical load types. Normalized day curves for residential consumers in the Netherlands have been adapted from [50]. The demand is representative for an annual electricity consumption of 3400 kWh. The load curves of Figure 5.4 have been interpolated to obtain the profiles of the remaining months.

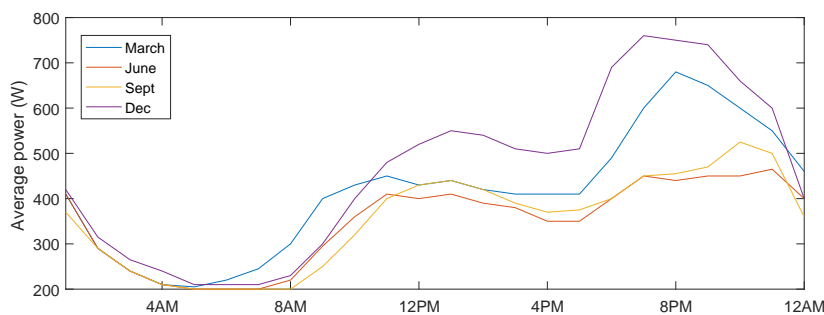


Figure 5.4: Daily aggregated load for common electricity use for a residential household with annual electricity demand of 3400 kWh

The electricity supplied by the *Energy Wall*, merging solar and wind energy production, is compared with a typical suburban electricity. The objective of comparing supply and demand is to understand and measure the effect of daily and seasonal energy imbalances. The daily imbalance can be observed in Figure 5.5 where only four months are shown and both curves represent an average day in that particular month. Energy mismatch is dominated by the night-day pattern intrinsic in solar energy. This is expected, because the penetration of solar power in the system is strong. For instance, during an average day in December, the gap between consumption and production reaches 5.8 kW, which gives an idea of the short-term storage requirements of the system. Figure 5.6 captures the yearly imbalance and gives a rough idea of the long-term storage requirements. Between March and September, summer season, the aggregated monthly generation is sufficient to supply the demand. The maximum is reached in April, with roughly 100 kWh of energy surplus. This is not the case during winter season. The energy generated throughout the month of December, is 200 kWh short of the demand. Ultimately, at the end of one year, a system of 12 solar panels and one small wind

turbine generates 3227 kWh, only 178 kWh short from covering the demand of a typical dutch residential household. The problem is, the disconnection between the times at which energy is produced and the times at which is demanded. Analysis of the energy imbalance for the full year sheds light on the possibilities and impossibilities of energy management strategies suitable for a system of these characteristics. Energy management strategies aim to optimize energy usage and guide the flow of energy through a system in the best possible manner. Good energy management practices are able to maximize utilization of renewable sources, minimize cost of energy, and ensure continuity of supply.

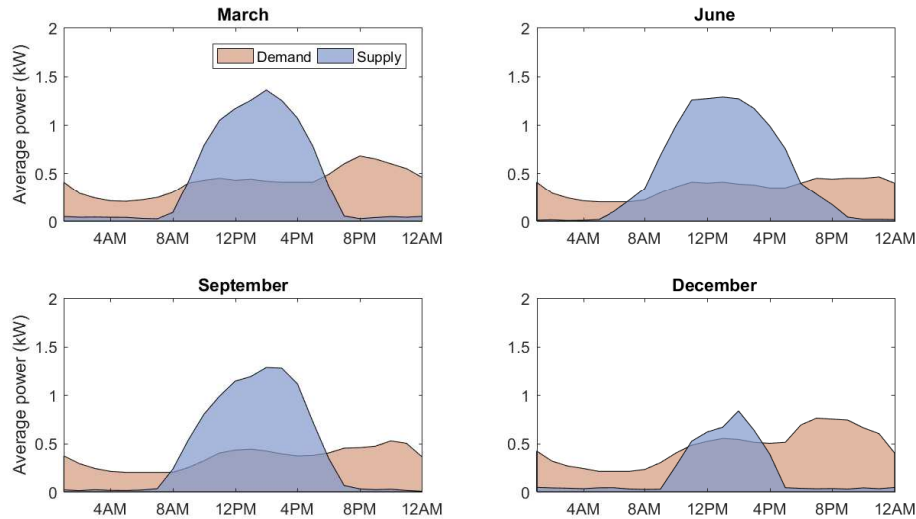


Figure 5.5: Daily production and consumption profiles for a system with 12 solar panels with 80° tilt and one urban wind turbine coupled onto a south-oriented noise barrier. Only 4 months displayed.

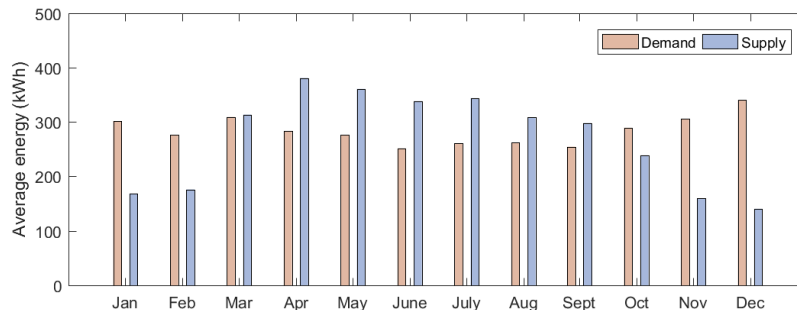


Figure 5.6: Aggregated production and consumption of each month. Annual generation is 3227 kWh with solar contributing 93.9% and wind 6.1% (i.e. 2992 kWh and 235 kWh respectively) and annual demand is 3400 kWh.

A number of energy management strategies have been reviewed, starting from stand-alone and moving towards grid-tied configurations. The three main criteria used to judge the adequacy of an energy management strategy are:

1. the generated energy is used sustainably, which implies that excess energy is limited;
2. the system is cost-efficient, meaning there is room for an economic return and;
3. no harm is done to consumer comfort, thus power quality and continuity of supply are guaranteed.

Stand-alone configuration. To balance the differences between generation and demand, a stand-alone configuration would require the use of dispatchable sources and/or distributed energy storage to reshape the energy profiles and assure stable electrical supply. On one side, at times of shortage, dispatchable sources used to support energy generation may be forced to run at unreasonably low loading due to the high variability of the non-dispatchable sources. On the other hand, a storage system sized to compensate for the daily

fluctuations of a dominantly solar generation will drive up the cost of the system considerably if minimization of waste energy is wanted. The need of a power quality solution to provide a response to disturbances equivalent to that of the existing electrical supply can also impact ownership cost substantially. Therefore, for a residential type of demand and the small-scale of the system, the concept of a stand-alone micro-grid fully supplied with non-dispatchable generation and without storage is unrealistic. Some of the challenges that islanded operation brings up could be avoided with grid connected operation. Another possible solution would be the addition of a battery and hydrogen storage subsystem.

Stand-alone configuration with battery and hydrogen storage. The coupling of hydrogen storage and batteries leads to greater flexibility as it allows short-term load-following through the batteries and long-term energy storage in the form of hydrogen [20]. Depending on the situation, surplus energy could be used either to charge the batteries or the hydrogen tanks. With the possibility of hydrogen storage, the management strategy can focus on maximizing the efficiency and lifetime of the batteries, adding value to the system [19]. However, if independence from the main grid is desired, the system must be dimensioned such that the peak power satisfies both the demand and the energy necessary for hydrogen production. Over-dimensioning combined with the additional components impact system cost significantly making this option suitable only for locations where stand-alone operation is a necessity or grid extensions are too expensive. Although this alternative is not economically viable today, the increasing interest from public and private authorities on research, development and deployment of hydrogen and fuel cell technologies are likely to turn this alternative into a very attractive solution in the near future. The so-called hydrogen economy holds other opportunities for the *Energy Wall* such as, for instance, a near-road charging station for hydrogen scooters. With the rapidly maturing hydrogen technology, this is an option to be investigated in future research.

Grid-supplying. Grid connection presents itself as the least costly alternative as it eliminates the imperative need of dispatchable energy sources. Because providing back-up short-term storage at zero marginal cost is unrealistic, storage could be considered for sites where security of supply is not guaranteed by the national electricity grid. Different from the previous strategies, this one meets the concerns of continuity of supply and minimized waste energy. With this in mind, this alternative arises as the only capable of balancing the energy profiles and still hold great promise of enabling the concept of an *Energy Wall* with an economic return.

5.3. Concluding remarks

The substantial disconnection between generation and consumption patterns associated with the *Energy Wall* near inhabited urban areas provides insights into the viability of the concept from both sustainable and economic perspectives. It can be argued, that the energy management strategies that ensure a sustainable and efficient energy use of a hybrid system of these characteristics are limited to grid-connected energy applications. Note that this claim is based in the current energy technology situation. The constant improvement in efficiency and storage solutions along with a reduction in costs is likely to open more opportunities in the future. These first conclusions regarding the possibilities and impossibilities of the system in current urban areas are used to shape the scope of the sensitivity analysis, the subject of the next chapter. Investigating the relationships between input model variables (orientation, wind resource and surface roughness) and output energy is interesting not only from the sustainable energy generation standpoint, but also for the economical assessment. Thus, a number of study cases are chosen to evaluate the influence of orientation on energy generation and assess the system output in a range of sites with different wind potentials and surface roughnesses.

6

Sensitivity Analysis

Having argued in the last chapter that grid-connection is the energy management strategy that enables the most efficient and sustainable use of the energy supplied by the *Energy Wall* nearby inhabited urban environment, the next step is to perform a sensitivity analysis on the output of the energy model. Due to grid-tied configuration, there is no imperative need to balance demand and supply. The system can, thus, be dimensioned for maximum production limited only by the size of one noise-barrier segment. The standard *Energy Wall* segment was defined in the previous chapter as the 6-meter long noise-barrier stretch fitted with one urban wind turbine and 12 solar panels on a 80° tilt. Leaving installed capacity constant, it is possible to produce energy output estimates of one standard segment in a set of predefined scenarios. The sensitivity analysis outlined in this chapter serves two main purposes,

- (A) investigate the *Energy Wall* supply in different circumstances and,
- (B) evaluate the stability of the model output to small changes in input parameters.

The latter is motivated by the fact that the parameter values and assumptions of any model are subject to change and error. Hence, the outcome of a model cannot be fully understood (Purpose A) without knowledge of the relationships between input and output variables (Purpose B). The sensitivity analysis will give information about,

- how the energy output of the models change with different orientations (Purpose A, sections 6.1 to 6.3);
- under what circumstances does the urban wind system operate at capacity factors low enough to question the overall worthiness of installing a wind turbine (Purpose A, section 6.1);
- how the energy output changes with more favorable wind conditions (Purpose A, section 6.2);
- how robust is the assumed vertical wind profile in the face of an increase in hub height and what is the increase in energy output (Purpose A and B, section 6.3);
- how robust is the urban boundary layer scaling technique¹ in the face of different surface roughness parameters (Purpose B, section 6.4);
- what is the impact of not considering zero-displacement height in logarithmic wind profiles within the urban boundary layer (Purpose B, section 6.4);
- how the future technological advances are likely to impact the wind energy contribution in the hybrid system (Purpose A, section 6.5);

Information about these sensitivities is extremely valuable, not only to assess the energetic potential of the system, but also to understand how robust is the model, and how reliable is the output. The wind energy model has higher uncertainty than the solar energy model, largely due to a greater number of input variables and assumptions. As a consequence, more in-depth consideration is given to wind in this analysis. Based on the parameter to be varied, the scenarios for which the model has been ran are presented in the following sections.

¹Refer to section 4.2.2 for explanation on the urban boundary layer scaling technique.

6.1. Varying noise-barrier orientation

The orientation of the noise-barrier affects both solar and wind energy generation. To study this effect, the arc domain has been split in intervals of 45° resulting in 8 different orientations. Because a North oriented noise-barrier is not different from a noise-barrier with a 0° azimuth (α), the term ‘alpha’ is used hereto as representative of road-side noise-barrier orientation. The concept of ‘energy rose’ is employed in this study as a tool to visualize the direction-dependent energy output of the model. The ‘local wind’ is the wind resource at the height of interest obtained following the urban boundary scaling technique presented in section 4.2.2. The kinetic energy in the local wind is transformed into useful energy by the turbine rotor. The complex aerodynamic phenomena governing the rotor-wind interaction determines the fraction of power in the wind that is extracted by the rotor. In this analysis, the power in the wind (P_{in}) is expressed by Equation 6.1, where A is the rotor area, and ρ is the density of air. The extracted power (P_{out}) is calculated by means of the experimental power curve presented in section 4.2.5 earlier. The difference between both is the end result of aerodynamic, mechanical and electrical efficiencies and is commonly referred to as power coefficient (C_p). This idea is captured in Figure 6.1, providing a measure of the overall efficiency of the studied wind turbine system. Note that production of P_{in} and P_{out} over one year period yields the annual energy indicated by E_{in} and E_{out} . The theoretical maximum efficiency a turbine can achieve is given by Betz Limit at $C_p=0.593$ although in real operation conditions, wind turbines operate well below this threshold. Based on the experimental power curve, the C_p of the chosen turbine is 0.331 at rated power wind speed (9 m/s), which means; a little over 33% of the kinetic energy in the wind can be captured by the rotor at that particular wind speed.

$$P_{in} = \frac{1}{2} \cdot \rho \cdot A \cdot u^3 \quad (6.1)$$

$$C_p = P_{in}/P_{out} \quad (6.2)$$



Figure 6.1: Energy rose showing in red the energy available in the local wind (E_{in}) and in blue the energy produced by the wind turbine (E_{out}). Radial axis in kilowatt-hour (kWh), time frame of one year.

Another convenient parameter used to evaluate the performance of a wind turbine is the capacity factor (CF). This factor is the ratio between the actual energy yield to the amount of energy that would have been produced had the turbine been operating continuously at rated power during the same period. The CF measure is useful as it gives a sense of the real full load hours of an operating wind turbine. While commercial scale wind farms may report capacity factors as high as 30%, those differ greatly from the CF of small urban wind turbines. This is largely due to the less ideal wind conditions and the significantly smaller rotor size. A computational fluid dynamics (CFD) study of a small turbine in the urban landscape of west London produced capacity factors of 4% [22]. Also in the UK, a field study investigating the performance of several small-scale turbines resulted in capacity factors in the 1.6% to 13.6% range with a 6.4% average [31]. Those values are consequently taken as a valid reference for this study.

The solid lines of Figure 6.2 show the turbine’s output power incorporating the wind concentrator effect of the noise-barrier as a function of orientation alpha. Values in brackets indicate the annual energy yield. To establish comparability, E_{out} from Figure 6.1 is indicated with a dotted line. By comparing these two lines, the impact of the wind concentrator effect can be appreciated. The noise-barrier oriented to alpha-180, for example, shows an energy yield curve lengthened towards South, as this is the direction of perpendicular

flow². Due to the assumption of a symmetrical noise-barrier, the energy rises with alpha-0 to alpha-135 are identical to those with alpha-180 to alpha-315, as expected. Maximum annual energy yield is obtained with a northeast (or southwest) segment orientation. This result is consistent with the prevailing wind direction of the local wind resource presented earlier in Figure 3.5. The higher frequency and wind force of such winds maximize the wind concentrator effect of the noise-barrier leading to higher wind speeds at rotor height. On the contrary, a northwest- (or southeast-) oriented segment will generate almost 10% less energy at the end of the year. The resulting capacity factors are in the 3.6% to 4% range, agreeing with those found in literature.

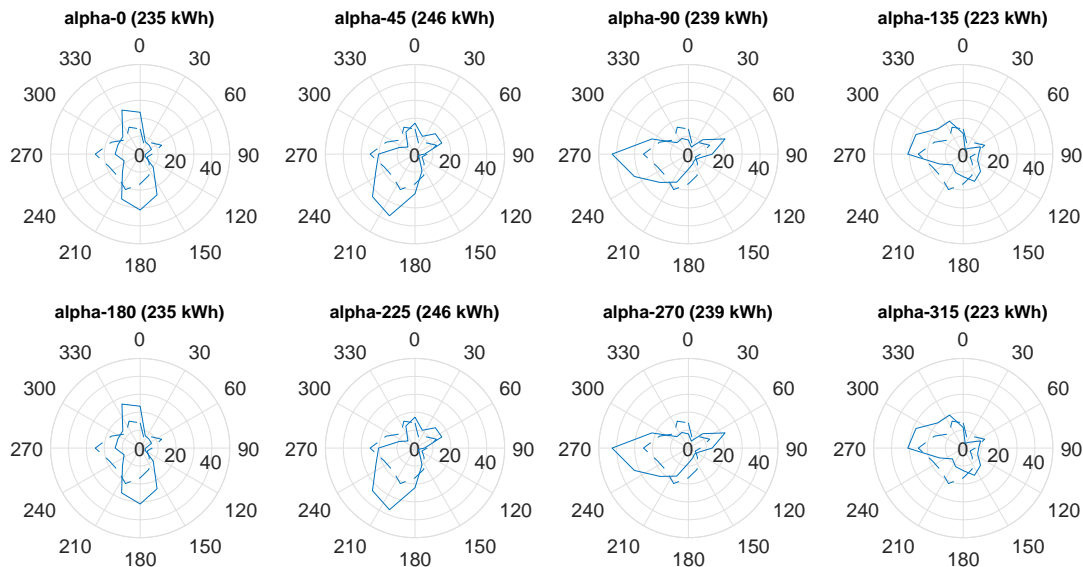


Figure 6.2: Power produced by the turbine including the concentrator effect of the noise-barrier (solid line) and without the effect (dotted line) for eight orientations; annual energy yields are between brackets; radial axis in kWh.

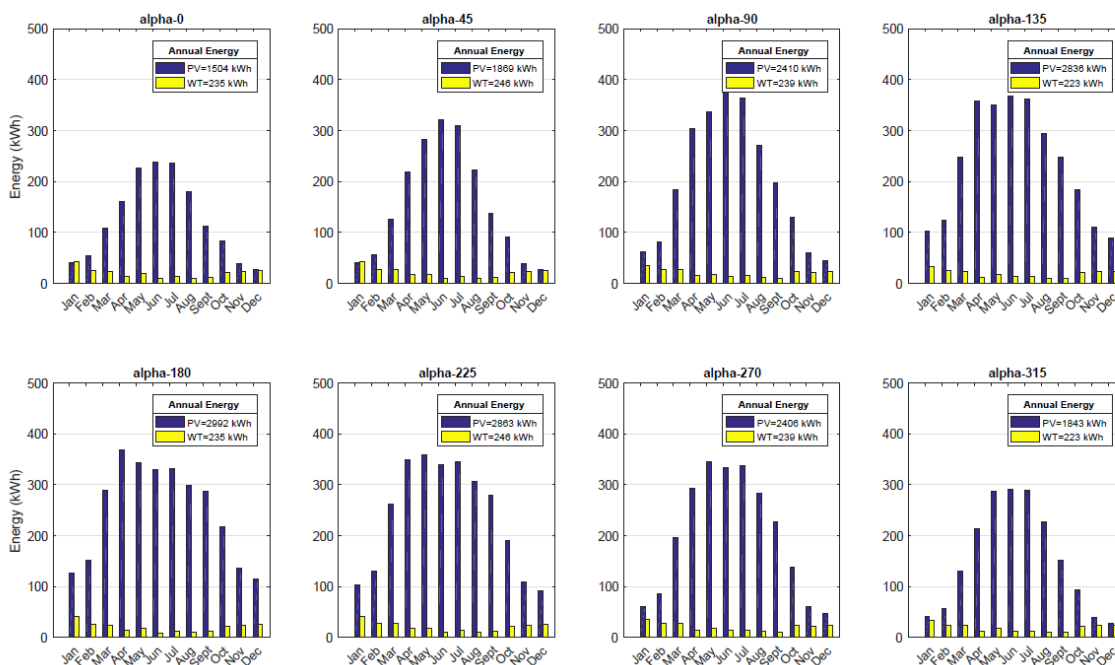


Figure 6.3: Monthly distribution of solar and wind energy generation levels for eight noise-barrier orientations. Annual yields appear separately in the box.

²Maximum wind concentrator effect occurs when flow is perpendicular to the noise-barrier long-axis (see section 3.2).

Shifting the focus to solar power, the orientation-related loss of solar output is substantially larger. The difference between maximum and minimum annual yield is almost 50%. Figure 6.3 shows the distribution of combined solar and wind energy output throughout the year. Skewed by the higher contribution of energy generated from the sun, the hybrid system achieves maximum annual production of almost 3230 kWh with a South orientation and a minimum production of 1740 kWh when oriented southeast. In fact, solar energy delivers between 86% and 93% of the total hybrid output, depending on orientation α . This results quantify the dependency of the *Energy Wall*'s output on orientation and confirms the dominance of solar energy when it comes to positioning a segment for optimum hybrid system performance.

6.2. Varying wind resources

All values presented so far were based on one unique wind data set, the base case wind resource introduced in section 3.1.1. In the real world, prospect noise barrier sites, even if just few kilometers away, can present significantly different wind characteristics. Across areas where irradiation patterns are fairly constant, the airflow patterns can vary in speed and direction, particularly within the urban boundary layer. Therefore, calculating the annual energy output using different wind data sets holds great value for selection of prospect *Energy Wall* sites. After investigation of the wind resources above The Netherlands, data from three KNMI [1] meteorological stations have been selected using the following criteria. First, only meteorological stations measuring hourly wind speed and direction for a minimum period of one year were considered. Second, to allow comparability between the new wind data sets and the base-case data set, stations sampling at a height different from 10 m and over a non-smooth surface were screened out. Lastly, out of the remaining stations, those with mean wind speeds above the base-case wind resource have been studied in more detail before selecting three with suitably spaced out means. Table 6.1 introduces the selected wind resources for which the model is ran. Each resource gets its name from the city where the data-provider meteorological station is installed: Rotterdam (RTDM), Valkenburg (VLKB) and Stavoren (STRN). The base-case wind resource preserves its original name (Delft). It is useful at this point to define a new parameter, the **urban penalty factor**. This refers to the factor by which the mean wind speed is reduced after scaling the wind speed from reference to hub height and is representative of the combined effect of the vertical profile and the local surface roughness on the wind.

To allow an insightful interpretation of the results, a more detailed characterization of the selected wind resources can be found in Figures 6.4 and 6.5. Although, each wind resource has a particular speed and direction distribution, the prevailing wind direction is clearly southwest, a natural attribute of the geographical situation of The Netherlands. This is remarkably the case for speeds above 4 m/s, whilst lower wind speeds have a more even distribution. Accordingly, the energy roses are strongly southwest-dominated, because only winds strong enough to set the turbine in motion can be used for energy generation. Because the input wind data vary not only in speed, but also in direction, comparison between wind resources will provide information on speed-energy and direction-energy relations.

	Delft	ROTDM	VLKB	STRN
Mean wind speed (m/s):				
measured at reference height (10 m)	3.84	4.21	5.08	5.52
scaled at hub height (8 m)	2.99	3.33	4.01	4.35
Urban penalty factor	-0.22	-0.21	-0.21	-0.21
Yearly energy (kWh):				
available in the wind (E_{in})	813.6	973.6	1819.1	1883.1
extractable by the turbine (E_{out})	216.4	264.7	488.6	526.1

Table 6.1: Characteristics of the selected wind resources

Knowledge of how the energy output changes with more favorable wind conditions gives information about the possibilities and impossibilities of the *Energy Wall* as it helps identifying a threshold below which the installation of this hybrid system might not be desirable. Specific terminology is used in this analysis to interpret the results. The term **performance ratio** is used to quantify the wind concentrator effect of the noise-barrier and is the ratio between the energy generated by the *Energy Wall* wind system and the energy a similar wind turbine can generate from the local wind in the absence of a noise-barrier. Likewise, the mean speed of the local wind resource increases (or decreases) after the acceleration (or deceleration) correction

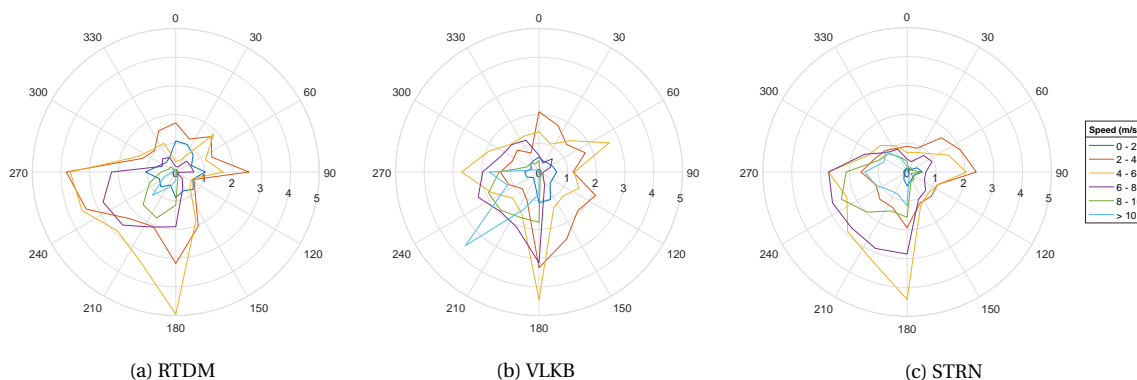


Figure 6.4: Wind roses at reference height with radial axis given as time frequency (%) in a year.

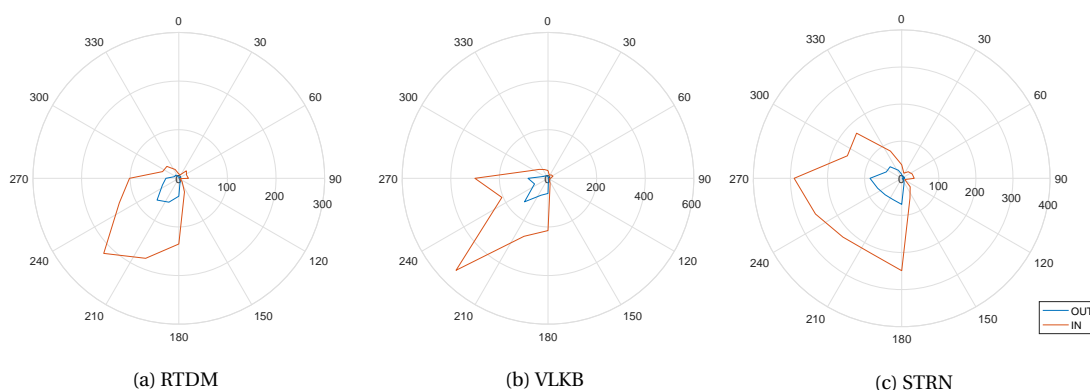


Figure 6.5: Energy roses showing in red the energy available in the local wind (E_{in}) and in blue the energy produced by the wind turbine (E_{out}); annual energy yields provided in Table 6.1; radial axis in kilowatt-hour (kWh), time frame of one year.

factor³ is taken into account. The resultant mean speed is referred to as **corrected mean** to distinguish it from the local wind mean speed. Lastly, the **state-of-turbine** is related to the starting behavior study presented in section 4.2.4. The three values give information about the fraction of hours in a year the turbine is standing still (state zero), rotating without generating (state one) or rotating and generating (state two). The discussed parameters are summarized in Table 6.2 for each evaluated wind resource starting from Delft, the base case, and moving to more favorable wind conditions. Figure 6.6 shows the energy yield at each wind speed for each investigated wind resource. The total area of the bars represents the annual energy yield and is related to the percentage of time the turbine is in 'state two' (blue colored pie slices). A number of inferences can be drawn from these results.

1. First, as expected, the impact of orientation on energy output depends on the degree in which a particular wind direction prevails over the others. This impact is direct consequence of the wind concentrator effect and can be strong enough to increase or decrease annual energy yield by 36% as is the case for ROTM. This information is given by the performance ratios of Table 6.2.
2. Second, wind resources at the lower end of the speed range show discouraging state-of-turbine values. As seen in the pie charts of Figure 6.6, rotors are sitting still almost 30% of the year, and generating periods add up to less than half of the year. These values impose major economic burdens to the system as they increase energy payback times considerably.
3. Third, during one quarter of its operation time, the turbine is generating only wear and tear, indistinctly of wind resource. In point of fact, state-of-turbine results for ROTM, VLKB and STRN show consistently 'state one' percentages around 25%. During these periods of no generation, the turbine is still rotating. Although the components are subject to minimal stress due to low wind speeds, mechanical wear is expected and may be seen as a kind of inefficiency.

³Refer to section 4.2.3 for clarification on correction factors.

4. Fourth, a distinction can be made amongst the investigated wind resources; the two resources at the higher end of the speed range show 'state two' percentages consistently above 50% which in terms of energy means breaking 400 kWh per year and capacity factors over 6.4%.
5. Fifth, moving from wind resources with hub-height mean speed of 3 m/s to a mean speed of 4 m/s entails doubling annual energy yield and again, breaking the 400 kWh barrier.

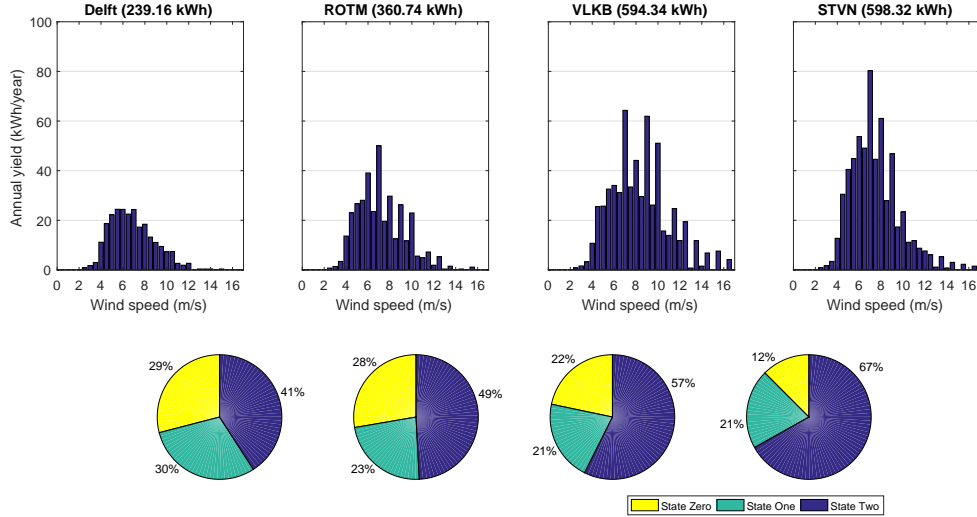


Figure 6.6: Energy generation at each wind speed for the investigated wind resources (top) and corresponding state-of-turbine percentages (bottom); annual energy yields are indicated in brackets (kWh); results from southwest noise-barrier orientation only.

Orientation (alpha)		N	NE	E	SE	S	SW	W	NW
Delft									
Annual Energy	kWh	235.09	246.3	239.16	222.6	235.09	246.3	239.16	222.6
Performance Ratio	%	109	114	110	103	109	114	110	103
Corrected Mean	m/s	3.06	3.12	3.11	3.04	3.06	3.12	3.11	3.04
State of Turbine	%	29-31-40	29-30-41	30-29-41	29-31-40	29-31-40	29-30-41	30-29-41	29-31-40
ROTM									
Annual Energy	kWh	277.88	360.74	307.6	220.04	277.88	360.74	307.6	220.04
Performance Ratio	%	105	136	116	83	105	136	116	83
Corrected Mean	m/s	3.37	3.62	3.5	3.24	3.37	3.62	3.5	3.24
State of Turbine	%	28-24-48	28-23-50	28-24-48	28-27-45	28-24-48	28-23-50	28-24-48	28-27-45
VLKB									
Annual Energy	kWh	496.71	594.34	535.07	425.4	496.71	594.34	535.07	425.4
Performance Ratio	%	102	122	109	87	102	122	109	87
Corrected Mean	m/s	4.08	4.33	4.17	3.92	4.08	4.33	4.17	3.92
State of Turbine	%	18-24-58	22-21-57	20-23-57	19-25-56	18-24-58	22-21-57	20-23-57	19-25-56
STRN									
Annual Energy	kWh	536.38	598.32	586.31	521.02	536.38	598.32	586.31	521.02
Performance Ratio	%	102	114	111	99	102	114	111	99
Corrected Mean	m/s	4.4	4.58	4.55	4.37	4.4	4.58	4.55	4.37
State of Turbine	%	10-24-65	12-21-67	12-22-66	10-25-65	10-24-65	12-21-67	12-22-66	10-25-65

Table 6.2: Sensitivity analysis results of varying noise-barrier orientation (α) and varying wind resource.

6.3. Varying hub height

The response of the model output in face of a change in hub height is interesting for two main reasons. First, to test the robustness of the boundary layer scaling technique used to scale the reference wind to the height of interest; and secondly, to weigh the gain in annual energy production against the cost entailed in bringing the rotor higher in the air. An increase in hub height can be the result of either a higher noise-barrier or

a longer turbine tower. Considering that a noise-barrier higher than 7 m is uncommon and that a tower longer than 4 m would inhibit the wind concentrator effect of a noise-barrier, it is considered that a 10 m hub height reflects a realistic scenario. Leaving all other variables at base values, the recalculated urban penalty factors are, as expected, less negative for a 10-meter hub if compared with the 8-meter base case. These new penalties are within the -0.14 to -0.15 range. To understand the impact of these lower penalties, model runs with the modified hub height have been conducted for all orientations and wind resources. Results have been normalized to those obtained with the original hub height (Delft, Table 6.2) and are reported in Table 6.3.

Orientation (alpha)	N	NE	E	SE	S	SW	W	NW
Delft								
Annual Energy	1.28	1.29	1.29	1.31	1.28	1.29	1.29	1.31
Corrected Mean	1.09	1.09	1.09	1.09	1.09	1.09	1.09	1.09
RTDM								
Annual Energy	1.29	1.25	1.28	1.32	1.29	1.25	1.28	1.32
Corrected Mean	1.09	1.09	1.08	1.08	1.09	1.09	1.08	1.08
VLKB								
Annual Energy	1.23	1.18	1.19	1.25	1.23	1.18	1.19	1.25
Corrected Mean	1.09	1.09	1.09	1.09	1.09	1.09	1.09	1.09
STRN								
Annual Energy	1.23	1.23	1.23	1.23	1.23	1.23	1.23	1.23
Corrected Mean	1.09	1.09	1.09	1.09	1.09	1.09	1.09	1.09

Table 6.3: Energy yield and mean wind speed for a higher hub height of 10 m normalized to the energy yield and mean wind speed of the base case hub height of 8 m reported in Table 6.3.

The normalized mean speeds show that a rotor sitting 2 m taller will experience wind speeds 9% higher on average, independently of wind resource quality and noise-barrier orientation. The increase in annual energy yield is higher, which could have been expected because the power produced is proportional to the cube of the wind speed, and is also more sensible to orientation fluctuating between 20% and 30%. The obtained values suggest that more favorable wind resources do not necessarily experience a bigger gain in energy yield, rather the opposite. One possible explanation could lie in the shape of the power curve. The slope of the curve increases remarkably between 2 to 4 m/s and 4 to 6 m/s and not so much between 4 to 6 m/s and 6 to 8 m/s. Therefore, wind speeds stepping from the 2-4 m/s range to the 4-6 m/s range will produce a energy output gain proportionately bigger than wind speeds stepping from 4-6 m/s to 6-8 m/s. In synthesis, within low speed wind regimes, the expected gain of raising the hub of a wind turbine does not increase linearly with more favorable wind conditions. This conclusion should be taken into consideration when the costs associated with taller wind turbines are discussed during the project planning phase.

6.4. Varying surface roughness

The uncertainty associated with surface roughness parameters has been thoroughly discussed in section 3.3. It is thus important to evaluate the sensitivity of the energy output to changes in roughness values. First, the influence of the inclusion of zero-displacement (d_0) in the classic logarithmic profile is tested. Many published works disagree on the way this parameter should be calculated [22][34][35][51], others simply overlook their inclusion avoiding in this way the problematic of parameterizing surface roughness characteristics [20][52]. Information from this first run is important to gauge the influence of a modeling choice that is not shared among all urban wind energy modelers. The purpose of the second run is to evaluate how sensitive the output energy is to changes in z_0 and d_0 . If the output is robust (insensitive to such changes) this allows more confidence in the results than if the output is highly sensitive; mainly because insensitivity introduces more flexibility in the calculations of z_0 and d_0 estimates.

Non-inclusion of zero-displacement. Similar to the urban penalty found in the previous section, the recalculated urban penalty factors taking $d_0 = 0$ lead to less negative penalties also in this case, around -0.14 for all wind resources. This result suggests that failing to include d_0 in urban wind logarithmic profiles is comparable to scaling wind speeds with a vertical overshoot of 2 m. This finding, although strongly dependent on the modeling strategy used in this paper, is consistent with the sensitivity analysis presented in [10], where the authors cautioned modelers to not overlook the importance of d_0 in wind profile analysis. The normalized results are similar to those in Table 6.3 and are plotted in Figure 6.7.

Modified surface roughness characteristics. Based on the surface roughness parameters derived in section 3.3, two new sets of z_0 and d_0 estimates have been generated. To keep the sets direction-sensitive, a 0.9 factor has been applied to all direction sectors so that the impact of underestimating surface roughness by 10% can be investigated. This scenario is the equivalent of smoothing out surface roughnesses, and consequently decreasing the urban penalty. The same has been done with a 1.1 factor to evaluate the opposite scenario. On average, z_0 values are altered by ± 0.02 and d_0 values are altered by ± 0.23 . In some sectors, z_0 values can vary up to ± 0.08 and d_0 values up to ± 0.31 , while in other sectors the variation is as small as ± 0.01 and ± 0.17 , respectively. The recalculated urban penalty factor is -20% in the smoother scenario and -24% in the rougher. Normalized annual energy output and wind speed results have been included in Figure 6.7.

Varying hub height and surface roughness characteristics provides information about the performance of the urban boundary scaling technique. Results from the four scenarios can be contrasted in Figure 6.7 using the following nomenclature to distinguish between cases; 'HH' stands for varying hub height, 'ZD' for neglecting zero-displacement height, and 'MR⁻' together with 'MR⁺' represent the two model runs with modified surface roughness. Because the results are consistent across all orientations, only North (alpha-0) is displayed. Values have been normalized once again to those obtained with base values (Table 6.2).

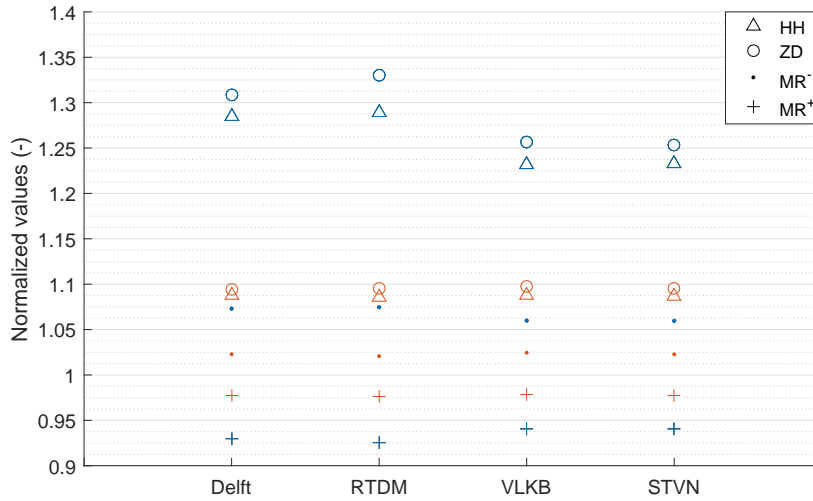


Figure 6.7: Sensitivity of annual energy output (blue) and corrected mean speed (orange) to varying hub height and surface characteristics for 4 different wind resources. Results are normalized to the base-case of Delft. Legend describes different sensitivity scenarios: varying hub height (HH), neglecting zero-displacement height (ZD), under- and over-estimating surface roughness parameters (MR⁻ and MR⁺)

Results for 'MR⁻' and 'MR⁺' consistently show that a 10% inaccuracy in z_0 and d_0 values will overestimate or underestimate annual energy yield by 8%. This means that determination of surface roughness parameters should be well-investigated and simple approximations will impact the reliability of a model significantly. As stated before, there is a remarkable similarity between the values obtained from 'HH' and 'ZD'. Both scenarios show an increase in annual energy yield in the range of 20% and 30% but there are some differences among wind resources. The two with higher mean speeds, VLKB and STVN, experience a smaller energy gain than the other two, whilst the increase in corrected mean speed holds nearly steady at 9%. It is worth reiterating that this finding is consistent among all orientations and thus, independent of wind direction. This small discrepancy is yet another evidence of the complexities inherent in wind energy generation within low, highly variable wind regimes suggesting that; for a given increase in hub-height wind speed, the subsequent gain in energy yield will depend on the percentage of time that winds blow with a particular wind speed. In other words, the (energy) consequences of an increase in wind speed vary depending on which speed level does this increase affect the most. The power curve associates a certain power output to each speed level and, therefore, has necessarily a role in this play. This observation emphasizes the importance of investigating the suitability of a wind turbine technology and its particular power curve, to the wind conditions at the prospect installation site.

6.5. Varying power curve

Technological advances in small wind turbines for urban applications will result in improved power curves. The performance of these turbines at low wind speeds is the most important parameter, hence current research is mainly directed towards lowering cut-in speeds and bringing power coefficients closer to the Betz limit. To investigate how future technological advances can increase the contribution of wind power in the hybrid system, a model run with a different power curve is conducted. Figure 6.8 displays both power curves, the experimental power curve used in the base-case scenario, and the improved power curve result of the current dynamic technological situation and the expected future trends. The power specifications of the *Archimedes Windmill* developed by KETech® have inspired the improved power curve. This small wind turbine has an innovative design ensuring that wind is drawn into the turbine. In theory, this design allows higher power coefficients and better performance at low wind speeds. The turbine has similar size than the base case turbine, which enables noise-barrier integration.

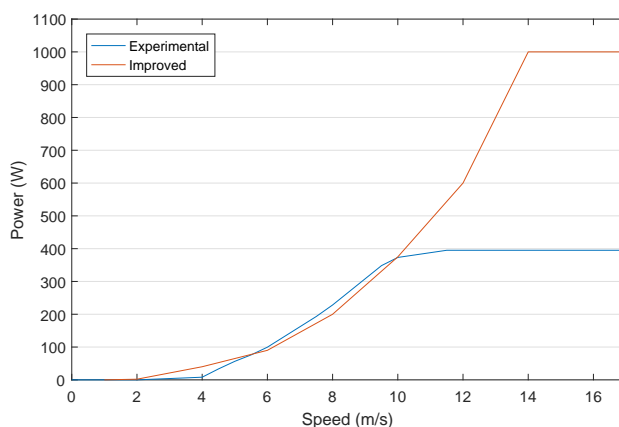


Figure 6.8: Base case power curve derived experimentally and improved power curve inspired in KETech's *Archimedes*

The starting behavior of the turbine has been upgraded to go hand in hand with the predicted technological developments. Wind tunnel tests were not available in this case, thus, the new speed levels triggering state transitions have been estimated based on intuition. The selected values are 2 m/s and 1 m/s for $start_{sp}$ and $stop_{sp}$, and 2.5 m/s and 1.5 m/s for cut_{insp} and $idle_{sp}$. In the next page, Figure 6.9 illustrates the consequences of improving wind turbine performance at low wind speeds by comparing state-of-turbine statistics from the base-case to those obtained from the future prospect case. The proportion of time the turbine operates in 'state two' becomes considerably larger having a direct impact on energy yield. This increase comes with a remarkable reduction in 'state one' and, although it may not have a direct consequence in terms of energy, this reduction indicates that it is possible to make a better use of the technology and limit worthless wear and tear.

Figure 6.10 (next page) summarizes the results of all the investigated scenarios as a function of noise-barrier orientation, only for the local wind resources of Delft. The prospect technological advances result in a 30% mean increase in annual energy yield, which corresponds to capacity factors of 5%. This energy gain is comparable in magnitude to that of scenarios 'HH' and 'ZD' but, distinct from those scenarios, the gain here is not motivated by changes in wind speed. Normalized corrected mean speed values remain constant at 1. In fact, out of the investigated scenarios, this is the only one not affecting wind speed. Therefore, results from this last scenario may be representative of the estimated potential of a prospect *Energy Wall* installed in the study area with state-of-the-art technology making use of the local wind resources.

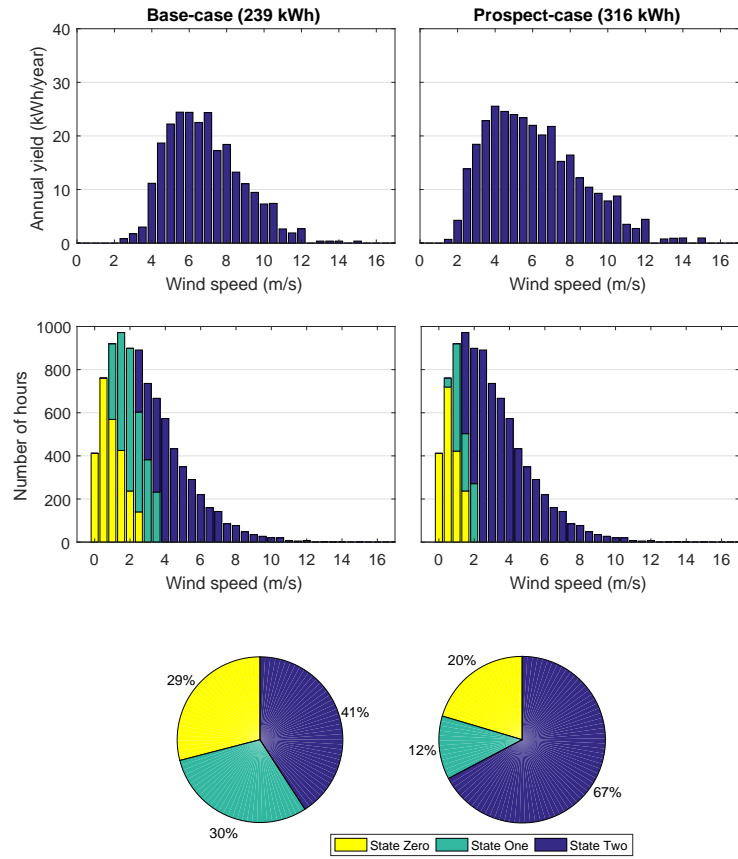


Figure 6.9: Energy generation at each wind speed (top), distribution of time spent in each turbine state as a function of wind speed (middle) and corresponding state-of-turbine percentages (bottom); annual energy yields are indicated in brackets (kWh); results from Delft wind resource and southwest noise-barrier orientation.

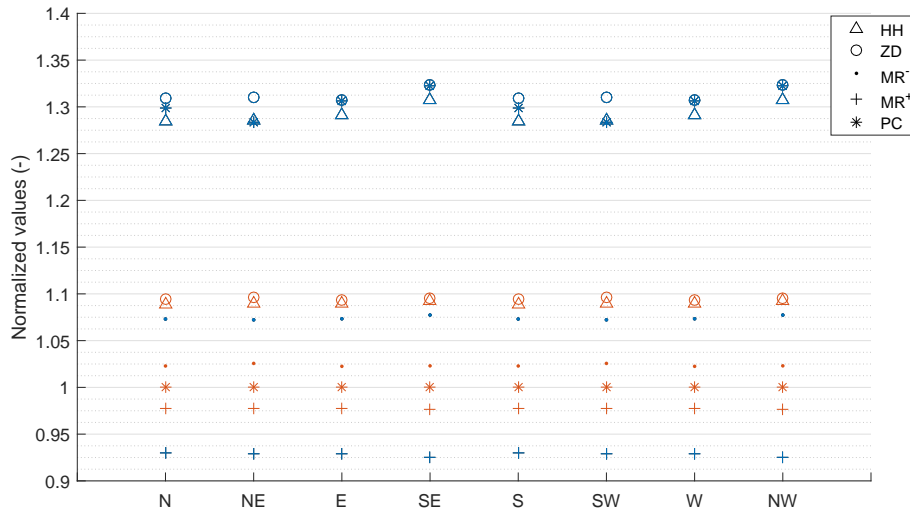


Figure 6.10: Sensitivity results for Delft wind resource at all noise-barrier orientations. Displayed parameters are normalized annual energy output (blue) and corrected mean speed (orange). Legend describes different sensitivity scenarios: varying hub height (HH), neglecting zero-displacement height (ZD), under- and over- estimating surface roughness parameters (MR⁻ and MR⁺).

6.6. Significance of sensitivities

This section gathers the relevant findings of the presented analysis and reflects on the two purposes stated at the beginning of the chapter. In order to provide continuity, the section has been structured to follow the same order of the analysis. In view of the high complexity associated with the availability and performance of urban renewable energy generation, results from this analysis are significant not only to assess the potential of the *Energy Wall* but also to identify gaps and uncertainties in scientific knowledge and point out major research needs. The aim has been to transform the obtained results into useful information applicable for providing guidance to urban planners, technology developers and researchers. Information can be transformed into recommendations and ultimately provide a significant level of support to decision-making, which can further enhance a constructive interaction across different levels of governance and unleash deployment of urban-integrated renewable energy systems. A rule guiding this section has been the effort to be faithful to the obtained results while trying to stay within the region of model validity.

Relative to purpose A, the *Energy Wall* supply was investigated for eight noise-barrier orientations, four different wind resources, two different wind turbine hub heights, and two different wind turbine power curves.

- Comparing the energy output of the hybrid model across different orientations confirmed that the contribution of solar energy is more sensitive to changes in orientations than wind energy. This dependency should be taken into consideration during planning and construction phases of a prospect *Energy Wall*. Shifting the focus to wind energy production, model runs for varying orientation revealed information about the wind concentrator effect of the noise-barrier. However, this feature was further explored with the inclusion of different wind resources.
- Results from varying wind resource revealed that, the wind concentrator effect is strongly correlated to the percentage of time winds blow with a particular wind direction and the relative angle between this direction and the orientation of the noise-barrier. Interestingly, this acceleration/deceleration effect seems independent of wind speed. Evaluation of state-of-turbine percentages within different wind regimes suggested that a threshold may exist above which wind turbines can operate at capacity factors greater than 6.4% and actually produce electricity (not only spin) for over 50% of the hours in a year. This qualitative jump is noticeable in wind resources with hub-height mean speed above 4 m/s. This threshold should be considered when potential sites for the installation of *Energy Wall* are surveyed.
- Increasing the height of the wind turbine rotor by 2 m showed (under the assumption that the vertical speed profile of urban wind follows a logarithmic increase) a mean wind speed increase of 9% and a mean annual energy yield increase between 20% and 30%. The latter was more sensitive to wind resource and noise-barrier orientation. In fact, results suggested that the slope of the power curve plays role in determining how a specific jump in wind speed will be translated into the subsequent gain in energy yield. It was found that this relation may not be as linear as could have been expected. This should caution project planners to study the expected gain in energy yield before incurring the costs of a taller turbine. Moreover, it should encourage evaluation of different turbine models to determine which power curve leads to greater annual yields in a particular site.
- Model runs for the two power curves led to the conclusion that optimizing wind turbine performance at low speeds holds great promise for the future of this innovative concept. Lowering cut-in levels from 4 m/s to 2.5 m/s can increase annual energy yields by 30% on top of the benefits arising from a reduction of time the turbine operates in survival mode, that being generating only wear and tear. In view of this, future urban-wind technological advances should focus on improving the starting behavior of a turbine by designing turbines with lower cut-in speeds.

In regard to purpose B, the sensibility and stability of the developed small wind energy model was evaluated by means of changing the three input parameters of the boundary layer scaling technique, which are: wind turbine hub height (z_H), direction-dependent surface roughness length (z_i), and direction-dependent zero-displacement height (d_i).

- The importance of accurately estimating d_i in urban logarithmic wind profiles is often overlooked. Based on the surface roughness map used in this model and according to the results, the practice of neglecting this parameter is equivalent to scaling wind speeds with a vertical overshoot of 2 m. Which

in wind terms means overestimating mean hub-height speed by 9% and, in energy terms means overestimating annual yields by 20% and 30%. Interestingly, annual yield results revealed higher sensitivity to wind resources. This finding supports the idea that for a given increase in wind speed, the resulting energy gain will depend on the percentage of time that winds blow with a particular wind speed.

- Given the lack of a well-received expression for the calculation of z_i and d_i , the task of identifying a range for each parameter which realistically reflects its possible range was based on the understanding of the theoretical relationship between them and the assumption that they are positively correlated. The results revealed that a 10% change in z_i and d_i generate a subsequent 8% change in annual energy yield. This is yet another evidence of the complexities inherent in wind energy generation within low, highly variable wind regimes revealing the insufficient experience and the lacks that theoretical knowledge cannot address due to the inhomogeneity of the system.

7

Technoeconomical Assessment

Renewable energy projects are much more capital intensive than their conventional counterparts. After an investment has been incurred, the means to react to changing economic circumstances are limited. Therefore, capital cost is a central element in every project decision [36]. With this in mind, the economic viability of the *Energy Wall* is studied in this chapter. Evaluation of integrated urban renewable energy projects at their initial feasibility stage has limits to the level of economic detail that can be examined. Some additional costs, as well as capital saving opportunities, only become apparent as the project progresses. Accurate costing requires a detailed study to identify and quantify sources of expenditure and develop a cost allocation scheme. Although subject to uncertainty, the preliminary economic analysis presented in this chapter can provide useful guidelines and aid in decision-making processes. The economics of wind and solar are first analysed separately to establish comparability. Then, the hybrid system is jointly analysed and further cost reductions are put into perspective by considering the additional savings that hybridization can bring. The results are put together in the last section.

7.1. The price of energy

System expenditures are split in two main categories, namely capital expenses (CAPEX) and operation expenses (OPEX). Based on the energy output obtained from the model, a price measure is commonly derived using the concept of levelized cost of energy (LCOE). This measure represents the per-kilowatt-hour cost (in discounted real amount) of building and operating a generation system over its life span. For technologies such as solar and wind, with relatively low operating costs, the estimated CAPEX is the major contributor to the LCOE compared to other conventional technologies which have to account for fuel costs and more demanding maintenance. Capital costs vary regionally and across time as technology improves. This uncertainty is the main limitation of the LCOE but there are other factors that this measure fails to capture such as the existing resource mix of the region, the security of supply and the emissions associated with each generation type [3]. In this sense, comparison between LCOE values from dispatchable and non-dispatchable sources may lead to distorted conclusions and is important to keep the big picture in mind.

An important factor in the calculation of LCOE is that all cash flows are assumed at their nominal or real levels. A common practice is to make cost predictions in the long term using real values. From this point onwards, all costs stated in this analysis are expressed in their real values [12]. Another influential factor in the calculation of LCOE is the choice of discount rate. In many published studies, this factor is assumed without further investigation, other studies apply identical discount rates to all technologies and locations. These practices can result in misleading conclusions. For instance, large wind farms requiring a large and risky investment will discount at high rates (i.e. 10%) as they must survive as a business [31]. Given the barriers facing small wind turbines for urban applications, it is unrealistic to apply such a high rate as it will never result in a profitable investment. It is important to keep in mind that the interest rate at which a particular investment is discounted has an underlying effect on its economics. To predict the discount rate of a particular technology, amount of investment and project-specific risk are often useful. However, uncertainty still remains high because financing conditions are location-dependent and can be subject to governmental control [31]. Based on the small size of the system and the relatively short market history of

urban energy technologies, a discount rate of 3% is applied in this study and is considered a conservative choice. The fact that LCOE is strongly dependent on discount rate compromises the validity and fairness of comparing LCOE levels among different projects. The LCOE notion is thus not suitable for determining the cost efficiency of a specific energy generation against the actual spot value of electricity [12]. In this analysis, the concept of LCOE is used to measure the weighted average costs of different system configurations. The same methodology is employed in all LCOE calculations ensuring a consistent treatment among them. This enables fair comparison between the different types of system configurations.

7.1.1. Calculating the LCOE

A variety of methods can be found in literature for the calculation of LCOE. The one employed in this analysis is based on the present value method used in [12] and [25]. This approach takes all expenditures and earnings streams incurred during the lifetime of a project and discounts them to a common base year. The ratio between the cash values of all expenditures and the cash values of power generation is the price at which a kilowatt-hour should be sold in order to break even. This break-even price is, by definition, the average levelized cost of energy. Discounting generated energy may seem irrational from a physical standpoint, but is the result of accounting transformations [12]. The amount of energy generated is implicitly linked to the earnings received from its sale. This exercise of abstraction has the goal to account for the time value of money; the farther this energy earnings are displaced in the future, the lower their cash value. All LCOE calculations in this analysis are presented in 2018-Euros and a project lifetime of 20 years is assumed. Expressed mathematically, the LCOE is equivalent to,

$$LCOE = \frac{I_0 + \frac{RC_{t^*}}{(1+i)^{t^*}} + \sum_{t=1}^n \frac{O\&M_t}{(1+i)^t}}{\sum_{t=1}^n \frac{E_t}{(1+i)^t}} \quad (7.1)$$

I_0 = investment expenditure in net present value

RC_{t^*} = replacement cost incurred in year t^*

$O\&M_t$ = operation and maintenance costs incurred in year t

E_t = energy generated in year t in kWh

i = real interest rate or discounting factor in %

n = financial life of the project

The share of external financing and equity financing is not taken into account at this point. The amount of equity capital, the return on equity capital over the lifetime, the cost of debt and the share of debt are project- and location-specific factors that could be included explicitly in the analysis through the weighted average cost of capital (WACC) over the discounting factor [12]. The present analysis, however, does not make such inclusion as it would limit the applicability of the results to a specific financial scenario. A scenario that is, anyway, not certain. It is for the same reason that the supportive schemes and incentives are excluded from the analysis. While a more detailed analysis could give the impression of more realistic results, it would also bring significantly higher granularity of assumptions and potentially reduce the transparency of the calculations. The simpler approach is favored as it has the additional advantage of making the analysis transparent.

To account for the fact that energy generation units degrade over time, a degradation factor is included separately for wind and solar production. On the solar side, results of analyzing nearly 2000 degradation rates measured on single solar modules or entire systems were reported in [32] showing on average, a 0.5% decline in energy yield per year. In particular for monocrystalline silicon technology, the median degradation rate per year was found to be 0.36%, which is the value assumed in this analysis. Many small wind turbine manufacturers claim nearly no degradation during the lifetime of their products. No relevant literature was found to sustain or deny such claim. Therefore, based on the premise that engineering machines degrade and the fact that wear and tear is not limited to periods of energy generation¹, a conservative degradation rate per year of 0.5% is assumed.

It is appropriate at this point reiterate that the purpose of this thesis project is to assess the sensitivity of the *Energy Wall* supply in a number of scenarios to determine its possibilities and impossibilities as urban

¹Three different turbine states were introduced in section 4.2.4, energy generation corresponds to 'state two'.

renewable energy source. Because comparing power output without cost concerns is redundant, the LCOE plays the role of price signal to guide investment and encourage development, not to produce an accurate benchmark price. Conventional forms of energy have a competitive advantage over their renewable counterparts, not only in terms of up-front cost, but also in number of full load hours. Accordingly, it is not correct to equate LCOE levels of large-scale wind and solar plants in locations with favorable conditions with the LCOE of urban solar and wind micro-generation. Again, the distinction here can be made on the basis of full load hours. For this reason, although cost is the primary indicator of financial viability, it is important to take into account not only the LCOE of each technology but also future cost trends, potential cost reduction product of retrofitting strategies, social and environmental benefits, and grid arbitrage (when applicable) all within the context of the assumed system life.

7.1.2. Cost taxonomy

The first step towards understanding the costs of a project is to classify them in different categories. Because distributed wind projects and distributed solar projects have many common cost items, it is convenient to apply the same taxonomy in the wind, solar and hybrid configurations of the studied system. To increase transparency and also allow comparability with other projects, the classification employed in this analysis uses NREL's *The Distributed Wind Cost Taxonomy* [48] as a guide. The cost taxonomy is described as follows:

- CAPEX, including the wind turbine or solar modules and the required power electronics as well as the balance-of-station (BOS) costs, in Eur/kW
- OPEX, including all fixed and variable operation, maintenance costs as well as replacement costs when applicable, in Eur/kW-year.

The balance-of-station expenditure is split in the general subcategories tabulated below. Appendix B elaborates on the specific treatment that each cost component has received separately for wind and solar systems.

Cost category	Description
System Equipment:	Costs of the energy generating equipment and its support
Structural Infrastructure:	Labor, equipment and materials costs required for the foundation serving as the basis for the subsequent installation of the tower or the rack
Electrical Infrastructure:	Cables and switches costs required for wiring the technology to the utility interconnection
Installation:	Labor, equipment, material and logistic costs for site preparation and cleanup, installation of the technology and commissioning.
Transport:	Costs associated with transporting all materials from their whereabouts to the installation site including shipping and storage
Sales tax:	Tax rates are site-specific and vary also per installer
Zoning, Permitting, Interconnection (ZPI):	Fees, labor and time associated with obtaining the appropriate zoning approval, permits and interconnection agreements
Marketing, Overhead and Profit (MOP):	Includes the developer overhead costs including publicity and a profit margin to all costs

7.1.3. A note on cost variability

Installed prices vary widely across different wind and solar projects in the urban scale. To analyze and track costs several research institutes elaborate cost benchmarks based on project-level data from manufacturers, installers and developers. These reports show that pricing varies among benchmarks due to a diversity of data, methods and definitions (external variability) and also across similar projects of a unique dataset (internal variability). According to [18], these deviations arise from a number of reasons:

- Project characteristics
- Local market and regulatory framework
- Installer size, experience and business model

- Labor rates, taxes, permitting and interconnection processes
- Differences between projected cost and final price

The fact that significant variability exists, implies that the notion of a unique price is false. Therefore, caution and specificity are important when using cost benchmarks to approximate the costs of a new project. To provide a more robust outlook, the use of a set of recent cost benchmarks is recommended. As with any other estimate, each benchmark will have its merits and limitations that must be interpreted and applied appropriately [18].

In the case of solar installations, due to a maturing market stimulated by increased competition and better-informed consumers, installed prices have been narrowing over the past two decades [18]. This narrowing trend has not yet been observed in the small wind market. Distributed wind benchmarks still involve reduced sample sizes and inconsistencies in market segment definitions. As a matter of fact, the NREL has only very recently published a distributed wind taxonomy to address the urgent need for a standard method to analyze the costs of distributed wind systems [48]. The differences between small-scale wind and solar energy have been a recurrent topic throughout this report to justify the different treatment that both technologies have been given. Following the same line, the presented economic analysis has concentrated in understanding small-wind pricing a bit more in depth than its solar counterpart.

7.2. Noise-barrier-integrated wind system

The particularities of this wind energy system, making use of already existing stock of urban constructions, prevents the direct use of benchmark small-wind costs. There is a need to investigate strategies to bring cost breakdown closer to the system's reality. The applicability of project cost benchmarks reported in literature is questioned due to discrepancies among taxonomies, foundation types, business models, turbine sizes and tower structures. All such factors are highly influential and vary dramatically between projects.

7.2.1. The question of system scale

Classification of wind turbines is commonly made on the basis of rated or nameplate capacity. A small wind turbine is generally defined as a turbine with capacity ranging from < 1 to 100 kilowatts [25]. Within this range, turbine size, height, weight, and materials vary widely, resulting in an even wider range of costs. To establish comparability, average costs of small wind systems should be categorized into smaller groups of different turbine size segments. This is rarely the case for most published cost benchmark reports. For instance, the classification adopted in [2] presumes that turbines below 20 kW are more likely be used in residential applications and therefore classes them as residential. This means that a *Xzeres 442SR* turbine with rated power 10.4 kW and a weight of 1045 kg falls in the same category as a < 1 kW turbine weighting less than 130 kg. Transport, installation, logistics and handling requirements of these two types of turbines are clearly different and so are their costs. A comprehensive review of published wind energy cost reports was conducted and it was found that only three studies classified reported average installed costs of small wind in subgroups. Their findings are summarized in Table 7.1. Reported original values have been converted to 2018-Euros and are presented as capacity-weighted average costs. Note that, although the values correspond to different studies with their own methodologies, the message is clear; subgroup size matters. Results from CanWEA and LBNL suggest that turbines at the lowest end of the size range have the lowest installed costs. This fact, however, cannot be tracked when turbines are not classified in sufficiently small size groups like in PNLL's results. Such a conclusion is of up-most importance for this analysis because the turbine employed in the *Energy Wall* falls in this < 1 kW low-end small wind turbine category. The term *micro* will be used in this chapter to distinguish this low-end category from the others.

Equally important is to understand the differences between projected and realized costs. Installed costs reported by manufacturers may differ from final project costs due to location-specific factors affecting installation, permitting and shipping [4][25]. Small wind turbine costs also vary widely depending on the competitiveness of the market. For the same turbine size, manufacturers may charge more for a single turbine order than for a bulk turbine purchase [4]. On that note, reported distributed wind projects often employ a small number of turbines. For instance, 89% of 2016 distributed wind projects evaluated in [4], were single-turbine. These projects do not benefit from economies of scale available to larger projects. Therefore, wind system costs scale separately with increasing turbine size and increasing number of turbines installed. With project costs seldom published, there is limited understanding of the drivers of these variations. Note that a 300-meter long noise barrier fitting fifty *Energy Wall* segments has a wind installed capacity of roughly 35 kW. In terms of capacity, such a system should be labeled as commercial, however, the cost breakdown of a project

Turbine size kW	CanWEA [11] Eur/watt	Turbine size kW	LBNL [4] Eur/watt	Turbine size kW	PNNL [2] Eur/watt
0-1	1,63	0-2,5	3,74	0-20	9,71
1-10	4,05	2,5-10	5,77	21-100	6,00
11-50	3,16	11-100	4,06		
51-100	3,10				
100-300	0.98				

Table 7.1: Comparison between average installed costs of small wind projects based on different subgrouping systems from three reports published by renewable energy research institutes or associations; Canadian Wind Energy Association (CanWEA), Lawrence Berkeley National Laboratory (LBNL) and Pacific Northwest National Laboratory (PNNL).

involving 50 turbines is not comparable to the cost breakdown of single-turbine project, even if their rated installed capacity is 35 kW for both. For all these reasons, small wind cost benchmarking exercises based on collected cost data are to be evaluated carefully before making assumptions. With the purpose of achieving a consistent treatment of the individual costs, the insights from a *micro* turbine developer have been valuable. Cost data from real projects has been studied analytically to elucidate what are the real costs of *micro* wind turbine projects. The next section presents how the cost breakdown of the *Energy Wall's* wind system has been estimated.

7.2.2. Cost breakdown

As mentioned earlier, to increase transparency and allow comparability with other projects the classification below is inspired by NREL's *The Distributed Wind Cost Taxonomy* [48]. Clearly, there are some cost items that are particular to the wind system and its urban-integration characteristic. For this reason, a more detailed description of each cost category has been included in Appendix B. Prior to analyzing the costs involved in the noise-barrier integrated wind system, is important to understand how this integration is achieved. The mechanical bracket coupling the wind turbine onto the noise barrier is shown in Figure 7.1. A prototype of this bracket has been designed by a third party. As in every new design, safety concerns have resulted in a structurally over-dimensioned bracket due to the choice of large safety factors. For this reason, the prototype cannot be taken for pricing reference, however, is still representative of the future flange connecting the wind turbine to the noise-barrier.

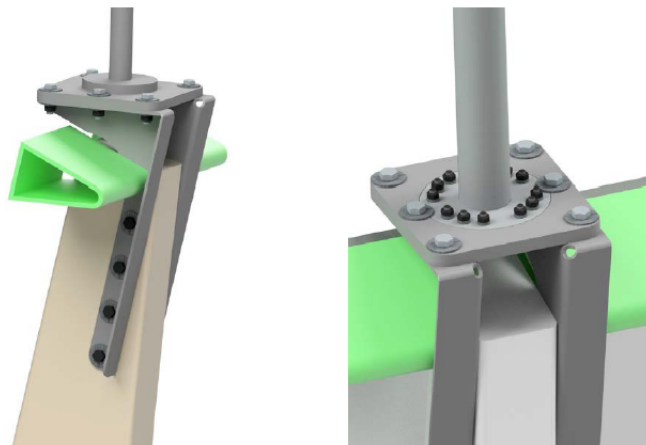


Figure 7.1: Noise-barrier coupling bracket prototype designed by Electronic and Mechanical Support Division (DEMO).

Due to the difficulty involved in pricing the bracket based on a single prototype and the absence of a similar project against which to validate the estimates, comparison with other systems is the only recourse to assess the cost of this installation. In this sense, the insights gained from the *micro* turbine developer interview constitute the starting point. Valuable information was obtained from comparing the cost breakdowns of two single-turbine projects; one roof-mounted and one employing a monopole. Both projects involved the same WindChallenge® turbine, differing only on the type of installation and support structure. With similar costs associated with cables and switches, installation, permitting and interconnection, the main cost driver

of both projects is clearly the structural infrastructure, which includes both materials and mounting.

- The roof-mounted installation does not require foundation and is, therefore, less cost intensive.
- On the contrary, the monopole mount is more expensive than a flat-roof mast and requires foundation.

Note that foundation comprises excavation, rebar assembly and concrete pour, which are not required for the noise-barrier-integrated turbine. Based on the above, the following can be inferred;

- The cost of a noise-barrier bracket mount is larger than the cost of a roof mount and smaller than the cost of a monopole installation.

Moving from a roof-mount to a monopole, structural infrastructure costs jump from 14% to 34% of the overall system cost. In terms absolute values, the increase is threefold. An intermediate value is assumed and the structural infrastructure of the coupling bracket is costed at 1000 Eur. To be compatible with NREL's taxonomy, costs associated with transport, taxes and MOP had to be included, as they are usually not provided by manufacturers. For those cost categories, percentages of total system costs obtained from recent cost benchmarks is considered appropriate. Transportation costs are assumed 2%, sales taxes 1% and overhead and profits 13% of the overall system cost [2][6]. Figure 7.2 shows the breakdown of costs for the configurations discussed above. Manufacturer roof-mount and monopole cost data have been modified for compatibility with the chosen taxonomy. All three configurations have the same system equipment costs (dark blue) and differ greatly in structural costs (light blue).

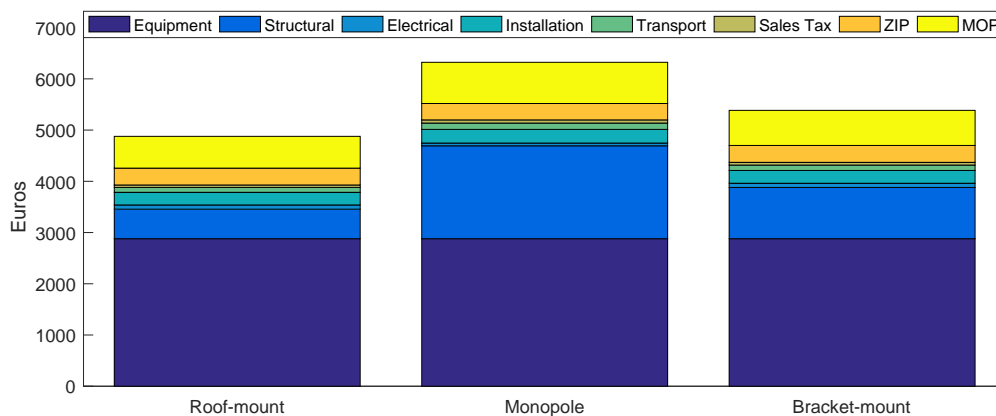


Figure 7.2: Cost breakdown of three single-turbine projects employing a commercial *micro* wind turbine on different mounting structures.

Following the nomenclature introduced in section 7.1, the costs discussed above constitute the CAPEX. Operation and maintenance (O&M) activities for small-wind systems also differ from those required for larger turbines. On one side, small wind turbines are much simpler mechanically and many have special-purpose designs aimed at reducing the number of moving parts and the need for maintenance [6]. On the other, distributed wind turbines are commonly installed individually which implies that traveling and equipment costs associated with maintenance activities are not spread across a number of turbines. Hence, reported O&M costs for small-wind systems tend to be unexpectedly high. For instance, a study of the 2016 U.S. distributed wind market found O&M costs estimates for turbines less than 5kW to be \$70/kW [4]. A much lower value of \$43/kW was reported in [2], a similar small-wind benchmark study sponsored also by an agency of the U.S. Government. Clearly, budgeting for maintenance of small-wind turbines has irreducible uncertainty as O&M costs are strongly project specific. Furthermore, among *micro* turbines manufacturers, some claim their products to be practically maintenance-free and others suggest simple annual inspections done from the ground and one inspection done by a qualified installer every 10 years of operation [16]. Contrary to what manufacturers may assert, the Warwick Wind Trials Project, a performance study of 26 building-mounted *micro* turbines, experienced multiple reliability issues throughout their one-year trial [15]. In view of this, to provide high operational availability and maximum performance, the noise-barrier-integrated wind system assumes the intermediate figure of 35 Eur/kW (~\$43/kW) of OPEX per year including replacement costs.

7.2.3. Cost reduction opportunities

Another issue is finding out what is really being saved in terms of materials, labor and money. Addressing the cost reduction that arise from economies of scale is problematic. The insights gained from the *micro* turbine developer interview constitute, also in this aspect, the starting point. Information from a multi-turbine project employing ten pole-mounted turbines was used to understand how costs scale with number of turbines. The most important observation to make from the comparison between both projects is that, for a single turbine, monopole structural costs are high (29% of overall system cost) but, as number of turbines increase, structural infrastructure becomes more cost-effective (19%). It is assumed that system costs for a noise-barrier coupling bracket will scale in the same fashion as in a project employing monopoles. It is the choice of a turbine manufacturer to apply a discount for a bulk turbine purchase thus, no assumption is made in this regard. For this reason, the system equipment costs are assumed to scale proportional with number of turbines. For the remaining costs, scaling factors for each category are calculated and then applied to the bracket-mount cost breakdown. The costs of a project employing ten bracket-mounted turbines including the effect of scale economies are obtained.

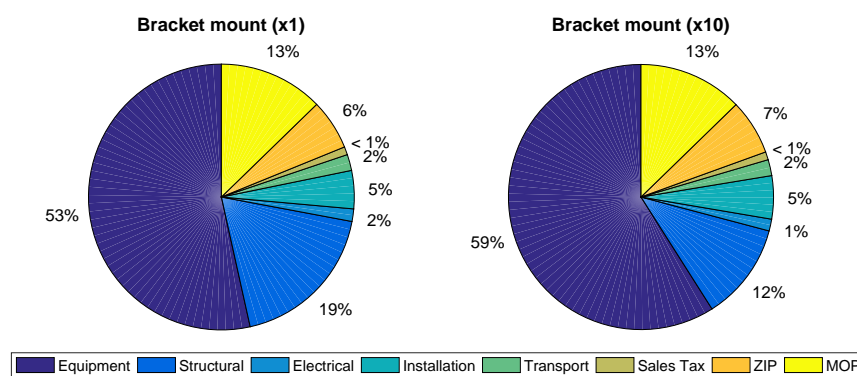


Figure 7.3: Cost breakdown comparison between a single-turbine project and a project employing ten turbines.

Figure 7.3 shows the cost breakdowns of a single- and a multi- turbine project employing a noise-barrier bracket system. Clearly, structural installation offers the greater economy of scale by moving from 19% to 12%. The other cost categories remain fairly constant. In absolute terms, there is a reduction in total cost of 10.3% and the price per turbine installed becomes 4,880 Eur. Additional cost reduction can be achieved by hybridization. Because balance-of-station costs are similar between distributed urban wind and distributed solar projects. Further analysis of system shared costs can be found in section 7.4.

7.2.4. LCOE range

To establish comparability, the LCOE has been calculated for a combination of system alternatives of varying structural infrastructure, project characteristics and wind resource². These alternatives are tabulated below.

System variable	Options	Description
Structural Infrastructure	FS/NB	Monopole free-standing (FS) and noise-barrier-integrated (NB) installations have been examined to illustrate the advantages that re-using existing urban stock can bring.
Project characteristics	S/M	Single-turbine (S) and multi-turbine (M) projects have been modeled to quantify the effect of economies of scale.
Wind resources	3/4	Two wind resources with hub-height mean wind speed levels around 3 m/s and 4 m/s have been used to understand how rapidly energy prices will decline with better wind resources.

²Annual energy yields obtained from the sensitivity analysis in section 6.2 have been used. The wind resources employed are Delft and STRN with mean hub-height speeds of 2.99 m/s and 4.35 m/s respectively.

The calculated LCOE values are displayed in Figure 7.4. A special nomenclature is used to identify each system alternative. For example, 'FS-S-3' represents the free-standing, single-turbine system sitting in a location with hub-height mean wind speed around 3 m/s. In this instance, the CAPEX of a single monopole has been used in combination with the annual energy yield obtained from the clean flow wind data from Delft, excluding in this way the effect of the noise-barrier. The system 'NB-M-4' represents the noise-barrier-integrated, multi-turbine system sitting in a location with hub-height mean speed around 4 m/s. Here, the CAPEX of the bracket-mount project employing ten wind turbines is used in combination with the annual energy yield obtained from STRN (see Table 6.2). In this second example, annual generation is orientation-dependent because the effect of the noise-barrier on the flow is included. To account for this variability, the LCOE is given in the form of a price range. Two main conclusions can be drawn from the results:

1. Noise-barrier integration offers a significant cost reduction opportunity with respect to a free-standing monopole, regardless of wind resource quality. The price decline is the largest in the less favorable wind resource (level 3) where the achieved reduction is between 16.5%-24.5% depending on noise-barrier orientation. The drivers of this cost reduction are:
 - Lowered CAPEX as a result of avoiding tower foundation.
 - Increased wind speed consequence of the wind concentrator effect of the noise barrier.
2. The impact of a slightly better wind resource is magnified when analyzed in LCOE terms. To be precise, the two wind resources employed in this analysis have a mean wind speed difference of 1.36 m/s. Translated into LCOE figures, this small difference is equivalent to 1 Euro per kilowatt-hour produced.

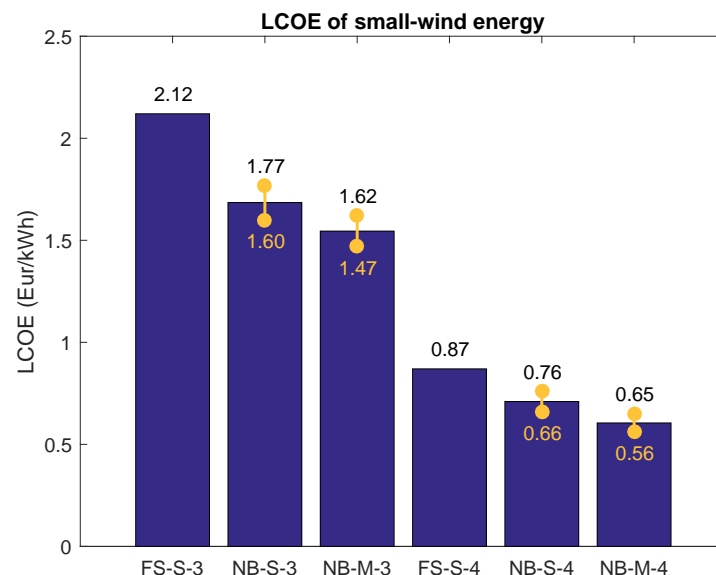


Figure 7.4: The calculated LCOE of small-wind for two system configurations; min/max ranges are given for those systems that have orientation-sensitive generation.

7.3. Noise-barrier-integrated solar system

The narrowing of variability in installed prices for distributed solar energy systems is consistent with a maturing market. Driven by supportive policies, residential and non-residential solar projects have been growing in size enhanced by an ever-increasing competition among installers and vendors and better-informed customers [18]. Among different published cost studies, the diversity of methods and market segment definitions is smaller than that of distributed wind benchmarks. It should be noted that wind turbines have a much wider nominal capacity range than solar modules, making the classification of wind energy projects more problematic. Different from the wind system, noise-barrier-integration of the solar system is comparable to roof-top installation, which makes published cost benchmarks a valid option for cost estimation.

7.3.1. The question of system scale

The question of system scale does not have the same relevancy in distributed solar systems as it has in small wind systems. The narrower range of solar module size and rated capacity contributes to better defined market segments and narrower price ranges. With cost benchmarks available for a number of system sizes, the estimation of the solar system cost simplifies.

7.3.2. Cost breakdown

This section looks at each of the costs of the distributed solar systems taxonomy separately and tries to identify major cost drivers and cost reduction opportunities. Also in this case, compatibility with the taxonomy adopted in the previous section is sought. Moreover, a detailed description of each cost category is presented in Appendix B. As previously discussed in section 7.1.3, the idea of a unique price is unrealistic. This applies for both solar and wind projects, however, the variability of solar photovoltaic pricing is well-documented in comparison. Based on the above, and mindful of the location dependency of price, the NREL's *U.S. Solar Photovoltaic System Cost Benchmark* [45] is taken the reference point for this analysis. This choice is made largely due to the level of detail that this benchmark provides, which is essential information to identify cost drivers and potential cost reductions. The aforementioned benchmark reported installed prices of 200kW non-residential solar systems at \$1.85 per watt as of the first quarter of 2017. Another report from LBNL found that during the first half of 2017, median installed prices fell by an additional \$0.4/W [32]. Taking this into account, the selected price per watt installed is fixed at \$1.45/W (or 1.17 Eur/W). Figure 7.5 shows the distribution of costs. Note that marketing, overhead and profit costs, often referred to as 'soft costs' make up for 30% of the total system cost. These costs include engineering, procurement and construction direct and indirect labor as well as markup and supply chain costs.

To reiterate, the choice of NREL's benchmark is made mindful of the location dependency of solar system installed prices. In countries with more competitive solar photovoltaics markets, prices may be lower. The absence of a well-established taxonomy to analyze the costs of distributed solar systems in Europe is a bottleneck. As already mentioned, compatibility with the taxonomy adopted in the small-wind section is important. High degree of cost granularity is required in this analysis in order to identify potential cost-sharing opportunities that arise from hybridization. Many published European reports state the wholesale price per Wp-installed without breaking down overall costs into smaller cost components. To give one example, a study of the photovoltaics market in the Netherlands as of the first quarter of 2016 reported prices of 1.27 Eur/Wp and 1.15 Eur/Wp for systems sizes 50 kWp and 500 kWp respectively, including installation [53]. No additional cost breakdown is provided and no mention is made to other cost categories such as transport, ZIP nor MOP. Similarly, Fraunhofer Institute's *Recent facts about photovoltaics in Germany* reported average net system price for 10-100 kWp rooftop systems at 1.27 Eur/Wp in the fourth quarter of 2016 [54]. The study indicates that BOS costs are responsible for 52% of the total investment, but these are not broken down into cost elements. Being able to trace back the origins of each cost item is essential to ensure that the costs of solar and small-wind systems are treated consistently. Adopting NREL's benchmark, on the other hand, has the advantage of keeping the analysis transparent. It is noteworthy, however, that the system price assumed in this report (1.17 Eur/Wp) compares favorably with the figures above.

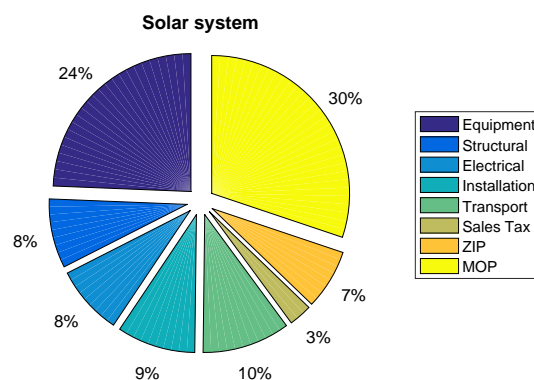


Figure 7.5: Cost breakdown the noise-barrier-integrated solar system adapted from [32].

The NREL's *Best Practices in Photovoltaic System Operations and Maintenance* report recommends planning for annual O&M costs equal to 1% of the system initial cost. For a single *Energy Wall* segment, this means 48 Eur/year. It is assumed that the inverter will be replaced in year 15 of the system lifetime at an additional cost of 530 Eur (or 0.13 Eur per watt installed [45]). As previously discussed in section 4.3.3 no cleaning regimen is employed due to its unlikely cost-effectiveness [41].

7.3.3. Cost reduction opportunities

The wide assortment of soft costs has been the center of attention of industry and policymakers who have placed significant efforts on reducing them. These costs are likely to vary by location and type of installer. Therefore, for a noise-barrier-integrated solar system installed in a location where supportive schemes are present, one could expect reduced soft costs and an overall lower installed price. As previously mentioned, some balance-of-station costs can be shared between distributed wind and solar systems. Section 7.4 presents the additional cost reductions offered by hybridization.

7.3.4. LCOE range

The LCOE of the noise-barrier-integrated solar system reflects the dependency of solar energy production on noise-barrier orientation. Moving from a noise-barrier facing North to a South oriented one, the LCOE halves. It is important to recall that solar modules were installed to match the inclination of the noise-barrier resulting in a suboptimal configuration. To maximize the amount of irradiation reaching the solar modules, a 55° altitude and 180° azimuth are needed (refer to Figure 4.11 for a contour plot showing incident annual irradiation as a function of module altitude and azimuth). The developed generation model is reran changing only those parameters to obtain the annual energy production of an optimum-tilt (OT) system and then calculate its LCOE. The results are shown in Figure 7.6 for both suboptimal and optimal systems. Two important observations can be made:

1. Noise-barrier orientation is of utmost importance and should be taken as a heavy-weighted criteria during planning of a prospect *Energy Wall* project.
2. Sacrificing optimal module altitude configuration for a better physical integration between the noise-barrier and the solar modules does not come at a high cost so long as the azimuth is relatively close to its South optimum (about 3 cents/kWh higher).

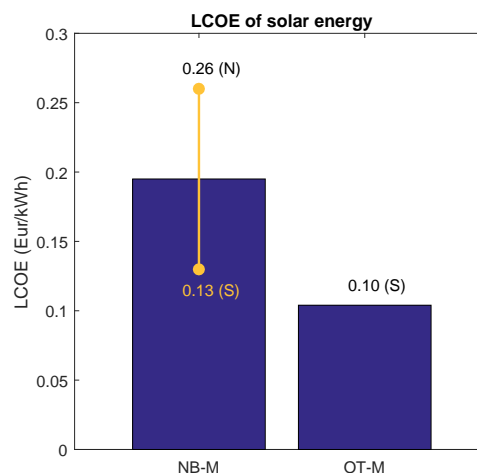


Figure 7.6: The calculated LCOE of the noise-barrier-integrated solar system (NB-M) and the same system installed at an optimum tilt angle (OT-M); min/max correspond to North (N) and South (S) noise-barrier orientation.

7.4. Noise-barrier hybrid system

This section describes the economics of the hybrid system altogether. Given the novelty of the system, there is little reference or guidance on how hybridization can affect costs. However, based on the analysis presented in sections 7.2 and 7.3 above, it is possible to make well-educated guesses and provide a qualitative picture of the *Energy Wall* in terms of its costs.

7.4.1. Cost breakdown

Following the line of thought of the previous sections, the same taxonomy is employed. Each individual cost category has been analyzed to identify cost items present in both wind and solar systems. A number of cost reduction opportunities have been identified in those costs groups with high degree of compatibility between systems. A simple cost-sharing methodology has been used on the basis of an assumed hybridization factor (HF) for each cost category. This factor is then applied separately to that particular cost in the solar and wind systems. By adding the resulting figures, the hybrid cost is obtained. The assumed 'hybridization factors' are summarized below.

Cost Category	HF	Justification
ZIP & MOP	1/2	Soft costs are commonly paid one time per project. Accordingly, ZIP and MOP cost categories receive a factor of 1/2.
Electrical Infrastructure	1/2	Trenching and backfill activities required for underground wiring are evenly shared between the two systems. In addition other, grid interconnection and other electrical costs are also common. Hence, it is assumed that electrical infrastructure costs hybridize with a 1/2 factor.
Installation	2/3	A number of cost items associated with installation such as labor and equipment for site preparation have cost-sharing potential. To be in the conservative side, a factor of 2/3 has been assumed.
Others	1	The degree of compatibility found in the other cost categories is non-existent or not high enough to justify a cost-sharing opportunity and, therefore, are given a factor of 1.

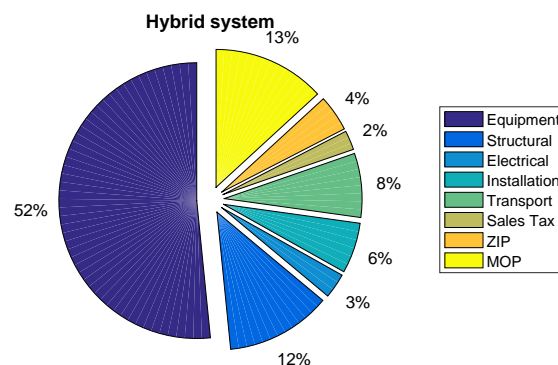


Figure 7.7: Cost breakdown the noise-barrier hybrid system.

Figure 7.7 shows the resulting cost breakdown of the hybrid system. System equipment includes the wind turbine, the solar modules and their pertinent power electronics, which taken all together contribute a little over half of the total *Energy Wall* cost. The remaining half is divided between soft costs and construction related costs. The installed price of a non-subsidized multiple segment *Energy Wall* is 7850 Eur/segment, or what is the same 1.64 Eur/watt. This amount is 19% smaller than the cost of installing the systems separately.

7.4.2. LCOE range

Having determined the cost of turning a noise-barrier into a hybrid sustainable energy generation system, the next step is to put this price into perspective by evaluating the system's LCOE. The results are displayed in Figure 7.8 for the same two wind resources that were explored in LCOE calculations of section 7.2.4. Here, 'EW-M-3' represents the hybrid *Energy Wall* multi-segment system sitting in a location with mean wind speeds around 3 m/s at hub height. Likewise, 'EW-M-4' represents the same system sitting on a location with more favorable wind resources of around 4 m/s hub height mean speed. Note that through hybridization, the weight of the LCOE of small-wind is lessened. The proportion ratio of installed capacity of each generation technology is roughly 6/1, or what is the same, the system has installed 6 kW of solar power per each kW of wind power. As a consequence, the impact of a better wind resource is clearly downgraded and partially

replaced by the higher impact of noise-barrier orientation. Minimum and maximum values correspond to North (N) and South (S) orientation, respectively.

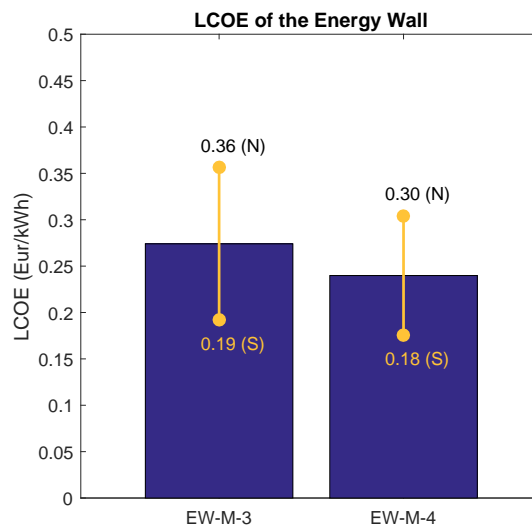


Figure 7.8: The calculated LCOE of the hybrid *Energy Wall* system for two sites of differing wind resources.

7.5. Discussion

Throughout this chapter, the noise-barrier-integrated wind system, solar system and hybrid system have been investigated one at a time. The diverse reality of urban environments and their inherent complexity are the reason of assessing the three systems separately. Although it would be ideal that all noise-barriers were installed facing towards South or oriented perpendicular to the prevailing wind direction, this would interfere with the primary purpose of a noise-barrier. One attribute of the *Energy Wall* concept is its adaptability to the local environment and resources. Its modular design makes it suitable for a variety of circumstances. One important point to remember is that, the aim of this study was not to demonstrate the economic efficiency of this novel concept but to assess its potential comprehensively and recognize its barriers and opportunities. At this point, the question that arises is,

How should the merits of each system be evaluated?

Evaluation criteria are inevitably somewhat subjective. A variety of different judgments will come from the wide range of players in the energy sector. Utility companies, technology developers, different levels of governance, renewable energy associations and educational institutions will most certainly value each system differently depending on their interest. Moreover, the desirability of a system varies geographically and temporarily and evolves technologies improve. An attempt to illustrate these dependencies has been included in appendix C in the form of a decision-making tree. A rule guiding this discussion has been the effort to be impartial and present the findings objectively. Results for the three potential systems in which a noise-barrier segment can be converted into are summarized in Table 7.2. The values that are dependent on noise-barrier orientation are given as ranges. Some results are provided per segment; the standard *Energy Wall* segment was previously defined as the 6-meter long noise-barrier stretch fitted with one urban wind turbine and 12 solar panels on a 80° tilt. The total installed capacity of a single segment is 4.78 kW, from which 4.08 kW are solar power and 0.7 kW are wind power.

The first row of Table 7.2 indicates the energy generated by one segment from solar and wind resources separately over the period of one year. Note that the installed capacity of one segment is dominated by solar power. Therefore, these values do not provide enough information to assess the performance of each technology. Instead, this information is given by the capacity factors in the next row. While the solar system generates more kWh per each kW installed, the real gap between solar and wind performance is not as large as annual generation values may suggest. The reported capacity factors are overall low. This is due to the non-ideal conditions of the project site in comparison with larger projects targeted for areas with greater wind speeds and

	Only wind	Only solar	Hybrid
Energy, in kWh/segment/year	223 - 246	1505 - 2992	1740 - 3227
Capacity factor, in %	3.6 - 4.0	4.2 - 8.4	4.2 - 7.7
CAPEX, in Eur/segment	4,880	4,800	7,850
LCOE, in Eur/kWh	1.46 - 1.62	0.13 - 0.26	0.19 - 0.36

Table 7.2: Summary of main results for the different potential systems for the local solar and wind resources of Delft.

higher solar irradiation. Even so, the system configuration employing only solar generation over-performs, on average, the other two systems.

The third row, CAPEX, reflects the current status of distributed wind and solar markets. The various forms of research and policy support that have been fruitful in growing the market of solar energy have had the unintended consequence of retarding the development of distributed wind technologies [6]. With almost the same CAPEX and 1/6 of the installed capacity, the small-wind system is far from achieving similar payback timeframes than the solar system. This result is consistent with the maturing solar market and its sustained decline in installed prices over the last two decades, increasing competition among installers and vendors and gaining customer confidence [6]. In the interim, wind energy research has been directed towards large wind turbines and the small-wind market has stagnated [48]. Clearly, the state of knowledge and experience of small-wind is lagging behind and the obtained LCOE values are yet another bit of proof. The most important observation to make from the last row of Table 7.2 concerns the LCOE of the hybrid system. The figures are close to those of the solar system; partly due to the greater solar installed capacity, and partly due to cost-sharing and its subsequent reduction in CAPEX. The three direct, visible benefits arising from hybridization are:

- Reduction in CAPEX due to cost-sharing between solar and wind (19% less with respect to installing the systems separately)
- Possibility to install a small-wind system at lowered LCOE levels and consequent shorter payback time frame
- More stable energy supply than with only solar or only wind (at times when one resource is affected by intermittency, the other will may still generate)

Hybridization can potentially have indirect, non-measurable, positive results. These are illustrated in the following diagram.

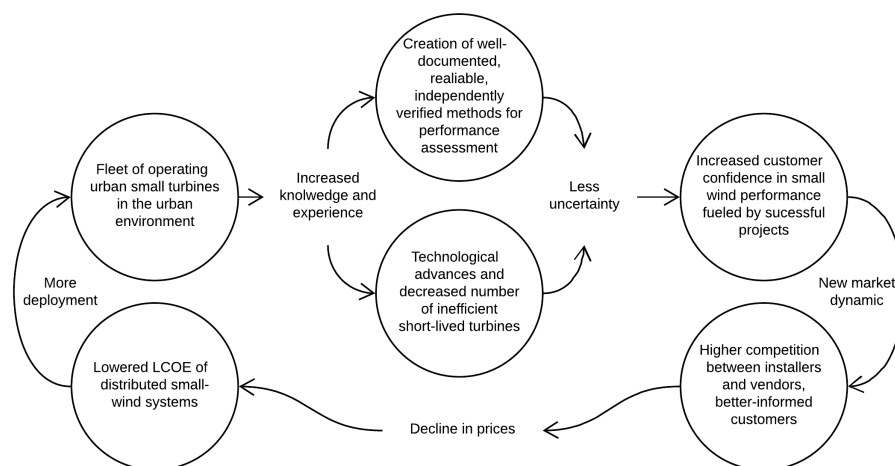


Figure 7.9: Positive cycle of small wind energy market development

It can be argued that similar market forces rule the industries of distributed solar and distributed wind energy. Learning from solar industry successes is both appropriate and necessary. To set the small-wind market on the path to growth, however, some action must be taken to fill the knowledge gap on the link between projected and actual performance of this technology. More reliable methods are needed to determine how

much extractable wind energy realistically exists in urban sites. But all these will never be accomplished if small-wind research and development remains lost in the shadow of large wind turbines. There is a need to redirect attention towards smaller wind turbines. The hybrid *Energy Wall* can contribute greatly to this end by enabling small-wind deployment at lowered LCOE. The opportunities that hybridization brings should not be limited to those tangible and/or measurable. Critical examination is needed to bring creative perspectives to a complex and rapidly evolving field. Urban renewable energy is receiving increased interest and small-wind technologies are not mature enough to follow the dynamic market of solar photovoltaics. Therefore, is necessary to tee up issues for future study and address the barriers hindering urban wind energy generation.

There is no right answer to the question formulated at the beginning of this section. The merits of each system depend on project-specific aspects such as what are the local energy resources and what is the intended use of the generated electricity. Another important aspect is whether or not the sole purpose is energy production or there are other interests behind the project such as contributing to a circular urban metabolism, diversifying energy sources or expanding the renewable component of a country's energy mix. How each system can contribute, depends on the drivers and value proposition of a particular project.

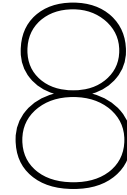
7.5.1. The effect of discount rate

A discount rate of 3% has been assumed throughout this economic analysis. Having arrived at this point, is important to recall that the interest rate at which a particular investment is discounted has an underlying effect on its economics. The implications of the strong dependency of LCOE calculations on the choice of discount rate were discussed in section 7.1 at the beginning of this chapter.

For the sake of completeness, the impact of varying discount rate between 0% and 7% has been analyzed. The results are shown in Table 7.3 for the three system configurations. Increasing the discount rate from 3% to 7% increases the LCOE between 44% and 23%, depending on the system. In contrast, in the extreme case of a discount rate of 0%, the LCOE reduces between 14% and 23%, also depending on the system. This asymmetry is due to the impact of costs incurred over the lifetime of each system, such as replacement costs and OPEX. Regardless of its causes, the fact that a substantial variability exists in the calculation of LCOE underscores the need for caution when comparing LCOE values among different projects. This is the reason why a comparison with benchmark LCOE values of other generation resources is not included in this economic assessment. For fairness and consistency, the use of LCOE has been restricted to internal comparison across the three studied system configurations.

	Only Wind	Only Solar	Hybrid
LCOE (Eur/kWh) at:			
0% discount rate	1.26-1.39 (86%)	0.10-0.20 (77%)	0.16-0.29 (84%)
3% discount rate	1.47-1.62 (100%)	0.13-0.26 (100%)	0.19-0.36 (100%)
7% discount rate	2.11-2.33 (144%)	0.16-0.33 (123%)	0.25-0.46 (132%)

Table 7.3: LCOE in Eur/kWh of each system at different discount rates



Conclusions and Recommendations

This work presents a modular energy generation system with an innovative noise-barrier integration feature. This novel concept, formally known as the *Energy Wall*, is designed to capture the local renewable energy resources of cities and transform them for urban use. This paper embarks on a comprehensive assessment of the potential of this system taking a full approach from experimental data to energy and cost modeling.

The study area located in Delft, the Netherlands, has provided the basis for the energy generation models in addition to valuable anemometric data used to investigate how a noise-barrier affects the local wind resources. Experimental measurements have demonstrated the existence of a wind concentrator effect arising from the interaction of the noise-barrier with urban wind flows. This effect was found to be weakly correlated with streamline velocity and strongly correlated with flow perpendicularity, reaching a relative increase in wind speed of 30% in some cases. Depending on the direction distribution of local winds, this effect can lead to a 36% increase in annual energy yield. While the results were seen positively, describing the physical form of an inhomogeneous system has irreducible uncertainty. A great amount of anemometric data is needed to further understand and characterize the variability and complexity of urban wind flows and their interaction with different urban forms. As a matter of fact, the inability to consistently and accurately predict performance of urban wind turbines impacts the market of small-wind negatively, and is partly due to the relatively high costs and long-time frames of accurate site assessment. Current site assessment methodologies become less robust for low, highly variable wind regimes. In an effort to test this robustness, the impact of small variations in input parameters of the vertical wind profile scaling technique has been investigated. Results have shown that inaccuracies on z_0 and d_0 estimates (around ± 20 centimeters) introduce a 8% relative error on the estimated annual energy yields. Discrepancies among urban wind modelers on the methods used to parameterize vertical wind profiles within the urban boundary layer evidence a knowledge gap. There is a need of well-documented, reliable, independently verified methods for assessing the performance of small-wind turbines in urban environments.

Assessment of energy profiles has shown that a single *Energy Wall* segment, fitted with 12 PV modules and one small wind turbine, generates per year almost enough energy to supply the annual demand of a typical Dutch residential household (95%). However, the great disconnection between the times at which energy is produced and the times at which is demanded poses burdens on the viability and cost-efficiency of stand-alone operation. Grid-connection has arisen as the system configuration that meets the concerns of continuity of supply and minimized waste energy and still holds great promise for enabling an economic return on the system. This is nonetheless based on the current technological situation. Future works should explore the new opportunities that efficiency improvements, advanced storage solutions and system costs reductions are likely to bring. With the current electric power grid gradually evolving towards a smart power grid and the diversification of electric loads new possibilities will arise, opening interesting lines of research. There is a need to explore other types of near-road energy demands, particularly interesting are those using hydrogen as the energy carrier.

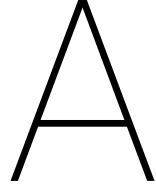
Cost modeling findings indicate that, if a discount rate of 3% and a system lifetime of 20 years are assumed, the levelized cost of the energy (LCOE) generated by a multi-segment *Energy Wall* in the studied area

utilizing the local solar and wind resources, ranges between 0.19-0.36 Eur/kWh depending on noise-barrier orientation. These figures are not valid if not accompanied by understanding of the various sources of price variability. One clear example is the small-wind system; for different combinations of wind resource and assumed discount rate, the LCOE range becomes 0.56-2.33 Eur/kWh. Pricing variability underscores the need of adopting a critical approach to interpreting LCOE prices of energy technologies in general, but more specifically of technologies that are still at development stage.

The energy generated by the *Energy Wall* is solar dominant (85%-93%), partly due to the larger installed capacity of solar power and partly due to the highly variable and circumstantial urban wind resource. Analysis of energy output sensitivities has provided valuable information that can be translated into practical guidance for technology developers and engineers. To determine which noise-barrier section is best suited for *Energy Wall* conversion, greater priority should be given to optimizing orientation for solar generation as it has a larger effect on the overall system output and economics. The contribution of wind energy changes mainly with wind resource quality. However, these changes are minimal when projected on the overall system cost. As a matter of fact, the small-wind contribution can hardly be justified its profitability. The benefits brought by the wind concentrator effect alongside with the cost reduction achieved thanks to noise-barrier-integration (14.5% if compared with a free standing monopole) and cost allocation between subsystems (19% if compared with installing the two subsystems separately) is not enough to counterbalance the decrease in efficiency caused by the less ideal conditions of the system with respect to other systems targeted for more windy areas. Results show that capacity-weighted investment required to include a small-wind subsystem remains high in comparison with the solar counterpart (nearly sixfold). This is consistent with the current status of distributed solar and wind markets. The sustained rapid growth of the former has had the unintended consequence of retarding the development of the latter.

The stagnant small-wind market needs to learn from solar industry successes to keep pace with the rapidly evolving field of urban energy generation. The *Energy Wall* can contribute greatly to this end by enabling small-wind deployment at lowered levelized cost of energy (LCOE). With more deployment comes more knowledge and experience, essential ingredients for performance improvements. Ultimately, better information and stimulated competition can bring a decline in prices. The hybrid system presented in this thesis has the uniqueness to serve as a stepping-stone for the wind market in urban environments. Analogously, hybrid cars attract buyers in search for fuel-efficient cars without the range limitation and the higher price tag of all-electric alternatives. With all major car producers engaged in developing more efficient batteries, a breakthrough in battery technology is all that is lacking to make all-electric vehicles cost competitive [23]. With wind energy research and development programs heavily concentrated on large wind turbines, a breakthrough in small-wind technology is, nonetheless, unlikely. There is a need to redirect research efforts and bring creative perspectives to the complex field of urban wind energy harvesting. By means of transforming urban regions into more productive ones, sustainability can be enhanced, contributing to more circular urban metabolisms, creating value and identity.

Out of the research questions that have guided this work, only one remains unanswered. The current knowledge and experience in small-wind performance is insufficient to determine *how much wind energy potential realistically exists in urban sites*. There is a need of empirical evidence to verify the theory and understand the practical implications of urban aerodynamics on the wind resources of cities. Only then, small-wind technology will be put in a position to redress its competitive disadvantage with respect to urban solar energy. With the above, the need of that future research focused on addressing the knowledge gap hindering urban wind development is underlined. This thesis has contributed in the field of urban-integrated energy systems by recognizing the possibilities of a noise-barrier-integrated energy generation concept and identifying critical gaps in the understanding of urban wind energy resources. To address these gaps, the *Energy Wall* is presented as a cost-efficient strategy to enable small-wind deployment and thereby educate the urban wind market.



Fluid Dynamics Model

Standard Test Conditions (STC) were quoted in section 4.3.2 as the most common standard used by manufacturers to rate the power of solar modules and yet, generally, not representative of the real working conditions. To address this issue, a fluid dynamic thermal model has been implemented to produce more realistic estimates of solar module working temperature T_m at each point in time. The thermal model, an adaptation from the work done by [5] and [17] with some minor additions, is explained in this Appendix.

A.1. Model framework

The model builds on a heat transfer balance between the solar module itself and the surroundings. Three important assumptions are made,

$$\dot{Q}_{module} = q_{sun} - q_{conv.} - q_{rad.(ground)} - q_{rad.(sky)} - q_{cond.}$$

- The module is seen as a single mass with uniform temperature T_m , which is not entirely realistic because modules are made of various materials and layers. This assumption is justified to produce an accurate representation of the true working temperature of the model because solar cells have relatively low thickness and heat capacity.
- Steady-state condition is considered over each ten-minute time step. The time lag between a change in irradiance and the respective change in model temperature is in the order of seven minutes. Because this time lag is shorter than the time step used in the model, the steady-state assumption is considered valid.
- Conductive heat transfer through the mounting structure is neglected due to the small area of contact. Therefore, the term $q_{cond.}$ drops.

The rate at which T_m changes with time is a function of module irradiance G_m , ambient temperature T_a , ground surface temperature T_{gr} and sky temperature T_{sky} and can thus be expressed as,

$$mc \frac{dT_m}{dt} = \alpha G_m - h_c(T_m - T_a) - \epsilon_{back} \sigma (T_m^4 - T_{gr}^4) - \epsilon_{top} \sigma (T_m^4 - T_{sky}^4) \quad (A.1)$$

h_c = Convective heat transfer coefficient (W/m^2K), see section A.2.1

α = Absorption coefficient (-), see section A.2.3

ϵ_{top} = Emissivity of the front glass surface (-), see section A.2.3

ϵ_{back} = Emissivity of the back surface (-), see section A.2.3

σ = Stefan Boltzmann constant ($\sigma = 5.670 \cdot 10^{-8} W/m^2K^4$)

Under steady-state conditions, the left-hand side of heat balance of Equation A.1 becomes zero. The two terms describing top and back radiative heat exchange are redefined using the algebraic identity $(a^4 - b^4) = (a^2 + b^2)(a + b)(a - b)$. With these newly defined parameters, $h_{r,sky}$ and $h_{r,gr}$, the simplified energy balance in

Equation A.4 is obtained. This simplification is convenient because $h_{r,sky}$ and $h_{r,gr}$ are relatively insensitive to changes in T_m and can be considered constant. As a matter of fact, a 10°C change in T_m will result in a variation of the term $(T_m^2 - T_{sky}^2)(T_m - T_{sky})$ smaller than 5%.

$$h_{r,gr} = \epsilon_{back} \sigma (T_m^2 + T_{gr}^2) (T_m + T_{gr}) \quad (A.2)$$

$$h_{r,sky} = \epsilon_{top} \sigma (T_m^2 + T_{sky}^2) (T_m + T_{sky}) \quad (A.3)$$

$$\alpha G_m - h_c (T_m - T_a) - h_{r,gr} (T_m - T_{gr}) - h_{r,sky} (T_m - T_{sky}) = 0 \quad (A.4)$$

This expression can be further elaborated to become a function of T_m as shown in Equation A.5. A solution can be found iteratively by assigning an initial T_m and updating $h_{r,sky}$ and $h_{r,gr}$ in each iteration. Generally, five iterations will lead to a nearly exact solution.

$$T_m = \frac{\alpha G_m + h_c T_a + h_{r,sky} T_{sky} + h_{r,gr} T_{gr}}{h_c + h_{r,gr} + h_{r,sky}} \quad (A.5)$$

A.2. Model Parameters

After elaborating on the equations governing this fluid-dynamics model, it is necessary to explain how the remaining unknown parameters can be calculated. The following properties of air have been assumed.

Property	Symbol	Value
Heat capacity, J/kg · K	c	1008
Heat conductivity, W/m · K	k	0.0264
Density, kg/m ³	ρ	1.165
Dynamic viscosity, kg/m · s	μ	$1.87 \cdot 10^{-5}$
Kinematic viscosity, m ² /s	ν	μ/ρ

Table A.1: Air properties at 30°C.

A.2.1. Coefficients for convective heat transfer

The overall convective heat transfer coefficient has two separate components, one for the top surface and one for the rear. This section explains in detail how these two coefficients can be calculated.

$$h_c = h_c^T + h_c^B \quad (A.6)$$

Top Surface. To estimate the top surface convective heat transfer coefficient, it is useful to make a distinction between free heat transfer (h_{free}), forced laminar heat transfer ($h_{forced-L}$) and forced turbulent heat transfer ($h_{forced-T}$). The Nusselt number Nu expresses the ratio between convective and conductive heat transfer and can be used to find h_{free} according to,

$$Nu = \frac{h_{free} D_h}{k} = 0.21 (Gr_x Pr)^{0.32} \quad (A.7)$$

where k is the heat conductivity of air, g is the gravity acceleration, β is the volumetric thermal expansion coefficient of air (approximated by $1/T$) and the Prandtl number Pr is the ratio between momentum and thermal diffusivity (commonly taken 0.71 for air). The hydraulic diameter D_h of a solar module of length L and width W is,

$$D_h = 2LW / (L + W) \quad (A.8)$$

The Grashof number Gr characterizes the ratio of buoyancy to viscous forces, thus, the degree of free convection. In the case of a solar module, the degree of free convection depends on the sine of the tilt angle θ_m at which the module is installed.

$$Gr = \frac{g \beta (T - T_a) D_h^3}{\nu^2} \cdot \sin(\theta_m) \quad (A.9)$$

The importance of the term $\sin(\theta_m)$ can be understood with the following example. Intuitively, free convection should be easiest when the solar module is vertical. Thus, at $\theta = 90$ the term $\sin(\theta_m)$ becomes 1 and

Gr automatically peaks. Contrarily, a flat module with $\sin(\theta_m) = 0$ will have virtually nonexistent free convection and Gr will become zero.

The distinction between laminar and turbulent regimes is made following the same criteria as in [5]. It is assumed that laminar flow extends until wind speeds of 3 m/s and the flow becomes turbulent afterwards. With Equations A.10 and A.11 below, laminar and turbulent convective heat transfer coefficients can be calculated.

$$h_{\text{forced-L}} = \frac{0.86 Re^{-0.5}}{Pr^{0.67}} \rho c_{\text{air}} u \quad (\text{A.10})$$

$$h_{\text{forced-T}} = \frac{0.028 Re^{-0.2}}{Pr^{0.4}} \rho c_{\text{air}} u \quad (\text{A.11})$$

where u is the wind speed at the height of interest and ν , ρ and c are the kinematic viscosity, the density and the heat capacity of air, respectively. The Reynolds number Re is the ratio between inertial and viscous forces expressed by,

$$Re = u D_h / \nu \quad (\text{A.12})$$

By combining the free and forced (either laminar or turbulent) heat transfer coefficients obtained as described above, the mixed convective heat transfer coefficient can be calculated.

$$h_{\text{mixed}} = h_c^T = (h_{\text{forced}}^3 + h_{\text{free}}^3)^{1/3} \quad (\text{A.13})$$

Rear Surface. The rear surface convection is expected to be lower than the top. One approach to calculate the rear surface convection coefficient is simply by scaling the convection coefficient calculated for the top surface according to,

$$h_c^B = R \times h_c^T \quad (\text{A.14})$$

The scaling factor R can be calculated based on the following energy balance,

$$\alpha G_m - h_c^T (T_{\text{INOCT}} - T_a) - h_{r,\text{sky}} (T_{\text{INOCT}} - T_{\text{sky}}) = h_c^B (T_{\text{INOCT}} - T_a) + h_{r,\text{gr}} (T_{\text{INOCT}} - T_{\text{gr}}) \quad (\text{A.15})$$

It is now useful to define R as the ratio between the actual and the ideal heat loss from the back side,

$$R = \frac{h_c^B (T_{\text{INOCT}} - T_a) + \epsilon_{\text{back}} \sigma (T_{\text{INOCT}}^4 - T_{\text{gr}}^4)}{h_c^T (T_{\text{INOCT}} - T_a) + \epsilon_{\text{back}} \sigma (T_{\text{INOCT}}^4 - T_a^4)} \quad (\text{A.16})$$

Based on the heat balance of Equation A.15, the numerator of Equation A.16 can be elaborated leading to the final scaling factor at INOCT conditions,

$$R = \frac{\alpha G_m - h_c^T (T_{\text{INOCT}} - T_a) - h_{r,\text{sky}} (T_{\text{INOCT}} - T_{\text{sky}})}{h_c^T (T_{\text{INOCT}} - T_a) + \epsilon_{\text{back}} \sigma (T_{\text{INOCT}}^4 - T_a^4)} \quad (\text{A.17})$$

A.2.2. Sky temperature estimation

The sky temperature is a function of the measured ambient temperature, humidity and cloud cover. A common approximation is to assume sky temperature equal to ambient temperature on cloudy days, when cloud cover (cc) is above 6 okta. On clear days, however, sky temperature be lower. In this model, the following logic is implemented to estimate sky temperature,

If $cc \geq 6$

$$T_{\text{sky}} = T_a$$

Else if $cc < 6$

$$T_{\text{sky}} = \frac{cc}{6} T_a + \left(\frac{6 - cc}{6} \right) \cdot 0.0552 \cdot T_a^{3/2} \quad (\text{A.18})$$

This approach is different from the one reported in [5] as it has proven to produce a smoother temperature profile and avoid unrealistic temperature drops between consecutive time steps.

A.2.3. Absorptivity and emissivity

Absorptivity can be understood as the fraction of incident radiation that is converted into thermal energy. Equation A.19 shows that this parameter is related to the reflectivity (R) of the module and also its efficiency.

$$\alpha = (1 - R)(1 - \eta) \quad (\text{A.19})$$

Emissivity can be understood as the capacity of a material to emit energy as thermal radiation. In this case, a different value is used for the front glass surface and the back surface of the solar module. The values reported in [5] are $\alpha = 0.1$, $\epsilon_{top} = 0.84$ and $\epsilon_{back} = 0.89$ and also used in this model.

B

Detailed Economics

This appendix gathers information relevant to the economical assessment performed in chapter 7. For a consistent treatment of system costs, the same taxonomy has been used to classify the costs of all three investigated systems, only wind, only solar, and hybrid. Because not all cost items are shared among solar and wind systems, a more detailed explanation of cost categories is deemed appropriate.

B.1. Description of wind system costs

This section looks at each of the costs of the small wind taxonomy separately and tries to identify major cost drivers and cost reduction opportunities. As mentioned in chapter 7, to increase transparency and allow comparability with other projects the classification below is inspired NREL's *The Distributed Wind Cost Taxonomy* [48]. Some minor modifications have been introduced to include the particularities of the urban-integration characteristic and extend this classification system to the solar and hybrid configurations.

Equipment System. This category is comprised only by the wind turbine in this case. Commonly, this category includes the costs of the tower for those systems requiring one. Reported averages in wind turbine prices vary widely depending on rated capacity but commonly, smaller turbines come at higher costs per kW. Values range roughly from 1,500 to 2,500 Eur/kW depending also if the costs reported by manufacturers include markup. The selected turbine has a price tag of 2,880 Eur including the inverter as specified on the manufacturer's website. Equipment system costs often account for more than 50% of the total project cost.

Structural infrastructure. This category takes the name 'Foundation' in the NREL's taxonomy and comprises excavation, rebar assembly and concrete pour. Foundation costs make up around 10% of the total project expense with averages ranging from 1050 to 480 Eur/kW depending on turbine size segment. With the noise-barrier as the main structural component, the *Energy Wall* system does not require a foundation for the installation of the wind turbine. This cost is avoided and represents a major cost reduction for the overall project. However, the system does require mounting the bracket on top of the noise-barrier. The cost, including labor and material, of coupling the bracket onto the noise-barrier was determined on the basis of comparison between cost data from two projects as explained in section 7.2.2.

Electrical infrastructure. The electrical installation of a wind turbine includes wiring through the tower to controls and installing the wire run to the interconnection point. Besides costs from labor, equipment and material, underground wiring requires trenching and backfill costs, which increase with increasing distance to the point of coupling with the utility grid. Single-turbine projects in isolated rural areas are prone to have considerably higher electrical infrastructure costs than multi-turbine projects in urban or peri-urban areas. Ranges reported in [2] vary between 372 and 460 Eur/kW depending on turbine size segment and represent about 6% of the total system cost. The electrical infrastructures of the wind and solar systems are compatible to a certain extent giving rise to a cost advantage.

Installation. This category comprises labor, equipment and material costs for site preparation, turbine installation and commissioning. Turbine dimensions and weight are main drivers of these costs as larger tur-

bines will require larger cranes and longer installation times. Labor costs vary geographically and estimates are often only indicative. For pricing the installation of the selected turbine on the noise-barrier bracket, insights gained from the *micro* turbine developer interview were used.

Transport. This category accounts for the costs associated with transporting all materials, including the turbine and the bracket, from their whereabouts to the installation site. Distance to the site, accessibility and dimensions of the transported goods are the main drivers of this cost. Large turbines with longer installation periods also require logistics for loading, unloading, storage and timing. Reasonably, for projects employing *micro* turbines, transport costs below reported averages are expected. Moreover, economies of scale apply raising opportunities for cost reduction in multi-turbine projects.

Sales Tax. The sales tax associated with the acquisition and installation of a *Wind Challenge* turbine amounts to 725 Eur as specified on the manufacturer's website. Multiple factors that influence tax rates and there is high uncertainty in estimating taxes based on published rates.

Zoning, permitting, interconnection and incentives (ZPII). This category includes fees, labor cost and time associated with the different administrative processes required for the installation of a turbine. Commonly, this cost is proportionally higher for small projects and sites requiring extensive permitting requirements. Capacity-weighted ZPII costs can vary between 45 and 1611 Eur/kW installed [2]. Zoning costs add up to 20% and arise because individual wind turbine systems fall outside standard community zoning ordinances. Therefore, it can be that the first cost a project incurs is obtaining approval for a zoning variance. Structural permits include foundation design and geotechnical reports and represent more than 35% of the total ZPII costs. Smaller and lighter turbines can arguably result in simplified foundation reports. Considering the particularities of the *Energy Wall* it is expected that special installation permits will be necessary. For instance, blocking of a highway lane may be required at sites where rear access is not possible and the physical space between the noise-barrier and the traffic lane is insufficient. Interconnection costs are rarely more than 10% of ZPII and incentive processing and transaction costs are not applicable for this economic assessment because a transparent analysis is prioritized to allow a more clear comparison with other standard methods. In absolute terms, the ZPII costs of a single-turbine project and a project employing ten turbines are presumably similar. Thus, multi-turbine projects may expect ZPII percentages at the low-end of the range, which is between 222 and 643 Eur/kW as reported in [2] for their commercial and residential categories, respectively.

Marketing, overhead and profit (MOP). This category accounts for the difference between the costs of a project and the actual price of the installed wind turbine system. Marketing and advertising costs are also included. Based on the cost data used in [2], found average values of 708 and 1394 Eur/kW for their commercial and residential categories respectively. The study also concluded that the allocation of MOP costs is influenced by economies of scale. Dynamic companies with multiple installations will spread overhead costs over a larger number of projects.

B.2. Description of solar system costs

This section looks closer at each of the costs items of a non-residential distributed solar system. As discussed in the body of the report, the narrower range of solar modules size and rated capacity when compared to wind turbines makes the use of existing cost benchmarks more appealing. Certainly, there is not a unique price, but the variability in solar system pricing is far more understood than that of wind systems. For this reason, provided that installing a solar panel on the noise barrier is not so different from installing it on very slanted roof, NREL's *U.S. Solar Photovoltaic System Cost Benchmark* [45] is used as a good point of reference. This choice is made mindful of the location dependency of solar system installed prices. One can expect the figures reported in this analysis to be higher than those based on a country leading the solar photovoltaics market. Despite this, NREL's cost analysis goes beyond stating the wholesale price of modules and describes with great level of detail the different costs associated with a complete system installation. Itemized costs are valuable to identify potential cost allocation arising from the hybrid integration of solar and wind energy systems.

Equipment System. This category is comprised by the solar panel and the inverter. The spot price of U.S. crystalline-silicon modules in 2017 was 0.28 Eur/W [45]. For a system size of 200kW this price represents 19% of the overall system cost. First buyer price of a three-phase string inverter is 0.08 Eur/W on average and add

up to 5% of the system cost.

Structural infrastructure. The structural infrastructure includes the racking system, which in this case is a flush mount with structural penetration to assure that the solar panels are secured onto the noise barrier. Different from roof mounted installations, the noise-barrier does not have weight limitations allowing more freedom in the choice of a proper mount. A typical mounting structure accounts for 8% of the total cost, unless special racking system is needed to minimize weight.

Electrical infrastructure. This category includes the cost of conductors, fittings, transition boxes and panel boards. Besides material and labor costs, underground wiring requires trenching and backfill is also needed, adding up to 8% of the total system cost. This cost can potentially be shared with the electrical infrastructure of the wind system.

Installation. This category comprises labor, equipment and material costs. Installation costs vary by location and mounting type. For a standard roof-top mount, installation generally accounts for 9% of the total cost of the system.

Transport. This category accounts for the costs associated with transporting all materials and usually represents 10% of the overall cost.

Sales Tax. Taxes vary greatly by location but make up, on average, 3% of the total cost [45].

Zoning, permitting, interconnection and incentives (ZPII). This category includes fees, construction permits, testing and interconnection and commissioning. NREL's range is between 0.9-0.13 Eur/W. Zoning is less of an issue for distributed solar systems than what it is for distributed wind. In fact, zoning is commonly not included in the taxonomy. ZPII costs are incurred on a per-project basis and, therefore, hybridization brings a cost-sharing opportunity.

Marketing, overhead and profit (MOP). This category includes all fixed overhead expenses and a 7% of profit applied to all costs. On average, this costs amount 28% of the total system expenditure.

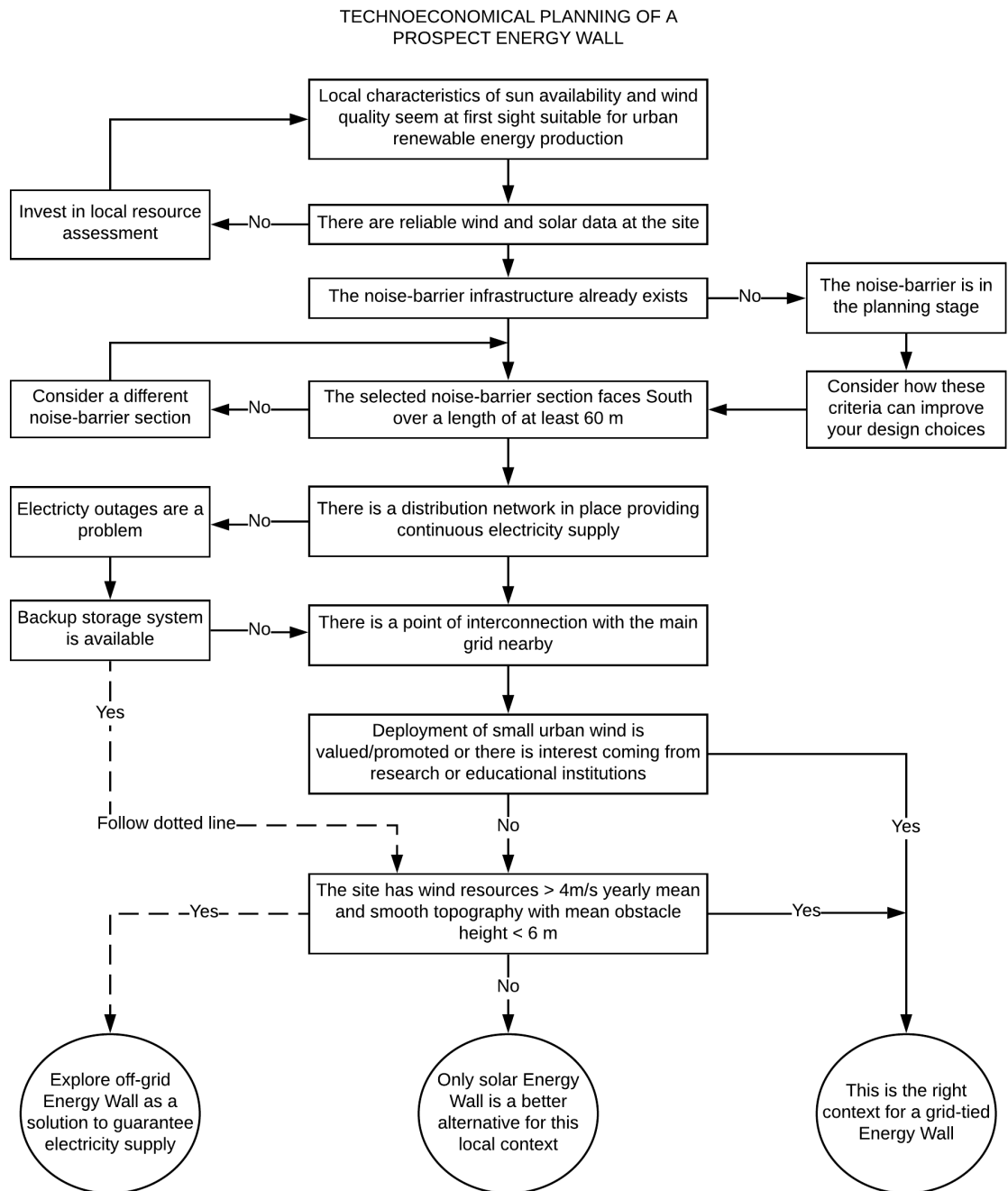


Technoeconomical Roadmap

The decision-making tree presented in this appendix (see next page) attempts to illustrate the level of subjectivity inherent in evaluating the merits of each of the three systems assessed throughout the report. These being; only wind, only solar and hybrid *Energy Wall*. The desirability each system varies with,

- Location
- Stakeholder
- Time

Although far from being exhaustive, the different paths of the roadmap show how the factors mentioned above affect decision-making of a future *Energy Wall*. Continuous electricity supply is not worldwide guaranteed which makes energy needs vary geographically. An off-grid *Energy Wall* can improve the well-being of communities affected by power outages. Such a contribution, however, has little value in areas where security of supply is not an issue. The local resources of each location also determine the contribution that each investigated system can potentially make. Likewise, this contribution will be valued differently among the wide variety of stakeholders engaged in the energy sector. Their interests on the project may be different, making evaluation criteria highly subjective. And last, but certainly not least, desirability of each system will also vary temporarily and evolve with technology improvements and price changes.

Figure C.1: Example of techno-economical planning of a prospect *Energy Wall*



Codes and Resources

All in-house developed codes for data processing and modeling have been compiled and are available upon request to Nikolaos Chrysochoidis in the Process & Energy department of TU Delft.

Bibliography

- [1] January 2018. URL <http://www.knmi.nl/kennis-en-datacentrum>.
- [2] E. A. Poehlman A. C. Orrell. Benchmarking u.s. small wind costs. Report, Pacific Northwest National Laboratory (PNNL), 2017.
- [3] U.S. Energy Information Administration. Levelized cost and levelized avoided cost of new generation resources in the annual energy outlook 2017. Report, EIA, April 2017.
- [4] Scott L. Morris Juliet S Homer. Alice C Orrell, Mikolas F Foster. 2016 distributed wind market report. Report, Pacific Northwest National Laboratory (PNNL), 2017.
- [5] Olindo Isabella René ACMM van Swaaij Miro Zeman Arno HM Smets, Klaus Jäger. *Solar energy. The physics and engineering of photovoltaic conversion technologies and systems*. UIT Cambridge Ltd, England, 2016.
- [6] DWEA (Distributed Wind Energy Association. Dwea distriuted wind vision 2015-2030: Strategies to reach 30gw of "behind-the-meter" wind generation by 2030. Report, 2015. URL <http://distributedwind.org/wp-content/uploads/2012/09/DWEA-Distributed-Wind-Vision.pdf>.
- [7] A. Barragán, P. Arias, and J. Terrados. Renewable energy generation technologies on urban scale. *Renewable Energy and Power Quality Journal*, 1(15):681–685, 2017. ISSN 2172038X 2172038X. doi: 10.24084/repqj15.432.
- [8] Arne W. S. Kaas Bauer and Pavol. Design approaches for a sustainable off-grid power system. *IEEE*, 2011.
- [9] Ziyad M. Salameh Bogdan S. Borowy. Methodology for optimally sizing a combination of a battery bank and pv array in a wind/pv hybrid system. 1996.
- [10] T. R. Oke C. S. B. Grimmond. Aerodynamic properties of urban areas derived from analysis of surface form. *Applied Meteorology*, 38, 1988.
- [11] CanWEA. Small wind market survey. Report, Canada Wind Energy Association, 2010.
- [12] Jessica Thomsen Niklas Hartmann Charlotte Senkpiel Simon Philipps Sebastian Nold Simon Lude Noha Saad Thomas Schlegl Christoph Kost, Johannes N. Mayer. Levelized cost of electricity renewable nergy technologies. Report, Fraunhofer Institut for Solar Energy systems (ISE), 2013.
- [13] World Commission on Environment and Development. Our common future. Report, Oxford University Press, 1987.
- [14] S. Diaf, D. Diaf, M. Belhamel, M. Haddadi, and A. Louche. A methodology for optimal sizing of autonomous hybrid pv/wind system. *Energy Policy*, 35(11):5708–5718, 2007. ISSN 03014215. doi: 10.1016/j.enpol.2007.06.020.
- [15] Encraft. Warwick wind trials project. Report, 2009.
- [16] Pika Energy. Pika t701 turbine. installation and service manual. Report, 2017.
- [17] M. K. Fuentes. A simplified thermal model for flat-plate photovoltaic arrays. *Sandia National Laboratories*, 1987.
- [18] Naïm Darghouth Galen Barbose. Tracking the sun ix. the installed price of residential and non-residential photovoltaic systems in the united states. Report, Lawrence Berkeley National Laboratory (LBNL), 2016. URL <http://trackingthesun.lbl.gov>.

- [19] Mario Petrollese Soren Knudsen K. Christian Milan Giorgio Cau, Daniele Cocco. Energy management strategy based on short-term generation scheduling for a renewable microgrid using a hydrogen storage system. *Energy Conversion and Management*, 87:820–831, 2014.
- [20] Mario Petrollese Giorgio Cau, Daniele Cocco. Modeling and simulation of an isolated hybrid microgrid with hydrogen production and storage. *Energy Procedia*, 45, 2013.
- [21] Parbir S. Grewal and Parwinder S. Grewal. Can cities become self-reliant in energy? a technological scenario analysis for cleveland, ohio. *Cities*, 31:404–411, 2013. ISSN 02642751. doi: 10.1016/j.cities.2012.05.015.
- [22] Malcolm A. Heath, John D. Walshe, and Simon J. Watson. Estimating the potential yield of small building-mounted wind turbines. *Wind Energy*, 10(3):271–287, 2007. ISSN 10954244 10991824. doi: 10.1002/we.222.
- [23] Karl Georg Hoyer. The history of alternative fuels in transportation: The case of electric and hybrid cars. *Utilities Policy*, 16(2):63–71, 2008. ISSN 09571787. doi: 10.1016/j.jup.2007.11.001.
- [24] Gill Instruments. Windmaster and windmaster pro ultrasonic anemometer. Report 1561-PS-0001, Gill Instruments, 2010.
- [25] IRENA. Wind power. Report, International Renewable Energy Agency (IRENA), 2012. URL www.irena.org.
- [26] IRENA. Renewable energy in cities. Report, International Renewable Energy Agency (IRENA), 2016. URL www.irena.org.
- [27] T. F. Ishugah, Y. Li, R. Z. Wang, and J. K. Kiplagat. Advances in wind energy resource exploitation in urban environment: A review. *Renewable and Sustainable Energy Reviews*, 37:613–626, 2014. ISSN 13640321. doi: 10.1016/j.rser.2014.05.053.
- [28] Dr Neveen Hamza Islam Abohela and Dr Steven Dudek. Building height and urban configuration effects on wind flow above a barrel vaulted roof. *BS2013*, 2013.
- [29] A. L. Rogers J. F. Meanwell, J. G. McGowan. *Wind energy explained: theory, design and application*. Wiley, United Kingdom, 2nd ed. edition, 2009. ISBN 978-0-470-01500-1.
- [30] L. Ma D. B. Ingham M. Pourkashanian J. T. Millward-Hopkins, A. S. Tomlin. Mapping the urban wind resource over uk cities using an analytical downscaling method. In *EWEA Annual Conference*. White Rose.
- [31] Stephen P. Carroll Katerina Syngellakis, Peter Robinson. Urban wind turbines: Development of the uk market. Report, 2006.
- [32] Dirk C. Jordan Kurtz and Sarah R. Photovoltaic degradation rates. an analytical review. *Progress in Photovoltaics: Research and Applications*, (NREL/JA-5200-51664):30, 2012.
- [33] Wouter R. W. A. Leduc and Ferry M. G. Van Kann. Spatial planning based on urban energy harvesting toward productive urban regions. *Journal of Cleaner Production*, 39:180–190, 2013. ISSN 09596526. doi: 10.1016/j.jclepro.2012.09.014.
- [34] Zhang Kai Lin Jian-Zhong, Li Hui-Jun. New expressions for the surface roughness length and displacement height in the atmospheric boundary layer. *Chinese Physics*, 16, 2007.
- [35] Gang Liu, Jianning Sun, and Weimei Jiang. Observational verification of urban surface roughness parameters derived from morphological models. *Meteorological Applications*, 16(2):205–213, 2009. ISSN 1350482714698080. doi: 10.1002/met.109.
- [36] Paul Noothout Sofia Boutsikoudi Robert Lucie Tesniere, David de Jager, Ivana Naydenova Silvia Nicola Boris Valach Mak Brückmann, Flora Borek, and Marko Dabetic Dukan, Leo Jerkic. Mapping the cost of capital for wind and solar energy in south eastern european member states. Report, ERCOFYS Netherlands B.V., 2016.

- [37] Sander Mertens. Wind energy in the built environment. 2006.
- [38] M. J. Jansen N. J. C. M. van der Borg. Photovoltaic noise barrier at the a9-highway in the netherlands. *ECN-C-01-021*, 2001. URL http://pvdatabase.nl/pdf/PV_schermA9_English.pdf.
- [39] U. Corsmeier M. Kohler B. Vogel N. Kalthoff, D. Bäumer. Vehicle-induced turbulence near a motorway. *Atmospheric Environment*, 39:5737–5749, 2004.
- [40] Michael Nash. Potential of the energy wall, a renewable energy generating noise barrier - with a focus on rotterdam, netherlands. 2018.
- [41] NREL/Sandia/Suspec. Best practices in photovoltaic system operations and maintenance. Report, National Renewable Energy Laboratory (NREL), 2016.
- [42] Evert Rajjen P. Bauer, Leake E. Weldemariam. Stand-alone microgrids. *IEEE*, 2011.
- [43] D. H. Wood P. R. Ebert. Observations of the starting behavior of a small horizontalaxis wind turbine. *Renewable Energy*, 12(3):245–257, 1997.
- [44] D. J. Hall R. W. Macdonald, R. F. Griffiths. An improved method for the estimation of surface roughness of obstacle arrays. *Atmospheric Environment*, 32, 1998.
- [45] Robert Margolis Mike Woodhouse Ran Fu, David Feldman and Kristen Ardani. U.s. solar photovoltaic system cost benchmark: Q1 2017. Report, National Renewable Energy Laboratory (NREL), August 2017 2017.
- [46] S. Trivikrama Rao Robert E. Eskridge. Measurement and prediction of traffic-induced turbulence and velocity fields near roadways. *Climate and Applied Meteorology*, 22:1431–1443, 1983.
- [47] Mariya Soshinskaya, Wina H. J. Crijns-Graus, Jos van der Meer, and Josep M. Guerrero. Application of a microgrid with renewables for a water treatment plant. *Applied Energy*, 134:20–34, 2014. ISSN 03062619. doi: 10.1016/j.apenergy.2014.07.097.
- [48] Robert Preus Suzanne Tegen Trudy Forsyth, Tony Jimenez and Ian Baring-Gould. The distributed wind cost taxonomy. Report, National Renewable Energy Laboratory (NREL), 2017.
- [49] Carbon Trust. Small-scale wind energy. policy insights and practical guidance. Report, Carbon Trust, 2008. URL www.carbontrust.co.uk.
- [50] Gaillard M. Gibescu M Slootweg J.G. Kling W.L. Veldman, E. Modelling future residential load profiles. *Innovation for Sustainable Production*, 2010.
- [51] Sara Louise Walker. Building mounted wind turbines and their suitability for the urban scale. a review of methods of estimating urban wind resource. *Energy and Buildings*, 43(8):1852–1862, 2011. ISSN 03787788. doi: 10.1016/j.enbuild.2011.03.032.
- [52] G. Venkataramanan W.D. Kellogg, M.H. Nehrir and V. Gerez. Generation unit sizing and cost analysis for stand-alone wind photovoltaic and hybrid pv wind systems. *IEEE*, 1998.
- [53] Tony Schoen Wilfried van Sark. Inventarisatie pv markt nederland. Report, Stichting Monitoring Zonnestroom (SMZ), 2016.
- [54] Harry Wirth. Recent facts about photovoltaics in germany. Report, Fraunhofer Institute for Solar Energy Systems (ISE), February 2018.
- [55] Hongxing Yang, Lin Lu, and Wei Zhou. A novel optimization sizing model for hybrid solar-wind power generation system. *Solar Energy*, 81(1):76–84, 2007. ISSN 0038092X. doi: 10.1016/j.solener.2006.06.010.
- [56] Hongxing Yang, Wei Zhou, Lin Lu, and Zhaohong Fang. Optimal sizing method for stand-alone hybrid solar-wind system with lpsp technology by using genetic algorithm. *Solar Energy*, 82(4):354–367, 2008. ISSN 0038092X. doi: 10.1016/j.solener.2007.08.005.